ABSTRACT

HOU, FEIER. Transition Zone Theory: a New Theory to Explain the Mechanisms of Crystallization, Viscous Relaxation and Glass Transition. (Under the direction of James D. Martin).

Crystal growth and viscous relaxation are known to be activated processes, albeit inadequately described by transition state theories. A new theory, transition zone theory (TZT), for crystallization, and also for the related but distinct process of liquid relaxation, has been developed by extending the Eyring transition state theory and the Kauzmann configurational entropy concepts to address the condensed phase activated processes, in which entropic and enthalpic activation probabilities scale with the cooperativity of the reactant, and the attempt frequency pre-factor (k_BT/h) is scaled by a characteristic phonon wavelength equal to twice the lattice constant for crystal growth, and the density of the liquid and the sound velocity in the liquid for viscous relaxation. TZT accurately describes the temperature dependent crystal growth rates and viscosity of diverse materials over the entire temperature ranges T_g to T_m and T_g to T_c, respectively, and affords detailed mechanistic understanding of condensed matter reactions like is afforded to molecular chemistry by the Eyring equation.

Previous group members have encountered the problem of the crystallization rate constants being experimental-technique dependent with the traditional Kolmogorov-Johnson and Mehl-Avrami (KJMA) model, and solved it by reintroducing the sample sizes and geometries into the KJMA model. Subsequently, melt and cold crystallization of the model system, halozeotype CZX-1, were investigated experimentally, with the latter normally exhibit more crystallites in the sample and faster crystallization rates than the former when bulk samples are evaluated. With the in-group developed software, the growth rates of individual crystallites in polycrystalline samples were obtained, which subsequently leads to an initial

nucleation normalization constant introduced into the modified KJMA model to obtain material-specific crystallization kinetics for polycrystalline growth. With that, TZT for crystallization has demonstrated that melt and cold crystallization likely share the same mechanism, which has enabled investigation of crystallization kinetics over a broader temperature range by both melt and cold crystallization.

With the material-specific crystallization kinetics and a comprehensive theory for crystallization established, the kinetic isotope effect on crystallization of CZX-1 with differently isotopically substituted templates was studied to investigate the influence of the templating cation on the crystallization process, and to further articulate details of chemical processes involved in crystallization. By comparing the enthalpy and entropy of activation of crystallization obtained by TZT for differently isotopically substituted templates, both the hydrogen bonding and the template reorientational effects on crystallization were observed.

TZT demonstrates that the entropy of activation for crystallization and relaxation exhibit inverse temperature dependency such that there is a temperature at which their free energies of activation are equivalent. Below this temperature, TZT suggests that there is a greater probability of crystallization than of relaxation, yet under these conditions, crystallization can only propagate over the length scale that atoms and molecules rearrange cooperatively during relaxation. In the non-relaxed, quenched system, such crystal-type organization occurring over only a few tens of nanometers makes the barrier to bulk liquid relaxation insurmountable. Herein crystallization and viscosity data of fourteen diverse systems are evaluated by this theory demonstrating that the crystallization-relaxation free energy equivalence point defines the glass transition temperature.

Transition Zone Theory: a New Theory to Explain the Mechanisms of Crystallization, Viscous Relaxation and Glass Transition

by
Feier Hou

A dissertation submitted to the Graduate Faculty of
North Carolina State University
in partial fulfillment of the
requirements for the Degree of
Doctor of Philosophy

Chemistry

Raleigh, North Carolina

2015

APPROVED BY:

_____	_____
James D. Martin Committee Chair	Jerry L. Whitten
_____	_____
David A. Shultz	Walter W. Weare

DEDICATION

This work is dedicated to my beloved middle school teacher, Ms. Lianjun Xia. Ms. Xia has been a motherly figure in my life since I became her student in 7th grade. She loves all her students unconditionally, no matter what their personalities are, how they are doing in school or what kind of families they are from, and she is the most responsible teacher I have ever met when it comes to teaching. She has taught me not only knowledge, but also to always be curious to learn, to always be rigorous in whatever I am studying, to be kind to everyone, and to love, understand, and listen to everyone without prejudice. There had been a period of time in my teenage years when I was quite confused, was bullied at school and had very low self-esteem, and without her unconditional, heart-warming support, love and trust in me, I would not have made through it so quickly without it having further impact on my life. Without her, none of this would ever be possible, and I would not be the person I am today. Thank you, Ms. Xia, you are a great educator, and you will always be my beloved teacher and a motherly figure I can trust.

BIOGRAPHY

Feier Hou was born on June 2, 1988 in Luoyang, Henan, China to parents Jun Hou and Zheng Wu. She graduated high school in 2006, then started attending Beijing Normal University in September, 2006 as a physics major, but changed her major to chemistry in the fall semester of 2007. She received her Bachelors of Science Degree in Chemistry from Beijing Normal University in July, 2010. She then moved to Raleigh, North Carolina and started graduate school at North Carolina State University in August, 2010.

ACKNOWLEDGMENTS

Just like any other achievements in science, my graduate work could not possibly be accomplished just by myself, and I have many people to be thankful for. First of all, I would like to thank my advisor, Jim, for being a great mentor. You are always available whenever I need your help, yet you are quite hands-off and I can get enough freedom to manage my research at my own pace, which makes you the perfect advisor for what I am looking for. The change may be gradual, but over the years, I have adopted a lot of your strategies, creativity and mentality towards science, which I am sure will be very beneficial for my future research. Also, thank you for not always being ridiculously serious (except in science) or "proper", which makes it much easier to see you as a human instead of "a brain in a jar", and much easier for me to talk to you.

I would also like to thank Dr. Jaap Folmer, whom I see as my "second advisor". You are a human-shaped encyclopedia, fluent in countless languages, including Dutch, German, English, French, Afrikaans, Statistics, Glass Transition, and all others that I do not even know the names for, and you have lived on (Gasp!) three continents. Thank you for all your help in reviewing my manuscripts and in my work in general, especially for asking questions that I could not possibly have thought of, some of which tore my ideas apart but are the most helpful.

I would like to thank all the Martin group members, especially the following ones, in chronological order: Amanda, we have never met in person because you graduated before I joined the group, but a big part of my crystallization work is built on your work in the Martin group, and I could not have climbed so high without standing on your shoulders. Eric, thank you for teaching me the ropes of this project, and for your further help in my super stressful

postdoc application. If we meet again, please remember to bring Penelope so I can pet her! Brad, thank you for being a great colleague as well as a friend through the long journey of graduate school, and wish you the best with your research as well as with your soon-to-come married life! All the undergrads, Mick, James, Troy and Olivia, thank you for being great lab mates, and special thanks to Olivia for your hard work on analyzing the synchrotron data.

I would also like to thank my friends, family and everyone that have indirectly but positively affected me on this seemingly never-ending journey of grad school. Dad and mom, thank you for loving me as I am, providing me with the best you can give, always caring about my happiness and well-being, and being supportive and encouraging me to pursue my dream in science, despite the pressure that the rest of the family and most of the society keep telling you it is pointless for a girl to get advanced education and a girl's only purpose in life is to find a husband and give birth to children. David and Mandy, you are the best friends I can ever ask for, without you I would never have made this far in grad school; thank you for always being there for me, telling me I am worth it, and supporting me through thick and thin; I miss you every day since you moved to Minnesota, but I know we will always stay close and have many happy years together ahead. Marc, thank you for being a great friend, for your kind help in and out of grad school, and for always being so trust-worthy and so easy to talk to whenever I need you; those trips to the "cawfee" shop were so much fun, just remember not to feed "cawfee" to your "dawg"! April, Chelsea and Crystal, you are the best roommates I have ever had, with whom I know that after a long day, I can come home to someone to talk to and have fun with, plus all the floppy, furry kisses from your animals. Last but not least, thank my teachers throughout the years, specifically, Ms. Jinqin Wang from 1st grade, who has taught me how to

learn and how to grow into a disciplined, kind person with empathy; Ms. Xiaolan Zhong from 5th grade, who was my first English teacher, and who is an excellent teacher that laid a solid foundation for me in learning foreign languages, a skill which is extremely useful especially after I came to the United States. Ms. Chunlei Zhang from 9th grade, who was my first chemistry teacher and who has sparked my interest in chemistry – I still find some of the things she taught me quite useful even when I am studying chemistry in graduate school; Mr. Yanqi Zhang and Mr. Zhifa Cai from my senior high school year, who have encouraged me in learning math and physics, while all my previous teachers have told me I am such an idiot in those two subjects, and with their encouragement and excellent teaching skills, I have eventually become good and interested in those two subjects, which is later proved to be really beneficial for my research.

Finally, thank the chemistry department at NC State University for support in my graduate research, and thank my committee members, Dr. Whitten, Dr. Shultz and Dr. Weare and the graduate school representative, Dr. Tonelli for reading this document and for attending my final defense. The experimental work determining the crystallization rate of CZX-1 was supported by the National Science Foundation via the contracts DMR-0305086 and DMR-0705190. Use of the National Synchrotron Light Source, Brookhaven National Laboratory and the Advanced Photon Source, Argonne National Laboratory, Office of Science User Facilities operated for the U.S. Department of Energy (DOE) Office of Science, was supported by the U.S. DOE under Contract No. DE-AC02-98CH10886 and DE-AC02-06CH11357, respectively. Beam line scientists Jonathan Hanson, Elaine DiMasi, Peter Chupas, and Karina Chapman are gratefully acknowledged.

TABLE OF CONTENTS

LIST OF TABLES

LIST OF FIGURES

CHAPTER 1

General Introduction

1.1. Background

The solidification of homogeneous liquids through crystallization or glass transition is critical to diverse areas of science and technology, ranging from naturally occurring phenomena, to purification and synthesis in physical sciences, to energy and information storage technologies. Nevertheless, mechanistic descriptions of either crystallization or glass transition remain inadequate and highly empirical[1-4].

It has been observed that the rate of crystallization from congruent melt increases above the glass transition temperature, T_g ("Arrhenius") up to some maximum temperature, T_{max}, above which it decreases ("anti-Arrhenius") gradually to zero at the melting temperature, T_m[5]. This behavior has mostly been described by either the classical nucleation theory (CNT)[6-8] or the model of interface controlled growth (ICG)[5,9-12]. CNT, initially derived from condensation from the gas phase and then extended to condensed systems, describes the Arrhenius and anti-Arrhenius regions as being growth and nucleation controlled, respectively, yet it treats nucleation and growth as parallel processes while singular nucleation events must occur before crystal growth, and contrary to CNT, anti-Arrhenius behavior has actually been experimentally observed in the rate of single crystal growth, without further nucleation, above T_{max}[5,9,13]. The ICG model differentiates the anti-Arrhenius and Arrhenius regions as thermodynamically and diffusion or kinetically controlled regions, respectively, the latter of which is related to viscous relaxation of the liquid and is often described with the empirical VFT equation. However, the thermodynamic control assumes equilibrium between the supercooled liquid and the crystal,

which is inconsistent with the first order nature of crystallization[14], while the diffusion control assumes mass transport across a defined liquid/crystal interface, which is actually not sharply defined[15,16] due to the equivalent short- and intermediate-range order of liquid and crystalline phases[17-21]. Furthermore, viscous relaxation of liquids, albeit related, is a distinct process from crystallization, and it is faster than the rate of crystallization and is generally complete before crystallization[22]. Therefore, relaxation can not be the rate determining step to the slower crystallization process, and the mechanism of relaxation must be treated separately from that of crystallization.

Understanding of the glass transition from the atomic and molecular level has been limited so far. Andersen suggested in 1995 that "The deepest and most interesting unsolved problem in solid state theory is probably the theory of the nature of glass and the glass transition"[1], and recent reports probing the glass transition problem reinforce that this problem remains unresolved[23]. It is still being debated whether glass transition is a thermodynamic or kinetic phenomenon[4,24-26]. Thermodynamically, glass transition is defined as the temperature at which the rate of change of the thermodynamic properties of a liquid, such as heat capacity, enthalpy or entropy, with respect to temperature decrease abruptly (but continuously) to a value comparable to that of a crystalline solid. Such definition, although based on intrinsic properties of the liquid, is mostly qualitative and does not explain glass transition at the atomic or molecular level. Kinetically, glass transition is usually defined as the temperature at which the shear relaxation time or viscosity of the liquid reaches a common large value (e.g. 10^2 s or 10^{13} Poise[25,27]). Such definition is empirical, and the explanation of the glass transition is based on the classic VFT theory of liquid relaxation and viscosity[28-30] or its WLF derivative[31], which are also highly empirical, can only accurately describe experimental viscosity data within a

limited temperature region and a temperature dependent crossover from VFT to Arrhenius theory is expected[31-33].

Therefore, it is the goal of this work to remove the empiricism and fundamentally understand crystallization, the related but distinct process of viscous relaxation, and the glass transition, with which control and prediction of those processes can be made possible.

1.2. Outline

In this work, a new theory, transition zone theory (TZT), which is an extension of the traditional transition state theory[34] to the condensed phase activated processes, is proposed to describe and provide mechanistic understanding of crystallization (TZT_c), viscous relaxation of liquids (TZT_{rlx})[35], and glass transition (TZT_{glass}).

In Chapter 2, details of TZT are presented[35], and the developmental process, especially the mathematical derivation of the pre-factors of TZT is explained. TZT is developed by extending the Eyring transition state theory[34] and the Kauzmann configurational entropy concepts[36] to address the condensed phase activated processes. It has been demonstrated to accurately describe crystallization and viscosity over the entire temperature range where experimental data are available for a wide variety of materials, spanning inorganic and organic, network, molecular and metallic materials, and the enthalpic and entropic activation parameters have been shown to provide detailed mechanistic understanding of those processes. TZT has also been validated for spherulite growth of crystalline polymers, as well as the unique viscosity behavior of sulfur due to significant structural change with temperature, the latter of which also suggests a possible application of TZT to study the liquid-liquid phase transition.

In Chapter 3, previous work from the group on modifying the traditional Kolmogorov[37]-Johnson and Mehl[38]-Avrami[39-41] (KJMA) model for the kinetics of condensed phase reactions by reintroducing the sample sizes and geometries into the KJMA model[13,42] has been expanded to obtain the material-specific crystal growth kinetics of polycrystalline growth, essentially the growth rate of individual crystallites. Extensive experimental measurements of melt and cold crystallization of our model system, halozeotype CZX-1[18,43], are reported, the latter of which always exhibits faster crystallization rates than the former when bulk samples are evaluated. With 2-D diffraction techniques, a greater number of nuclei have been observed for cold crystallization, and thus a bulk sample size correction would lead to an over estimation of the rate constant. With our in-group developed software, the growth rates of individual crystallites in polycrystalline samples have been determined, which has further afforded development of an initial nucleation normalization constant on the KJMA model. With the correction for initial nucleation, material-specific crystallization kinetics were obtained for melt and cold crystallization, to which TZT_c was applied to demonstrate if melt and cold crystallization share the same mechanism.

In Chapter 4, a higher-level mechanistic investigation on crystallization is described, which utilizes measurement of activation processes to articulate details of chemical processes involved in crystallization. Specifically, the goal of this chapter is to determine the influence of the templating cation on the crystallization process of the model system CZX-1. To accomplish that, crystallization kinetics of CZX-1 with d_0, d_1, d_9 and d_{10}-$[(H/DN(C(H/D)_3)_3]^+$ cationic templates have been studied experimentally over extensive temperature range to investigate the kinetic isotope effect on crystallization. With TZT_c applied, the enthalpy and entropy of activation for crystallization are compared for CZX-1 with differently isotopically

substituted templates, from which both hydrogen bonding and inertial effects of the template have been observed on crystallization.

After observing that according to TZT, the entropy of activation for crystallization and viscous relaxation exhibit inverse temperature dependency, TZT is expanded in Chapter 5 to explain the glass transition (TZT_{glass}). TZT_{glass} have shown that the glass transition occurs at the temperature where the free energy of activation for crystallization and relaxation become equivalent, below which crystallization has a higher probability than relaxation, yet crystallization can only propagate over the length scale that atoms and molecules rearrange cooperatively during relaxation, such that the bulk system can neither crystallize nor relax. TZT_{glass} quantifies the relationship between the competing crystallization and liquid relaxation processes to describe the glass transition temperature, validated with data from 14 distinct materials from the fragile molecular OTP to the strong network SiO_2, and has been shown to be applicable to non-crystallizing atactic polystyrene. The potential of applying TZT_{glass} to explain the glass aging process, the time-temperature superposition of glass transition, and the glass-to-crystal transition have also been discussed in this chapter.

CHAPTER 2

Transition Zone Theory of Crystal Growth and Viscosity

Section 2.1 of this chapter was previously published: Hou, F.; Martin, J. D.; Dill, E. D.; Folmer, J. C. W.; Josey, A. A. *Chem Mater* **2015**, *27*, 3526-3532.

2.1. General Theory

2.1.1 Introduction

The solidification of homogeneous liquids through crystallization or the formation of a glass is critical to diverse areas of science and technology. Despite the importance, mechanistic descriptions of congruent crystallization remain highly empirical and poorly understood[2-4]. Crystallization has been described by classical nucleation theory (CNT), initially derived for condensation from the gas phase and then extended to condensed systems,[6-8] and the model of interface controlled growth (ICG).[5,9-12] Viscous relaxation, which in the ICG model is also linked to the activation energy of crystallization, is described by the largely empirical VFT[28-30] or analogous WLF[31] functions. To better understand a broad range of physical processes from geologic formations to the design of new functional materials, it is necessary to remove empiricism and establish fundamental atomic and molecular level descriptions of the mechanism(s) of solidification.

Processes involved in solidification, e.g. relaxation of a supercooled melt, nucleation, and crystal growth, all exhibit characteristics of activated processes. While the Arrhenius relationship is attractive to obtain activation parameters, its applicability to condensed phase processes is questionable.[2,3] Only at high temperature is relaxation (1/viscosity, $1/\eta$) data

reasonably fit to Arrhenius kinetics. The VFT expression (Equation (2.1)) and the WLF derivative provide a better fit to relaxation data.[28-31]

$$\frac{1}{\eta} = \frac{1}{\eta_0} \exp\left(\frac{B}{T - T_0} \right) \tag{2.1}$$

η is the temperature dependent viscosity, η_0 is a frequency factor, B and T_0 are material specific empirical constants. However, many materials exhibit substantive deviation from the VFT model[32,33], and the WLF model only claims to fit data within 50 to 100 K of the glass transition temperature, T_g[31].

The rate of crystallization has been described as Arrhenius-like above T_g, up to some maximum temperature, T_{max}, above which anti-Arrhenius behavior is observed, decreasing to zero at the melting temperature, T_m[5]. CNT differentiates Arrhenius and anti-Arrhenius regions as being growth and nucleation controlled, respectively, with the barrier to nucleation responsible for the retardation of crystallization at high temperature. Interestingly, the Turnbull-Fisher CNT expression, Equation (2.2)[6-8], with independent activation terms for crystal growth, E_g, and nucleation, E_m, treats these processes in a parallel fashion when they must be serial since singular nucleation events precede continuing growth.

$$k = k_0 \exp\left(\frac{-E_g}{RT\left(T - T_g\right)} \right) \exp\left(\frac{-E_m}{RT\left(T_m - T\right)} \right) \tag{2.2}$$

In practice, E_g is commonly associated with the free energy of activation for viscous flow. E_m includes terms for the surface energy, the enthalpy of fusion, the atomic/molecular layer thickness as well as several empirical parameters.[44] However, we[13] and others[5,9,12] (see also references 139, 141, 145, 149, 150, 154, 156, 158, 167, 168, 170 from Appendix Table B.1.) have demonstrated that the growth of individual crystals, i.e. with no further nucleation,

is also slowed above T_{max}, which contradicts the idea of nucleation-controlled crystallization rates.

The ICG model alternatively delineates the Arrhenius and non-Arrhenius regions as thermodynamically vs. diffusion or kinetically controlled regions. As described by Equation (2.3)[5,11], the difference between the free energy of the melt and crystal, ΔG_c defines the region of thermodynamic control.

$$\Upsilon = \frac{f k_B T}{3\pi a_0^2 \eta}\left(1-\exp\left(\frac{-\Delta G_c}{RT}\right)\right) \tag{2.3}$$

Based on the Stokes-Einstein relationship, the VFT relaxation Equation (2.1) is used as the activation term to describe the diffusion across the liquid-crystal phase interface. Here, f is the fraction of sites of attachment, and a_0 is the atomic/molecular layer thickness. However, the thermodynamic control, described by equilibrium concepts, is inconsistent with the first order nature of crystallization[14]. Diffusion control assumes mass transport across a defined liquid/crystal interface, which is inconsistent with the essentially equivalent short- and intermediate-range structure of solid and liquid phases[17-21], such that an interface is not sharply defined[15,16]. Furthermore, it is experimentally recognized that relaxation is a faster process than the rate of growth[22], which from a mechanistic perspective means relaxation can not be rate determining to the slow step of crystal growth.

Given the questionable applicability of the Arrhenius-type models for both relaxation and crystal growth, consideration of the more detailed Eyring transition state theory (TST)[34] for condensed phase reactions is limited[45]. Kirkpatrick concluded "the meaning of the activation entropy for crystal-growth processes, … is not clear."[46] Nevertheless, while the local structure in liquid, glass and crystalline phases of congruently melting systems is essentially

equivalent, crystals uniquely exhibit long-range order. Thus, because the long-range ordering of atoms and molecules is likely rate determining, we suggest any theory to describe the crystallization process must explicitly address the entropy of activation.

Specifically, in this work we extend the Eyring TST[34] and Kauzmann configurational entropy[36] concepts to address condensed phase activated processes. The theory presented herein was developed to understand our kinetic data for the crystallization of the sodalite-type halozeotype, CZX-1[13], but is found to be generally applicable to diverse materials and processes.

2.1.2 Transition Zone Theory (TZT)

Eyring TST[34] describes the rate constant of a reaction as the product of a molecular collision attempt frequency (pre-factor) and the probability a reactant is activated to the transition state. Adam and Gibbs noted the traditional form of TST, in which single molecules pass over an activation barrier, is inadequate to describe condensed phase reactions. Instead cooperative rearrangements of groups of particles are required[47]. Thus, for homogeneous condensed phase reactions, there should be a transition zone (TZ) through which the condensed phase reaction must traverse. Correspondingly, instead of a Boltzmann distribution of atomic or molecular collisions, in the condensed phase one might assume a Boltzmann-type distribution of interacting phonons[2,3]. Such a distribution results in a characteristic frequency whereby some unit of matter transforms from a non-ergodic to ergodic liquid or a non-crystalline to crystalline phase, and thus the presumption of an attempt frequency related to $(k_B/T)/h$.

The striking contrast between TST and our TZT is that the entropy and enthalpy of activation of condensed phase reactions are significantly temperature dependent. Described as the Kauzmann paradox[36], the temperature dependence of a liquid's configurational entropy, S_l, is greater than that of its crystalline phase, S_c. As a result, there is a temperature, T_K, at which the projected configurational entropy of the liquid becomes equivalent to that of the crystal, shown schematically in Figure 1a. T_K can be obtained from the material's ΔH_m, T_m and ΔC_p[48]. For crystallization to occur, components of a liquid must be activated within the TZ such that their configurations begin to match the crystalline configurations. We suggest that like for a crystal, the configurational entropy of the crystallization TZ, $S_c^{\ddagger}$, should be small and reasonably temperature independent, such that at T_K it can be assumed $S_c = S_l = S_c^{\ddagger}$.

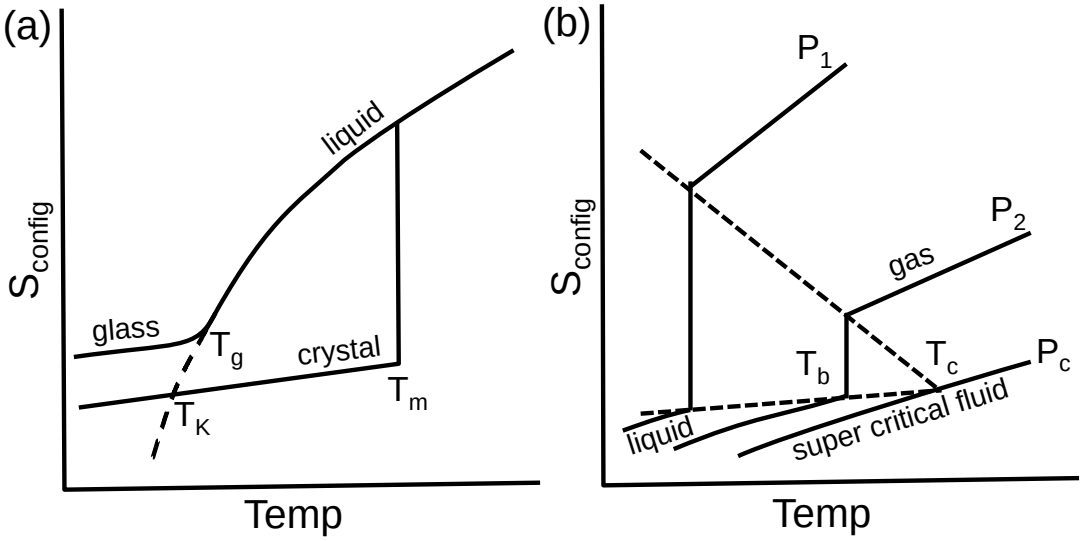

Figure 2.1. (a) Kauzmann paradox for which the extrapolated configurational entropy of a supercooled liquid is equivalent to that of the solid at T_K. (b) Schematic representation of the temperature/pressure dependence of configurational entropy of liquid-gas transitions. Liquid and gas saturation entropy lines (dashed) intersect at T_c where $\Delta S_{config} = 0$.

The concept of temperature and pressure dependent configurational entropy can be extended to consider the relationship of gas and liquid phases, represented in Figure 2.1b.

Below the critical point, T_c, but above the triple point, an entropic discontinuity is observed with vaporization. However, at T_c the configurational entropy of the gas and liquid become equivalent. Furthermore, at T_c ergodic and non-ergodic liquids become indistinguishable with the gas and supercritical fluid, such that we assume their configurational entropy is equivalent to that of the TZ for relaxation (i.e. $S_g = S_{erg\ l} = S_{non\text{-}erg\ l} = S_{rlx^{\ddagger}}$).

Boltzmann describes the molar entropy of a system as relating to the number of microstates, W; $S = R \ln(W)$. Thus, for one mole of material crystallized, if there are $W^{\ddagger}$ microstates accessible to the TZ and W_{rct} microstates accessible to the reactant phase (here the ergodic liquid for crystallization and the non-ergodic liquid for relaxation), then the entropy of activation can be described by Equation (2.4).

$$\Delta S^{\ddagger} = S^{\ddagger} - S_{rct} = R \ln\left(\frac{W^{\ddagger}}{W_{rct}}\right) \tag{2.4}$$

According to Equation (2.5), the entropic probability to rearrange into a specific TZ configuration is directly proportional to the ratio of the number of microstates of the TZ compared to that of the reactant phase.

$$\exp\left(\frac{\Delta S^{\ddagger}}{R}\right) = \frac{W^{\ddagger}}{W_{rct}} \tag{2.5}$$

Given Equation (2.5), and the configurational entropy conditions, $\Delta S^{\ddagger}$ goes to zero at T_K for crystallization and at T_c for relaxation.

Before considering the distinct temperature dependence of $\Delta S^{\ddagger}$ for crystallization and relaxation, it is important to recognize that the Kauzmann condition also impacts the enthalpy of activation, $\Delta H^{\ddagger}$. The $\Delta H^{\ddagger}$ is dominated by the energy required for making or breaking bonding interactions in the given transformation. As a reaction system approaches T_K the loss

of configurational microstates requires an increased size of the cooperative region for each activation event. If a liquid could be supercooled to T_K, the entire sample would need to transform as a single cooperative region; essentially an impossible condition. Nevertheless, consistent with the model proposed by Adam and Gibbs[47], $\Delta H^{\ddagger}$ should be proportional to the size of the cooperative regions‡, which can be modeled by Equation (2.6) where ΔH^* is a material specific parameter indicative of the bond reconstruction required for the transformation.

$$\Delta H^{\ddagger} = \Delta H^{*}\left(\frac{T}{T - T_K}\right) \tag{2.6}$$

The enthalpic probability is described by expression (2.7).

$$\exp\left(\frac{-\Delta H^{*}}{R\left(T - T_K\right)}\right) \tag{2.7}$$

Notably, expression (2.7) is similar to the VFT expression (Equation (2.1))[28-30] describing the temperature dependence of viscosity and likely accounts for the historic use of $1/\eta$ to describe the activation term for crystallization[5,11]. The physical process of bond/intermolecular force reorganization required on the local level for relaxation should be similar to that required for crystallization since the local structure of liquid, glass and crystalline phases is essentially equivalent[17-21]. However, the amount of material involved in a relaxation event is anticipated to be less than is required to develop crystalline order. Thus, while the enthalpic probability terms exhibit a common form, the enthalpic activation parameter for relaxation, ΔH_{rlx}^{*}, should normally be smaller than the enthalpic activation parameter for crystallization, ΔH_c^{*}.

Though crystallization and relaxation are related, they are distinctly different processes delineated by different temperature dependence of their $\Delta S^{\ddagger}$. Furthermore, their rates require different units for the pre-factor; the velocity of the phase boundary, v_{pb}, requires units of distance per time, whereas dynamic viscous relaxation, $1/\eta$, requires units of Poise^{-1} = 10 m•s/kg.

2.1.3. Crystal Growth (TZT_c)

To understand the temperature dependence of the entropy of activation for crystallization, $\Delta S_c^{\ddagger}$, it is important to consider the limits at T_K and T_m. In reality the Kauzmann paradox ($\Delta S_{liquid\text{-}solid} = 0$) is avoided by the glass transition. But if an ergodic liquid could be supercooled to T_K, an equivalent number of configurational microstates would be accessible to the liquid, the crystal and the TZ_c. Thus, $W_c^{\ddagger}/W_{erg\ l} = 1$ and $\Delta S_c^{\ddagger} = 0$. By contrast, at any temperature $T_K < T < T_m$, only a limited number of configurational microstates are suitable to form a TZ_c[49], but an increasingly large number are accessible to the ergodic liquid. Thus, as T_m is approached, $W_c^{\ddagger}/W_{erg\ l} \rightarrow 0$ and $\Delta S_c^{\ddagger} \rightarrow -\infty$. Above T_m the probability of achieving the TZ_c configuration is not defined. This temperature dependence of $\Delta S_c^{\ddagger}$ is modeled by Equation (2.8) where ΔS_c^{*} and z_c are material specific parameters that scale the magnitude of $\Delta S_c^{\ddagger}$ and modulate the temperature dependence, respectively.

$$\Delta S_c^{\ddagger} = \Delta S_c^{*}\left(\frac{T - T_K}{T_m - T}\right)^{z_c} \tag{2.8}$$

Developed to consider our CZX-1 crystallization data[13], initial modeling demonstrated no need for the empirical parameter z_c. However, upon considering data from a diverse set of materials, it was observed that crystallization data was more effectively fit for crystallization

of fragile liquids than for strong liquids. Given that the fragility/strength of a liquid is defined by the extent to which its relaxation deviates from Arrhenius behavior[27], and that for a system with a small T_K the $\Delta H^{\ddagger}$ term alone is approximately Arrhenius, we introduced the empirical parameter z_c such that when $z_c = 0$, $\Delta S_c^{\ddagger}$ is temperature independent. The strong interatomic/molecular interactions of a strong liquid limit the temperature dependence of the number of microstates accessible to the liquid, but $z_c > 0$ for more fragile systems because of the increasing number of microstates accessible to the liquid with increasing temperature.

To understand the attempt frequency pre-factor for crystallization, recall in TST the number of vibrations in the TS that can proceed towards the product is $(k_BT)/h\nu$[34]. The product of the number and frequency of vibrations gives the rate for the TS to proceed to the product, i.e. the Eyring pre-factor $(k_BT)/h$. Similarly the pre-factor for TZT_c is the product of the number of lattice vibrational modes that lead to formation of the crystalline phase, $(k_BT)/h\nu$, and the velocity of the TZ_c, $\lambda\nu$, where λ is some characteristic wavelength of vibrations that lead to growth. Thus, the TZT_c pre-factor is $\lambda(k_BT)/h$. Using a lattice harmonic oscillator approximation, we postulate that λ corresponds to the edge of the first Brillion zone of the allowed lattice vibrations. For a cubic lattice, $\lambda = 2a$; in the following analyses the average lattice constant of non-isotropic lattices is used as a first approximation of $\lambda/2$. Thus, for crystal growth to occur a cooperative set of vibrations must organize with the characteristic wavelength λ; essentially a standing wave pattern on the length scale of twice the unit cell dimension.

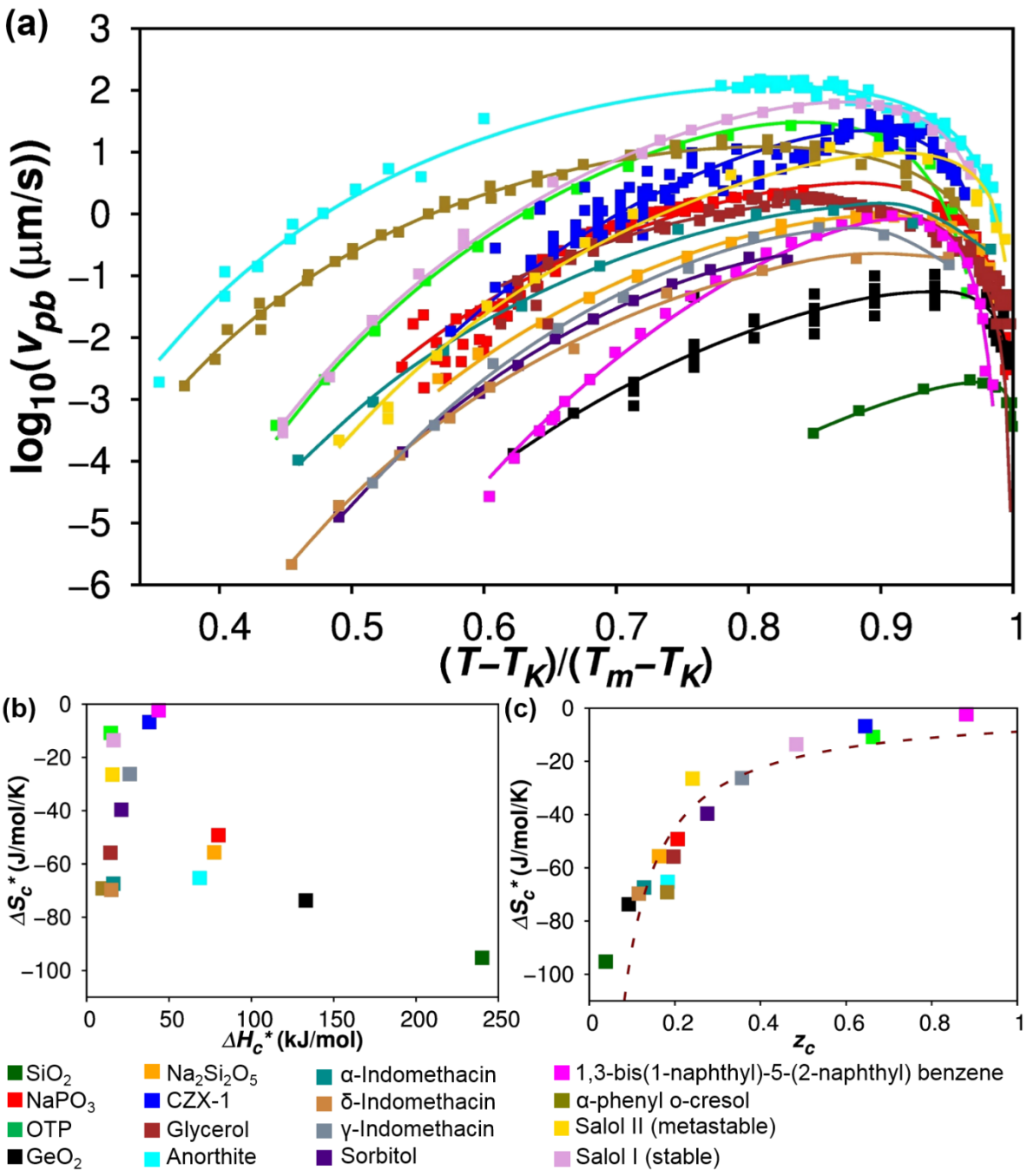

Figure 2.2. (a) Experimental crystallization rate data points with lines of the best fit to Equation (2.9), plotted with respect to the normalized temperature. (b) Correlation between ΔH_c^* and ΔS_c^*. (c) Correlation between z_c and ΔS_c^* and the correlation line $\Delta S_c^* = -3\text{csch}(z_c/3)$ (dashed).

Combining the pre-factor with the enthalpic and entropic probabilities yields the TZT_c expression, Equation (2.9).

$$v_{pb} = \lambda \frac{k_B T}{h} \exp\left(\frac{-\Delta H_c^*}{R\left(T - T_K\right)} \right) \exp\left(\frac{\Delta S_c^*}{R} \left(\frac{T - T_K}{T_m - T} \right)^{z_c} \right) \tag{2.9}$$

Mathematically one might note a similarity between Equation (2.9) and the CNT and ICG Equations (2.2) and (2.3), i.e. a double exponential form with temperature dependent exponential terms with limiting temperatures. They are distinct in that for Equation (2.9) the limiting temperatures are intrinsic thermodynamic values not empirical parameters, the exponentials are correctly unitless, and the pre-factor is defined by a physical property of the material. But most importantly, Equation (2.9) exclusively addresses the process of crystal growth, rather than convoluting nucleation or viscous relaxation with crystal growth.

The test of any theory is how effectively it fits experimental data, and whether the fitting parameters are physically meaningful. We developed this theory based on fitting our isothermal crystallization data for the sodalite-type halozeotype CZX-1[13]. The T_K for CZX-1 was measured to be 150 K using modulated DSC techniques[48]; data and the experimental procedure are given in Appendix A. However, to explore the breadth of applicability of TZT_c we turned to literature reports of the linear growth rate of crystal faces. When tabulated rate data is not published, crystallization rate vs. temperature data was extracted from digitized images of published figures. Data for CZX-1 and 15 additional crystalline phases, and the respective fit to Equation (2.9) is presented in Figure 2.2. Tabulation of fitting parameters and references is given in Supplemental Information Table S1. Lattice constants (averaged to obtain $\lambda/2$) were obtained from the literature, as were values for T_m and T_K. T_K data is least reliably reported, and when not available, T_0 from VFT analysis was used as a first

approximation. More accurate values for T_K are obtained by fitting to Equation (2.9), and when viscosity data is available also to Equation (2.11) below.

The rate of crystallization for this entire series of compounds spanning inorganic and organic, network and molecular materials, is well fit by Equation (2.9) using the experimental parameters λ, T_m and T_K and fitting parameters ΔH_c^*, ΔS_c^* and z_c. Further examination of the correlation between these parameters demonstrates an apparent exponential relationship between ΔS_c^* and z_c (Figure 2.2c). For crystallization it seems unlikely that ΔS_c^* should be positive or z_c be negative, thus the correlation function between ΔS_c^* and z_c should asymptote to zero for both parameters. This behavior is reasonably modeled with the hyperbolic cosecant function $\Delta S_c^* = -3\mathrm{csch}(z_c/3)$. We do not yet know the physical significance of the correlation constant 3, but presume it to be related to the 3-dimensionality of crystallization. Furthermore, we are not clear if all systems should be forced to this correlation thus requiring only two fitting parameters, or whether deviation from this correlation line is indicative of material diversity. Nevertheless, it is apparent that systems with most negative values of ΔS_c^* exhibit the least temperature dependence of $\Delta S_c^{\ddagger}$.

It is instructive to consider the physical/chemical significance of the comparative ΔH_c^* and ΔS_c^* parameters (Figure 2.2b). Not surprisingly SiO_2 and GeO_2 exhibit the largest values of ΔH_c^*, consistent with their strong covalent networks. Intermediate values of ΔH_c^* are observed for the somewhat deconstructed networks including polymeric $Na_2Si_2O_5$ and $NaPO_3$, and the open cage-network of anorthite. Molecular species, with weaker intermolecular forces, exhibit relatively small values of ΔH_c^*.

While all values of ΔS_c^* are negative, as expected for a liquid-to-crystal transition, it is interesting that the strong network materials SiO_2 and GeO_2, the cage-network of anorthite,

and molecular materials such as α-phenyl o-cresol and indomethacin exhibit large negative ΔS_c^*, whereas the cage-network CZX-1 and molecular o-terphenyl and 1,3-bis(1-naphthyl)-5-(2-naphthyl) benzene exhibit very small values of ΔS_c^*. Large negative values of ΔS_c^* suggest that substantial structural rearrangement is required to achieve a more crystal-like TZ_c structure. For example, diffraction studies of SiO_2, imply substantial changes in the O-Si-O angles, and the greater prevalence of 3-ring structural units in the melt, as opposed to only networked 6-rings in the crystalline phase[50]. By contrast a small value of ΔS_c^* implies the liquid is ordered similar to that of the TZ_c, consistent with our best interpretation of the structure of liquid and glassy CZX-1 for which a crystalline-like networked β-cage structure appears to persist with ~5 nm order into the liquid phase[18]. Notably, among molecular liquids, o-terphenyl and 1,3-bis(1-naphthyl)-5-(2-naphthyl) benzene, for which π-stacking is likely to cause longer-range order in the liquid[17], exhibit a small ΔS_c^*, whereas the strongly hydrogen bonding glycerol and sorbitol exhibit larger ΔS_c^*, because, like silica, there is a greater difference between the networks (albeit here H-bonded) in the liquid and solid states.

2.1.4. Viscous Relaxation (TZT_{rlx})

As described above, viscous relaxation historically has been directly tied to the activated process of crystallization, e.g. Equation (2.3). Though related, experimental observation suggests relaxation is generally complete prior to crystallization[22]. Thus, with respect to crystallization, relaxation is the mechanistic analog of pre-equilibrium observed in molecular reaction mechanisms. Furthermore, since activated relaxation is observed above T_m it is reasonable to conclude that TZT for relaxation (TZT_{rlx}) requires a different description than that for TZT_c.

A liquid quenched from high to low temperature or alternatively exposed to a shearing force, must adapt its energy and configurations to accommodate the new free energy landscape. Initially the quenched or sheared system will have excess free energy that must be projected onto the different probability distribution of configurations resulting in a non-ergodic quenched liquid[20]. Relaxation is the process by which atomic/molecular reorganization returns the system to an ergodic probability distribution of configurations. As such the process of relaxation should be highly dependent on its entropy of activation, $\Delta S_{rlx}^{\ddagger}$.

Adam and Gibbs described relaxation in terms of configurational entropy[47], which is in fact a reformulated expression of the classic VFT equation[28-30,51], further modified by Angell to express relaxation in terms of the fragility of the liquid[52]. However, we suggest that the TZT_{rlx} understanding of the temperature dependence of $\Delta S_{rlx}^{\ddagger}$ better describes the temperature dependence of relaxation.

Again it is important to consider the limiting cases at T_K and at T_c. A liquid quenched to T_K will be non-ergodic, having the same large number and probability distribution of accessible configurations, $W_{non\text{-}erg\ l}$, as the original high temperature liquid. Relaxation to reach the Kauzmann condition, $W_c = W_l \approx 1$ at T_K, would require that atomic/molecular reorganization of the entire system becomes cooperative. Thus at T_K we assume $W_{rlx}^{\ddagger} \approx 1$ and $W_{rlx}^{\ddagger}/W_{non\text{-}erg\ l} \rightarrow 0$, and $\Delta S_{rlx}^{\ddagger}$ becomes large and negative. As the temperature increases there is less cooperativity such that the non-ergodic liquid and the relaxed ergodic liquid can both access an increasing number of configurations. Under these conditions the atomic/molecular reorganization is less coupled and numerous transition configurations should also exist. When the temperature is high enough for the liquid to behave like a gas, i.e. the critical temperature T_c (Figure 2.1b), then the non-ergodic and ergodic liquids are indistinguishable, thus

$W_{rlx}^{\ddagger}/W_{non\text{-}erg\ l} \approx 1$ and $\Delta S_{rlx}^{\ddagger} = 0$. Such temperature response to the entropy of activation can be modeled by Equation (2.10), where ΔS_{rlx}^{*} and z_{rlx} are material specific parameters that scale the magnitude of $\Delta S_{rlx}^{\ddagger}$ and modulate the temperature/pressure dependence, respectively.

$$\Delta S_{rlx}^{\ddagger} = \Delta S_{rlx}^{*}\left(\frac{T_c - T}{T - T_K}\right)^{z_{rlx}} \tag{2.10}$$

Similar to crystallization, the attempt frequency pre-factor for relaxation can be treated as an interaction between phonons. However, the resulting vibrational waves exhibit attenuation when traveling through the liquid. Only phonons with the fastest wave velocity can travel through the entire liquid system leading to atomic/molecular rearrangements necessary to make it ergodic. Using the Maxwell material model, the fastest velocity is the speed of sound in the liquid, v_s. Thus the reciprocal of the dynamic viscosity can be expressed as $\frac{1}{\eta} = \sqrt{\frac{G' - v_s^2\rho}{G'}} \bullet \frac{4\pi\nu}{v_s^2\rho}$ [53,54]. ν is the frequency of the shear wave that leads to liquid relaxation, which contains the characteristic frequency of the vibrational modes that lead to the formation of the ergodic liquid from the transition zone and the probability of occurrence of those modes. G' is the elastic constant of the system. Because viscosity is dominant over elasticity in a Newtonian liquid, G' is very large with respect to $v_s^2\rho$ except as T_g is approached, where the liquid becomes more solid-like and more elastic. Applied to TZT_{rlx}, $\frac{4\pi}{v_s^2\rho}\frac{k_B T}{h}$ is the attempt frequency pre-factor.

Combining the pre-factor with the enthalpic and entropic probabilities yields the TZT_{rlx} expression, Equation (2.11).

$$\frac{1}{\eta} = \frac{4\pi}{v_s^2 \rho} \frac{k_B T}{h} \exp\left(\frac{-\Delta H_{rlx}^*}{R(T - T_K)} \right) \exp\left(\frac{\Delta S_{rlx}^*}{R} \left(\frac{T_c - T}{T - T_K} \right)^{z_{rlx}} \right) \tag{2.11}$$

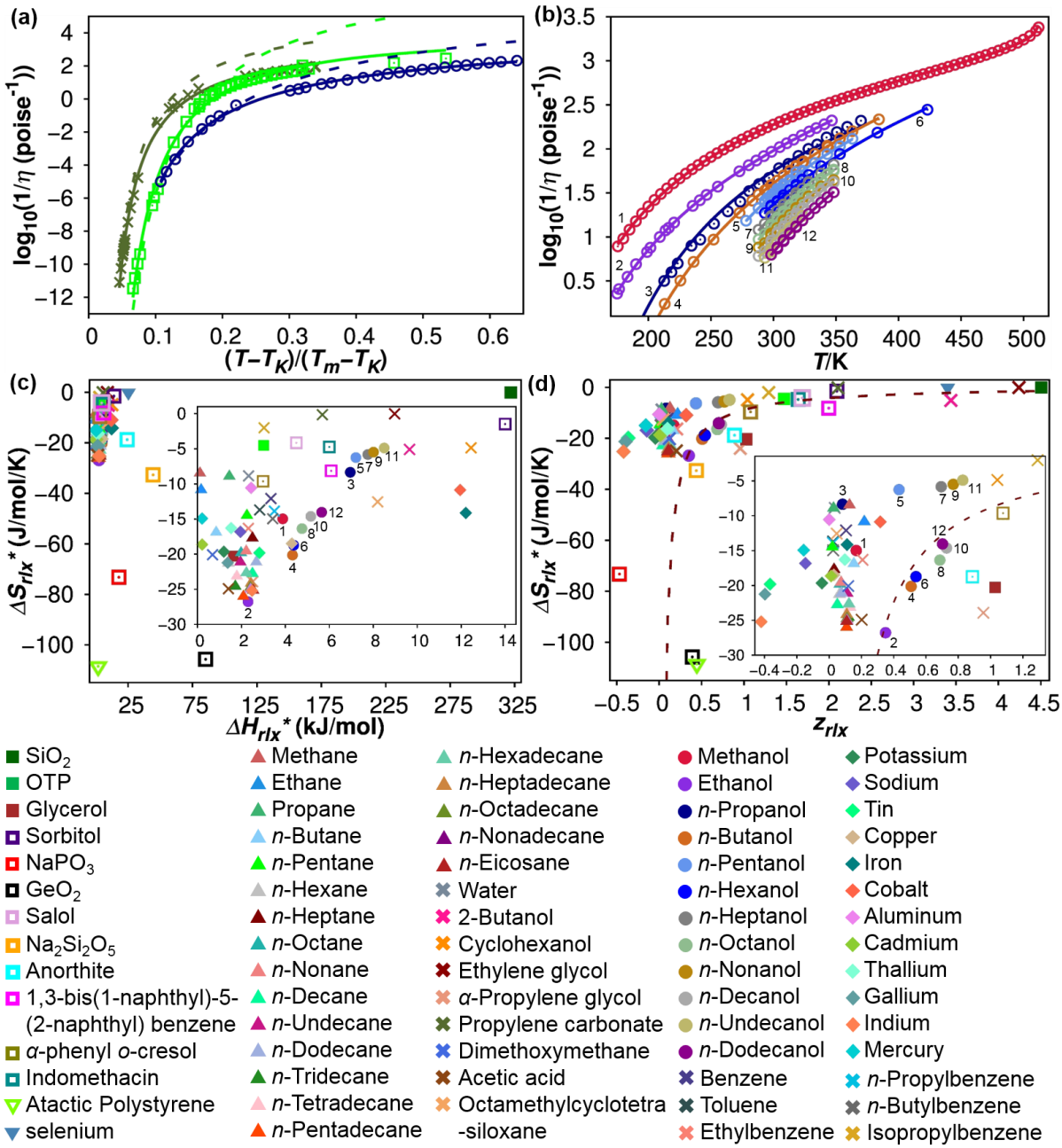

Figure 2.3. Reciprocal viscosity data (symbols) fit to Equation (2.11) (solid lines). (a) Comparison of TZT_{rlx} to VFT fits, Equation (2.1), (dashed line) for o-terphenyl (OTP), n-propanol, and propylene carbonate. (b) TZT_{rlx} fits to the series of n-alcohols C_1 to C_{12}. Plots showing the relationship between (c) ΔH_{rlx}^* and ΔS_{rlx}^* and (d) z_{rlx} and ΔS_{rlx}^*; insets are plotted on an expanded scale. Chain lengths of *n*-alcohols are numbered. Dashed line in (d) is the correlation function $\Delta S_{rlx}^* = -3\text{csch}(z_{rlx}/3)$. Data represented as squares are for compounds with crystallization data reported in Figure 2.2, for which T_c is reported (solid) or is an additional fitting parameter (open).

We do not yet have temperature dependent viscosity data for CZX-1, but are able to test the applicability of Equation (2.11) against extensive literature reports (Figure 2.3 and Appendix Figure B.1 and Table B.2). Temperature dependent viscosity data for this entire series of compounds spanning inorganic and organic, network and molecular materials across a range of reported liquid fragilities, is well fit by Equation (2.11) using the experimentally determined parameters $v_s^2\rho$, T_c and T_K and fitting parameters ΔH_{rlx}^*, ΔS_{rlx}^* and z_{rlx}. As shown in Figure 2.3a, Equation (2.11) provides a superior fit to experimental viscosity data than the classic VFT Equation (2.1), with no need to introduce an arbitrary crossover temperature between VFT and Arrhenius rate laws[32,33]. Unlike any other theories, Equation (2.11) even fits the decrease in viscosity just below T_c reported for methanol (Figure 2.3b) and benzene (Appendix Figure B.1c).

Figure 2.3d shows a similar exponential correlation of the ΔS_{rlx}^* and z_{rlx} parameters, as was observed for crystallization, although with much greater variance. The dashed line in Figure 2.3d is a plot of the same hyperbolic cosecant function observed for TZT_c, which as a point of reference we consider to be the standard correlation. We suspect the greater variance in z_{rlx} results from our fixed T_K approximation when T_K should increase with pressure (see for example reference 55). An increasing value of T_K can be compensated by a smaller value of z_{rlx}. Since reported viscosities generally follow the saturation line, thus are not isobaric, any pressure dependence of T_K will become more apparent in z_{rlx} than for z_c of essentially isobaric crystallization. Our fixed $v_s^2\rho$ approximation, when both are P and T dependent, could also contribute to variance in the parameters. But because the P/T variation is small relative to the magnitude of $v_s^2\rho$[56], its impact on the activation parameters is minimal.

The $\Delta S_{rlx}^{*}/z_{rlx}$ correlations reveal interesting mechanistic insight. An even/odd variation is observed for n-alcohols C_1 to C_{12} with odd chain alcohols exhibiting smaller z_{rlx} than predicted by the correlation function while even chain alcohols fall on the correlation line (Figure 2.3d). This effect is reminiscent of the loose (odd) and close (even) packing of terminal methyl groups of linear alcohols on graphite, attributed to cause lower melting temperatures of odd chain alcohols[57]. Loose packing would be expected to exhibit a greater increase in TK with pressure and thus a smaller value of z_{rlx}. By contrast, GeO_2, anorthite, glycerol and α-propylene glycol exhibit larger values of z_{rlx} than predicted by the standard correlation. Under pressure GeO_2 is known to change from tetrahedral to octahedral coordination[58], and glycerol becomes a more fragile liquid under pressure[59]. The increased fragility with increasing pressure of these systems likely yields decreasing T_K, and thus as modeled here exhibit a larger z_{rlx}. In addition seven of these materials exhibit negative values for z_{rlx}, indicative of an increased $\Delta S_{rlx}^{\ddagger}$ with increasing temperature. These include: Hg, Ga, In and Sn, which exhibit more open covalent structures in their low T/P melts but transition to more metallic close packed structures at higher T/P[60]; the alkali metals Na and K which are bcc metals at low T/P; and $NaPO_3$ for which the rings (LT) vs. chains (HT) of the metaphosphate[61] may account for the negative z_{rlx}. Thus it appears a negative value observed for z_{rlx} is indicative of a low-to-high density structural transition in the liquid.

Activation parameters ΔH_{rlx}^{*} and ΔS_{rlx}^{*} also provide new insight into the physical properties of the liquids, including the strong/fragile conception. Previously noted to correlate with the VFT parameter[52], the fragility parameter exhibits modest correlation to the free energy of activation, $\Delta G_{rlx}^{\ddagger}$, calculated with TZT_{rlx} parameters at T_g. However, as visualized by Figure 2.3c, $\Delta G_{rlx}^{\ddagger}$, and thus the strength/fragility of a liquid, can be partitioned into enthalpic and

entropic components. In this regard it is notable that SiO_2 and GeO_2, both strong network liquids, appear to be respectively, enthalpically and entropically strong. This is consistent with structural and spectroscopic studies that suggest Ge is more coordinatively flexible than Si[58]. Similarly, while n-alcohols exhibit consistently increasing viscosity with increasing chain length (Figure 2.3b), the ΔH_{rlx}^* and ΔS_{rlx}^* parameters demonstrate dramatic odd/even chain length dependence (Figure 2.3c). The viscosity of odd chain length alcohols being more enthalpically dependent whereas even chain alcohols are more entropically dependent, is likely indicative of differential molecular packing[57]. In addition, ΔH_{rlx}^* and ΔS_{rlx}^* values for n-alkanes (Appendix Table B.2) exhibit odd/even effects for short chains known to prefer linear conformations but not for long chains $n \geq 16$ which prefer folded conformations[62]. These examples demonstrate that TZT_{rlx} not only provides a superior fit of temperature dependent viscosity data, but it also offers insight into enthalpic and entropic control of relaxation.

2.1.5. Conclusion

We articulate the new transition zone theory for condensed phase reactions by extending the concept of transition state theory to consider transition zones, and, building upon the Kauzmann concept, recognize the temperature (and pressure) dependence of the activation parameters. TZT, using only the non-empirical enthalpic ΔH^* and entropic ΔS^* activation parameters, along with a single empirical parameter z which itself is strongly correlated to ΔS^*, provides a superior description of crystallization and relaxation rate data than any previously reported theories. Comparison of the $\Delta S^*/z$ correlation for crystallization and relaxation suggests that articulation of the pressure dependence of T_K will further eliminate the empiricism of the z parameter. Importantly, TZT, unlike CNT, ICG, VFT and WLF theories

does not require the imposition of an arbitrary mechanistic shift from non-Arrhenius to Arrhenius behavior.

For both crystallization and relaxation, ΔH^* parameters provide mechanistic insight into the nature of the intermolecular/atomic interactions that must reorganize during the transformation. ΔS^* parameters demonstrate the extent of structural organization necessary for the transformation. Both parameters are modulated by the extent of cooperativity required for the transformation, with limits of complete cooperativity at T_K, and its absence with respect to crystallization at T_m, and relaxation at T_c. The parameter z, which modulates the T/P dependence of $\Delta S^{\ddagger}$, is useful to differentiate liquids with respect to T/P induced changes in their structure. Together these parameters deepen the insight given by the classic concept of fragility, in that they articulate whether the strength of a liquid is enthalpic or entropic, which for example describes the distinct character of SiO_2 and GeO_2 networks, and chain length effects in n-alcohols and n-alkanes.

As demonstrated in the examples above, TZT provides a common framework for understanding the processes of crystallization and relaxation, but equally demonstrates they are distinct. They are clearly distinct with respect to the temperature dependence of the ratio of microstates accessible to reactant and TZ. Both crystallization and relaxation are rate limited by phonon propagation through the liquid phase. They are distinct, however, in that crystallization requires a standing wave type organization of phonons at the crystallization front with a characteristic wavelength of twice the unit cell dimension, whereas viscous relaxation requires phonons that can transverse the entirety of the liquid and thus are traveling at the speed of sound in the liquid. Because of their distinct characteristics, viscosity should not be used as the activation term to describe crystal growth. This result raises interesting

questions with regard to the extensive literature built upon the conception of the reduced growth rate, i.e. the product of the crystal growth rate and viscosity. Nevertheless, ongoing development of TZT is pointing toward a relationship between these two distinct processes as a key to the unresolved question of the origin of the glass transition[1].

2.2. Mathematical Derivation of the Pre-factor in TZT

2.2.1. Introduction

Being built on Boltzmann distribution of atomic or molecular collisions, transition state theory[34] describes the rate constant of a molecular reaction as the product of an atomic or molecular collision attempt frequency and the probability of the reactants being activated to the transition state. The activated complex has a vibrational degree of freedom that corresponds to the decomposition of the activated complex into the products. If the frequency of that vibrational degree of freedom is ν, the weighted number of states, using classical theory, is $\frac{k_B T}{h\nu}$. Due to the small curvature of the transition state on the potential energy surface, this vibrational degree of freedom can also be treated as a translational degree of freedom, which is often described as the passage over the activation barrier and the speed of which is expressed as the product of the frequency of this vibrational degree of freedom and the number of states, i.e., $\frac{k_B T}{h\nu} \times \nu = \frac{k_B T}{h}$, thus the pre-factor in the Eyring equation[34].

However, Adam and Gibbs have noted that cooperative rearrangements of groups of particles, instead of single molecules passing over an activation barrier, are required to describe the activated processes in the condensed phase[47]. Correspondingly, as an extension of the transition state theory concept[34], transition zone theory considered a Boltzmann distribution of

interacting phonons in the condensed phase, and a transition zone through which the condensed phase reaction must traverse[35]. The interacting phonons result in a characteristic frequency, ν, at which some unit of matter transforms from a non-ergodic to ergodic liquid or a non-crystalline to crystalline phase, analogous to the passage over the activation barrier in transition state theory. The corresponding weighted number of states is thus $\frac{k_B T}{h\nu}$. In this section, the transformation from the transition zone to the crystalline phase and to the ergodic liquid will be explained for crystal growth and viscous relaxation, respectively, and detailed derivation of the pre-factor of transition zone theory will be shown.

2.2.2. Formation of the Crystalline Phase from the Transition Zone

While the local structure in liquid and crystalline phases of congruently melting systems is essentially equivalent, crystals uniquely exhibit long-range order. Therefore, the liquid must undergo substantial molecular rearrangements to form the long-range order in the crystal from transition zone. Those rearrangements result in vibrational waves, or interacting phonons, that propagate through the liquid. When the interacting waves create a standing wave pattern throughout the liquid system, a periodic structure is formed, and the liquid transforms into the crystal. Therefore, formation of the long-range order in the crystal from the intermediate-range order in the transition zone corresponds to a characteristic frequency, ν_c, and wavelength, λ_c, of interacting phonons that result in a standing wave pattern.

To obtain ν_c and λ_c, a simplified model was used as a starting approximation, which is a one-dimensional chain of hard spheres with the same mass, m, and each sphere is connected to its two neighboring spheres by springs, while all the springs have the same spring constant,

k (Figure 2.4). To the first approximation, each sphere is assumed to only interact with its two nearest neighbors.

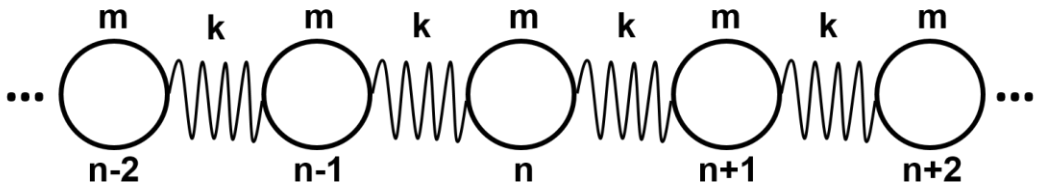

Figure 2.4. Simplified model for the formation of periodic crystalline structure.

If the chain is in the x dimension, and the displacement of the *n*th sphere is x_n, then applying Hooke's law to the *n*th sphere,

$$F_n = k\left(x_{n+1} - x_n\right) - k\left(x_n - x_{n-1}\right) \tag{2.12}$$

According to Newton's second law, Equation (2.12) can be written as

$$m\frac{\partial^2 x_n}{\partial t^2} = k\left(x_{n+1} - 2x_n + x_{n-1}\right) \tag{2.13}$$

The same equations can be written for all of the other spheres. To form a periodic structure in the chain, all the spheres need to oscillate with the same amplitude *A* and the same angular frequency ω, resulting in propagating waves in the chain with the same amplitude and frequency. Solving them simultaneously and assuming harmonic oscillation

$$\begin{aligned} &\cdots \\ &x_{n-1} = A\exp\left(-i\left(\omega t - qx_{n-1,0}\right)\right) \\ &x_n = A\exp\left(-i\left(\omega t - qx_{n,0}\right)\right) \\ &x_{n+1} = A\exp\left(-i\left(\omega t - qx_{n+1,0}\right)\right) \\ &\cdots \end{aligned} \tag{2.14}$$

where *q* is the wave vector (wave number for one dimensional wave) with the magnitude of $2\pi/\lambda$ where λ is the wavelength, and $x_{n,0}$ is the equilibrium position of the *n*th sphere on the

chain. Since the transition zone has the same short- and intermediate-range order as the crystal, to form a one-dimensional lattice chain with lattice constant *a*, the equilibrium position of the *n*th sphere should be *na*. Substitute into Equation (2.14)

$$\begin{aligned} &\cdots \\ &x_{n-1} = A\exp\left(-i\left(\omega t - q\left(n-1\right)a\right)\right) \\ &x_n = A\exp\left(-i\left(\omega t - qna\right)\right) \\ &x_{n+1} = A\exp\left(-i\left(\omega t - q\left(n+1\right)a\right)\right) \\ &\cdots \end{aligned} \tag{2.15}$$

Substitute Equation (2.15) into Equation (2.13)

$$\begin{aligned} &-mA\omega^2\exp\left(-i\omega t\right)\exp\left(iqna\right) = \\ &k\left(A\exp\left(-i\omega t\right)\exp\left(iq(n+1)\mathrm{a}\right) - 2A\exp\left(-i\omega t\right)\exp\left(iqna\right) + A\exp\left(-i\omega t\right)\exp\left(iq(n-1)\mathrm{a}\right)\right) \end{aligned}$$

(2.16)

Rearranging Equation (2.16) by dividing $A\exp(-i\omega t)\exp(iqna)$ on both sides and by realizing $exp(ix) = cos(x)+isin(x)$:

$$m\omega^2 = 2k\left(1-\cos\left(qa\right)\right) \tag{2.17}$$

Therefore

$$\omega = \sqrt{\frac{4k}{m}}\left|\sin\left(\frac{qa}{2}\right)\right| \tag{2.18}$$

The periodicity of the plot of ω against q (Figure 2.5) suggests that the frequency (Equation (2.18)) and the displacement of the sphere (Equation (2.15)) do not change when q is changed by $q\pm 2\pi/a$, which means the solutions at q and $q\pm 2\pi/a$ are physically identical. Therefore, the region between $q = -\pi/a$ and $q = \pi/a$, which is the first Brillouin zone, contains all the independent solutions and is the only region that needs to be considered.

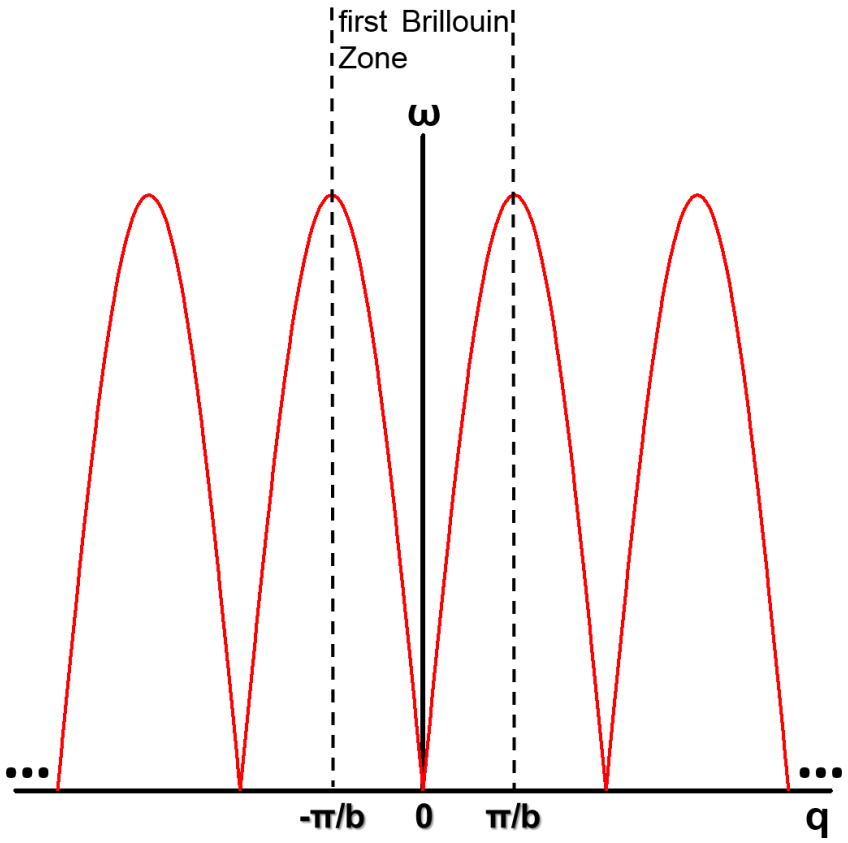

Figure 2.5. Plot of ω against q. The boundaries of the first Brillouin zone are shown as dashed lines.

The group velocity of the propagating wave packets in the chain, which is also the velocity for the propagation of energy, is the first derivative of ω against q, $d\omega/dq$. At the boundary of the first Brillouin zone, the group velocity and the transmission velocity of the energy are zero, thus the wave is standing, with the corresponding wavelength $\lambda = 2\pi/q = 2a$, and a periodic crystalline phase is formed. Therefore, the characteristic wavelength of the formation of standing wave pattern is $\lambda_c = 2a$, and with the characteristic frequency being ν_c and thus the weighted number of states being $\frac{k_B T}{h\nu_c}$, the velocity of transformation from the

transition zone to the crystalline phase is $\lambda_c \nu_c \times \frac{k_B T}{h \nu_c} = \lambda_c \frac{k_B T}{h} = 2a \frac{k_B T}{h}$, hence the pre-factor in transition zone theory of crystal growth.

For three dimensional crystal growth with non-isotropic lattices, the averaged lattice constant, which is the cube root of the volume of the unit cell, is used as a first approximation of *a*. However, for anisotropic crystal growth, such as lamellar growth in polymers, different lattice constant may be needed in each dimension.

2.2.3. Formation of Ergodic Liquid from the Transition Zone

When a liquid is quenched from high to low temperature or exposed to a shearing force, it will initially project its excess free energy and probability distribution of configurations onto a changed free energy landscape, resulting in a non-ergodic liquid. Relaxation is the process which returns the non-ergodic liquid to an ergodic liquid to accommodate the new free energy landscape through atomic/molecular reorganization. Those atomic/molecular reorganization leads to longitudinal waves propagating through the liquid, and due to the viscosity of the liquid, those longitudinal waves are attenuated, yet some of them, such as the sound wave in the liquid, can still propagate through the whole liquid system despite the attenuation, which adjust the probability distribution of configurations of the whole liquid system and transforms it to be ergodic. Therefore, relaxation of the liquid corresponds to the frequency and velocity of those longitudinal waves that propagate throughout the whole system.

Each longitudinal wave propagating through a material applies an oscillatory force (stress) to the material, which results in energy transmission and atomic/molecular displacement (strain). In purely elastic materials, such as most crystalline solids, the stress and

strain occur in phase, thus the response of one occurs simultaneously with the other. In purely viscous materials, such as Newtonian fluids, there is a 90° ($\pi/2$ radian) phase lag between strain and stress. In viscoelastic materials, such as some polymeric liquids, strain exhibits a phase lag to stress that is between 0 and 90°. Assuming harmonic oscillation with the longitudinal waves, strain (ε) and stress (σ) can be expressed as

$$\begin{aligned} \varepsilon &= \varepsilon_0 \exp\left(i\omega t\right) \\ \sigma &= \sigma_0 \exp\left(i\left(\omega t + \delta\right)\right) \end{aligned} \tag{2.19}$$

where ε_0 and σ_0 are the amplitude of strain and stress oscillation, respectively, i is the imaginary unit, ω is the angular frequency of the oscillation, t is time, and δ is the phase lag between strain and stress. For convenience and with Euler's formula ($\exp(i\theta) = \cos(\theta) + i\sin(\theta)$), stress can be written as a complex quantity, the real part of which is in phase with the strain and the imaginary part of which is 90° out of phase with the strain

$$\sigma = \sigma_0 \exp\left(i\delta\right)\exp\left(i\omega t\right) = \left(\sigma_0 \cos\left(\delta\right) + i\sigma_0 \sin\left(\delta\right)\right)\exp\left(i\omega t\right) \tag{2.20}$$

The dynamic modulus is therefore defined as

$$G = \frac{\sigma}{\varepsilon} = \frac{\sigma_0}{\varepsilon_0}\cos\left(\delta\right) + i\frac{\sigma_0}{\varepsilon_0}\sin\left(\delta\right) \tag{2.21}$$

where the real part, $\sigma_0 \cos(\delta)/\varepsilon_0$, and the imaginary part, $\sigma_0 \sin(\delta)/\varepsilon_0$, are the storage and loss modulus, respectively.

The Maxwell material model can be used as an approximation to calculate the dynamic modulus of a viscoelastic system, which describes the system as a spring and a dashpot connected in series. The spring obeys Hooke's law, models the instantaneous bond deformation of the material, and accounts for the fraction of the energy stored reversibly as strain energy, while the dashpot is described as a Newtonian fluid and accounts for the

attenuation of the wave propagation and the loss of the energy transmission in the system. In a series of spring and dashpot, the total strain is the sum of the strain in each element, while the stress on each element is the same and equal to the imposed stress:

$$\begin{aligned} \varepsilon &= \varepsilon_s + \varepsilon_d \\ \sigma &= \sigma_s = \sigma_d \end{aligned} \tag{2.22}$$

where the subscripts s and d represent the spring and the dashpot, respectively. Taking the first derivative of the strain equation with respect to time

$$\frac{d\varepsilon}{dt} = \frac{d\varepsilon_s}{dt} + \frac{d\varepsilon_d}{dt} = \frac{1}{E}\frac{d\sigma_s}{dt} + \frac{\sigma_d}{\eta} = \frac{1}{E}\frac{d\sigma}{dt} + \frac{\sigma}{\eta} \tag{2.23}$$

where η is the viscosity represented by the dashpot, in which the stress produces a strain rate $\sigma_d = \eta\, d\varepsilon_d/dt$, and E is the elastic modulus of the spring. Substituting Equations (2.19) into Equation (2.23)

$$\begin{aligned} i\omega\varepsilon_0 \exp\left(i\omega t\right) &= \frac{i\omega\sigma_0}{E}\exp\left(i\left(\omega t+\delta\right)\right) + \frac{\sigma_0 \exp\left(i\left(\omega t+\delta\right)\right)}{\eta} \\ \varepsilon_0 &= \frac{\sigma_0 \exp\left(i\delta\right)}{E} + \frac{\sigma_0 \exp\left(i\delta\right)}{i\omega\eta} \end{aligned} \tag{2.24}$$

Therefore, the dynamic modulus of the system is

$$\begin{aligned} G = \frac{\sigma}{\varepsilon} &= \frac{\sigma_0 \exp\left(i\left(\omega t+\delta\right)\right)}{\varepsilon_0 \exp\left(i\omega t\right)} = \frac{\sigma_0 \exp\left(i\delta\right)}{\varepsilon_0} = \frac{\sigma_0 \exp\left(i\delta\right)}{\dfrac{\sigma_0 \exp\left(i\delta\right)}{E} + \dfrac{\sigma_0 \exp\left(i\delta\right)}{i\omega\eta}} \\ &= \frac{1}{\dfrac{1}{E} + \dfrac{1}{i\omega\eta}} = \frac{E\eta^2\omega^2}{E^2+\omega^2\eta^2} + i\frac{E^2\eta\omega}{E^2+\omega^2\eta^2} \end{aligned} \tag{2.25}$$

The real and imaginary parts are the storage and loss modulus, respectively. Comparing Equation (2.25) to Equation (2.21), the phase lag angle, δ, can be expressed as

$$\tan(\delta) = \frac{\frac{\sigma_0}{\varepsilon_0}\sin(\delta)}{\frac{\sigma_0}{\varepsilon_0}\cos(\delta)} = \frac{\frac{E^2\eta\omega}{E^2+\omega^2\eta^2}}{\frac{E\eta^2\omega^2}{E^2+\omega^2\eta^2}} = \frac{E}{\eta\omega} \tag{2.26}$$

For purely elastic systems, $\eta \to \infty$, thus $G = E$, $E/\eta\omega = 0$, and $\delta = 0$. Therefore, there is no loss modulus, which indicates all energy transmitting in the system is stored reversibly, and stress and strain occur in phase. For purely viscous systems, $E \to \infty$, thus $G = i\eta\omega$, $E/\eta\omega = \infty$, and $\delta = 90°$. Therefore, there is no storage modulus, which indicates all waves and energy propagating in the system are attenuated, and there is a 90° phase lag between strain and stress.

Liquid, as a continuous medium, can be divided into numerous small volumes in each dimension, with each volume having the area A perpendicular to the dimension and length δx in the dimension (Figure 2.6).

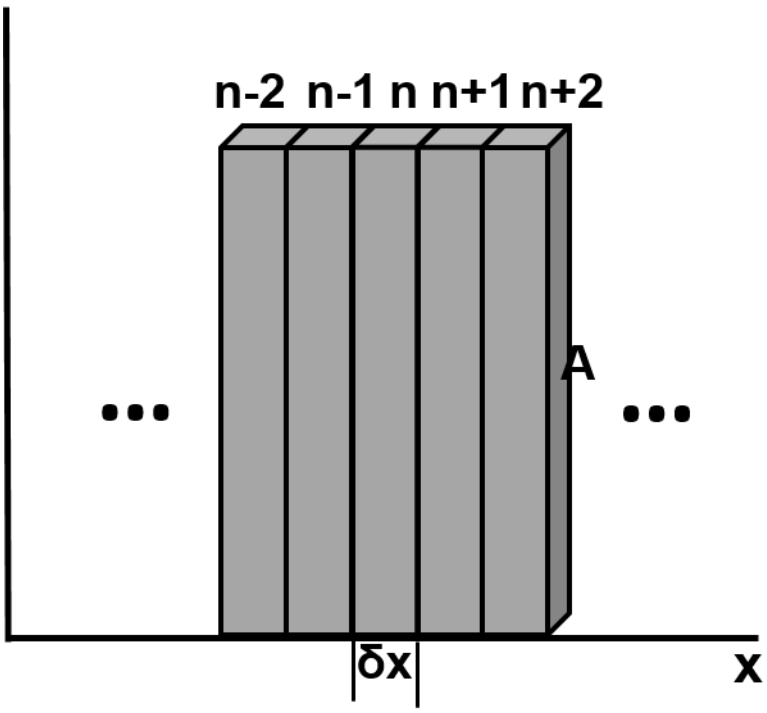

Figure 2.6. Simplified model of longitudinal waves traveling in the liquid, where the liquid is divided into numerous small volumes in the *x* dimension. Only the *x* dimension is shown in this graph. The *y* and *z* dimensions can be represented and analyzed in the same way.

When a longitudinal wave propagates in the medium, a pressure gradient is present. For the *n*th volume, if the pressure is p_1 on its left side and p_2 on its right side, then the force in the *x* direction is

$$F = \left(p_1 - p_2 \right) A = \Delta p A \tag{2.27}$$

According to Newton's second law, when δx is infinitesimal

$$\begin{aligned} F &= ma \\ \Delta p A &= \rho A \delta x \left(\frac{\partial^2 s_n}{\partial t^2} \right) \\ \frac{\Delta p}{\delta x} &= \rho \left(\frac{\partial^2 s_n}{\partial t^2} \right) \\ \frac{\partial p}{\partial x} &= \rho \left(\frac{\partial^2 s_n}{\partial t^2} \right) \end{aligned} \tag{2.28}$$

where m and ρ are the instantaneous mass and density of the nth volume, respectively, and s_n is the displacement of the nth volume in the medium.

As an approximation, each volume is modeled as the Maxwell material, i.e., a series of spring and dashpot. The dynamic modulus of the nth volume is

$$G = \frac{stress}{strain} = \frac{p_1 - p_2}{\left(V_f - V_i\right)/V_i} = \frac{\Delta p}{\Delta V/V_i} \tag{2.29}$$

where V_i and V_f are the initial and final volume of the nth volume.

During the propagation of the longitudinal plane wave, for the nth volume, the displacement of the right side and that of the left side are different due to the pressure gradient, and if the difference in displacement is Δs_n, then for infinitesimal δx

$$\begin{aligned} V_i &= A\delta x \\ V_f &= A\left(\delta x + \Delta s_n\right) \\ \frac{V_f - V_i}{V_i} &= \frac{\left(A\left(\delta x + \Delta s_n\right) - A\left(\delta x\right)\right)}{A\delta x} = \frac{\Delta s_n}{\delta x} = \frac{\partial s_n}{\partial x} \end{aligned} \tag{2.30}$$

Thus

$$\Delta p = G\frac{\Delta V}{V_i} = G\frac{\partial s_n}{dx} \tag{2.31}$$

Substitute Equation (2.31) into Equation (2.28)

$$\frac{\partial p}{\partial x} = \frac{\partial}{\partial x}\left(G\frac{\partial s_n}{dx}\right) = G\frac{\partial^2 s_n}{\partial x^2} = \rho\left(\frac{\partial^2 s_n}{\partial t^2}\right) \tag{2.32}$$

Under the harmonic assumption of the longitudinal plane waves, a solution to Equation (2.32) is

$$s_n = s_0 \exp\left(i\left(qx_n - \omega t\right)\right) \tag{2.33}$$

Equation (2.33) is the displacement of the medium with the propagating longitudinal plane wave with the angular frequency ω, in which s_0 is the amplitude of the displacement, q is the wave vector, and x_n is the position of the nth volume in the x dimension. Substitute Equation (2.33) back into Equation (2.32)

$$\begin{aligned} & G\frac{\partial^2}{\partial x^2}\left(s_0\exp\left(i\left(qx_n-\omega t\right)\right)\right)=-Gs_0q^2\exp\left(i\left(qx_n-\omega t\right)\right) \\ & =\rho\frac{\partial^2}{\partial t^2}\left(s_0\exp\left(i\left(qx_n-\omega t\right)\right)\right)=-\rho s_0\omega^2\exp\left(i\left(qx_n-\omega t\right)\right) \\ & q^2=\left(\frac{\rho}{G}\right)\omega^2 \end{aligned} \tag{2.34}$$

For purely viscous or viscoelastic systems, G is a complex number due to the phase lag between strain and stress. Since density and frequency are both real numbers, the wave vector q must be a complex number, which indicates that part of the longitudinal wave propagate through the liquid and the energy transmitted with it is stored reversibly, and part of it is attenuated. The velocity of the propagating longitudinal waves should depend on the storage part of the wave, and the velocity of the wave propagation, v_c, can be expressed as[54]

$$v_c = \frac{\omega}{R(q)} = \frac{\omega}{R\left(\sqrt{\frac{\rho\omega^2}{G}}\right)} = \frac{1}{R\left(\sqrt{\frac{\rho}{\frac{E\eta^2\omega^2}{E^2+\omega^2\eta^2} + i\frac{E^2\eta\omega}{E^2+\omega^2\eta^2}}}\right)}$$

$$= \frac{1}{\sqrt{\frac{\rho}{\left(\frac{E\eta^2\omega^2}{E^2+\omega^2\eta^2}\right)^2 + \left(\frac{E^2\eta\omega}{E^2+\omega^2\eta^2}\right)^2}} \cdot R\left(\sqrt{\frac{E\eta^2\omega^2}{E^2+\omega^2\eta^2} - i\frac{E^2\eta\omega}{E^2+\omega^2\eta^2}}\right)}$$

$$= \sqrt{\frac{2\left(\left(\frac{E\eta^2\omega^2}{E^2+\omega^2\eta^2}\right)^2 + \left(\frac{E^2\eta\omega}{E^2+\omega^2\eta^2}\right)^2\right)}{\rho\left(\left(\frac{E\eta^2\omega^2}{E^2+\omega^2\eta^2}\right) + \sqrt{\left(\frac{E\eta^2\omega^2}{E^2+\omega^2\eta^2}\right)^2 + \left(\frac{E^2\eta\omega}{E^2+\omega^2\eta^2}\right)^2}\right)}} \tag{2.35}$$

where $R(q)$ means the real part of the complex number q.

Solve Equation (2.35) for viscosity

$$\frac{1}{\eta} = \sqrt{\frac{E-\rho v_c^{\,2}}{E}} \cdot \frac{2\omega}{\rho v_c^{\,2}} \tag{2.36}$$

Most non-polymeric liquids can be approximated as purely viscous unless the glass transition temperature is approached, thus $E \to \infty$ and $G = i\eta\omega$, and Equation (2.36) becomes

$$\frac{1}{\eta} = \frac{2\omega}{\rho v_c^{\,2}} = \frac{4\pi\nu}{\rho v_c^{\,2}} \tag{2.37}$$

Due to the attenuation, only the longitudinal waves with the fastest wave velocity can propagate through the entire liquid system, and sound wave is one of them, thus v_c is the speed of sound in the liquid. The frequency, ν, in Equation (2.37), is the frequency of the longitudinal wave that leads to liquid relaxation, which contains the characteristic frequency of the

vibrational modes, v_c, that lead to the formation of the ergodic liquid from the transition zone, and the probability of occurrence of those modes, represented by the enthalpy and entropy of activation in transition zone theory for viscous relaxation (TZT_{rlx}). Therefore, the pre-factor in TZT_{rlx} is $\frac{4\pi v_c}{\rho v_c^{\,2}} \times \frac{k_B T}{h v_c} = \frac{4\pi}{\rho v_c^{\,2}} \frac{k_B T}{h}$.

TZT_{rlx} with the pre-factor $\frac{4\pi}{\rho v_c^{\,2}} \frac{k_B T}{h}$ accurately describes viscosity of diverse non-polymeric liquids over the temperature range T_g (glass transition temperature) to T_c (critical point). However, polymeric liquids and some non-polymeric liquids at temperatures close to T_g should not be treated as purely viscous liquids, and thus both the storage (elasticity) and the loss (viscosity) moduli need to be considered, and Equation (2.36) is needed to describe relaxation.

2.2.4. Conclusion

We presented detailed derivation of the pre-factor in transition zone theory for crystal growth from the melt and liquid viscous relaxation. Both crystal growth and relaxation are related to phonon propagation through the liquid, however, the formation of the periodic crystalline structure requires the formation of a standing wave pattern in the liquid through interaction of vibrational modes with characteristic wavelength of twice the unit-cell dimension, and the formation of the ergodic liquid requires the propagation of the longitudinal plane waves throughout the entire liquid system, thus traveling with the velocity of sound in the liquid. Those derivation assists with understanding of transition zone theory mathematically, and provides part of a common framework for understanding the processes of

crystallization and relaxation, which serves as a foundation to further extend transition zone theory into fields such as crystallization and relaxation of polymeric liquids as well as to explain the origin of the glass transition.

2.3. Application of TZT: Spherulite Growth of Crystalline Polymers

When a polymer crystallizes, the polymer chains fold and align to form ordered regions, lamellae, which further compose large spheroidal structures, or spherulites. Due to the amorphous regions in the spherulites formed by the lamellae, most crystalline polymers are semicrystalline. Nevertheless, similar to crystal growth of non-polymeric materials, the rate of spherulite crystal growth of polymers can be measured by optical microscopy, in which the size of the spherulites are measured as a function of time. In order to test and broaden the applicability of TZT_c as well as to further understand the fundamental processes during spherulite growth such as the organization of chemical bonds and the polymer chains, TZT_c is applied to the kinetics of spherulite growth of crystalline polymers.

The spherulite growth rate vs. temperature data of eight polymers, as well as selenium which also exhibits spherulite growth similar to polymers, are obtained directly from literature or extracted from digitized images of published figures. As shown in Figure 2.7a, TZT_c accurately describes the kinetics of spherulite growth for all nine materials using experimentally measured λ, T_K and T_m and fitting parameters ΔH_c^*, ΔS_c^* and z_c. Tabulation of fitting parameters and references are given in Appendix Table B.1.

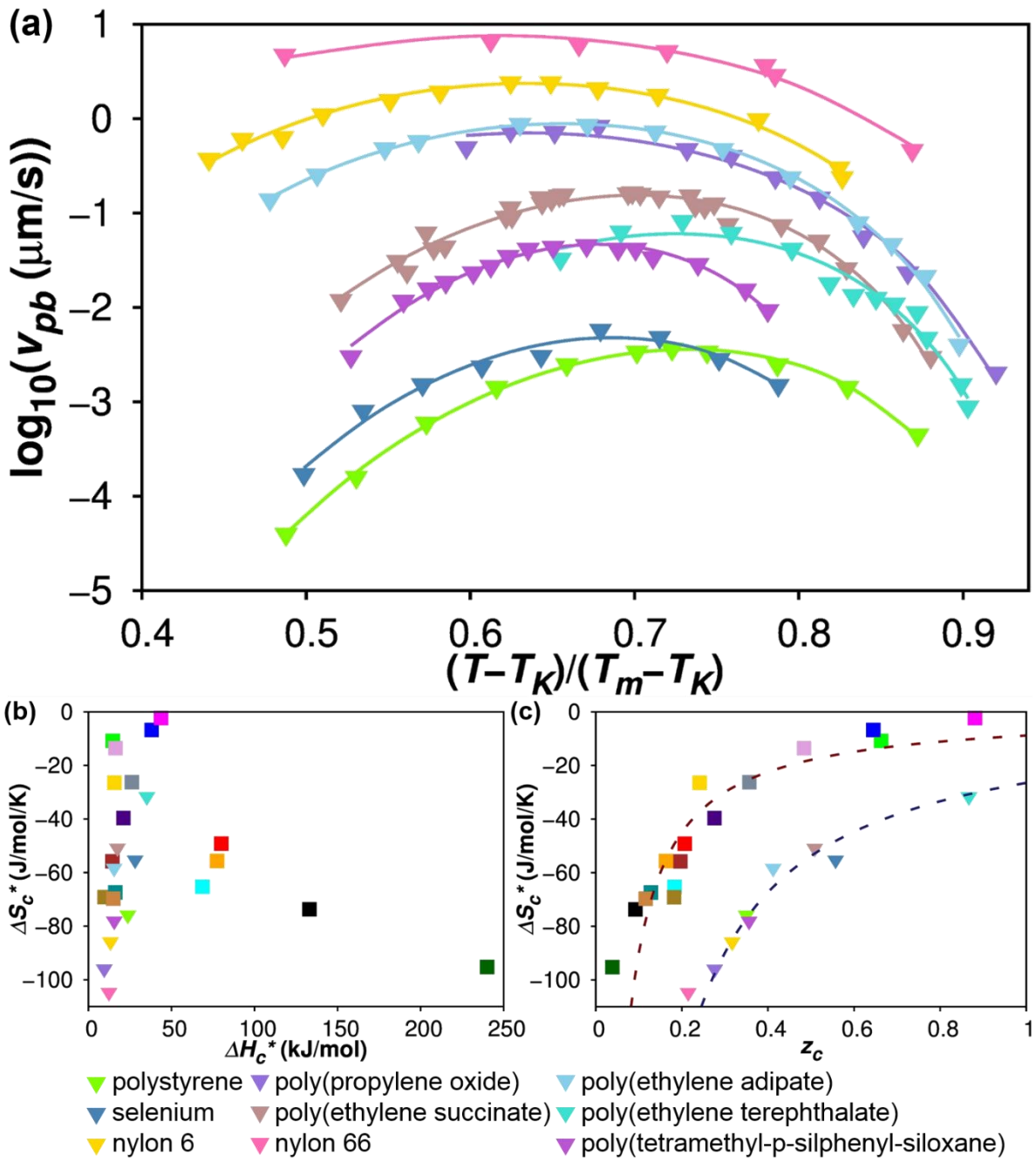

Figure 2.7. (a) Experimental rates of spherulite growth data points with lines of the best fit to Equation (2.9), plotted with respect to the normalized temperature $(T\text{-}T_K)/(T_m\text{-}T_K)$. (b) Replot of Figure 2.2b, with correlation between ΔH_c^* and ΔS_c^* of spherulite crystal growth added. (c) Replot of Figure 2.2c, with correlation between z_c and ΔS_c^* of spherulite crystal growth and the correlation line $\Delta S_c^* = -9\text{csch}(z_c/3)$ (blue dashed) added.

As shown in Figure 2.7b, spherulite growth of crystalline polymers exhibit relatively low ΔH_c^* and more negative ΔS_c^*. The relatively low ΔH_c^* indicates relatively weaker intermolecular forces and less chemical bond breaking/forming, which is consistent with the chain-folding mechanism of spherulite growth of crystalline polymers. Meanwhile, the more negative ΔS_c^* indicates significant structural difference between the amorphous phase and the spherulites, such that substantial structural rearrangement by polymer chain folding is required to achieve a more crystal-like TZ_c structure.

Further investigation of the correlation between the fitting parameters also suggests a strong correlation between ΔS_c^* and z_c, yet different from the correlation observed in the TZT_c fits for crystal growth of non-polymeric materials. This correlation can also be described by a hyperbolic cosecant function, $\Delta S_c^* = -9\text{csch}(z_c/3)$, as shown in Figure 2.7c. Under the hypothesis of the correlation constant 3 being related to the three dimensionality of crystal growth for non-polymeric systems, the correlation constant -9 can be treated as -3×3, and thus the correlation function for spherulite growth of crystalline polymers is essentially the correlation function for crystal growth of non-polymers ($\Delta S_c^* = -3\text{csch}(z_c/3)$) multiplied by 3. When such correlation function is substituted back into the entropy of activation, the entropic probability term becomes

$$\exp\left(\frac{-3\times 3\,\text{csch}\left(z_c/3\right)}{R}\left(\frac{T-T_K}{T_m-T}\right)^{z_c}\right)=\left(\exp\left(\frac{-3\,\text{csch}\left(z_c/3\right)}{R}\left(\frac{T-T_K}{T_m-T}\right)^{z_c}\right)\right)^3 \qquad (2.38)$$

Therefore, the correlation between ΔS_c^* and z_c indicates that the entropic probability of spherulite growth of crystalline polymers is the cube of a similar form of entropic probability of crystal growth of non-polymers. One possible explanation to that is when polymers crystallize, the ordering of polymer chains only occur in the two dimensions of polymer chain

aligning instead of three, and depending on the orientation of the polymer, there are three possible ways (*x* and *y*, or *x* and *z*, or *y* and *z* dimensions) to choose two dimensions of chain aligning out of three, thus the overall entropic probability for spherulite growth is the entropic probability for ordering in each pair of the two dimensions (P) multiplied by itself twice (P*P*P), or cubed (P^3).

To conclude, TZT_c accurately describes the spherulite growth of crystalline polymers, in which the relatively low ΔH_c^* and the more negative ΔS_c^* indicate less chemical bond breaking/folding yet significant structural reorganization by polymeric chain folding, and the correlation between ΔS_c^* and z_c possibly suggests the two-dimensional ordering of polymer chains.

2.4. Application of TZT: Viscosity of Liquid Sulfur

2.4.1. Introduction

The viscosity of liquid sulfur changes significantly with temperature. It has been observed that upon being heated from its melting point, the viscosity of sulfur first decreases slowly, and after reaching a minimum at around 154 °C, it increases rapidly by over four orders of magnitude to a maximum at around 187 °C, after which it decreases slowly as temperature increases. This distinct phenomenon has been observed since measured by Bacon and Fanelli in 1943[63], and it has been shown that the sudden rise of viscosity is due to the polymerization of liquid sulfur at approximately 159 °C: below the polymerization temperature (T_p) liquid sulfur is consist of 8-membered rings, while above T_p it is consist of long sulfur chains, and the increased viscosity is characteristic of long-chain polymers. Polymerization of liquid sulfur in which sulfur rings open up to reconnect into polymer chains has been shown to be reversible,

yet its mechanism is still being debated. Some has viewed it as an equilibrium mixture of monomer rings and polymer chains[64], while some has viewed it as a phase transition in between first and second order based on calorimetric data[65].

Several mechanisms have been proposed to explain the distinct temperature dependence of the viscosity of liquid sulfur, yet most of them are highly empirical and do not accurately describe the experimental results. The most common one suggested that liquid sulfur can be viewed as a pseudo-solution, with the polymeric chains being the solute and the eight-membered sulfur rings being the solvent. The viscosity of sulfur depends on the viscosity of the solvent, the length of the polymeric sulfur chains, and the weight fraction of the polymeric chains in the pseudo-solution. The viscosity of the solvent is usually fitted with an Arrhenius type function, and the total viscosity of the liquid is fitted with a polynomial function of the weight fraction and the length of the polymeric chains[66,67]. This mechanism can only fit viscosity in a limited range of temperature, and the parameters used in the Arrhenius function and the polynomial are completely empirical.

Meanwhile, Eyring has proposed transition state theory[34] and applied it to liquid viscosity[45]. The application assumed that liquid flow occurs based on successive movements of each individual molecule or each small segment for large molecules such as long – chain hydrocarbons and polymers, and the size of each segment is approximately the same for large molecules of all sizes. The probability of a movement of one segment that leads to the liquid flow only depends on its cooperation with other segments, which the authors claimed to be temperature independent. Enthalpy of activation of fluidity (reciprocal of viscosity) was related to the enthalpy of evaporation, while entropy of activation involves averaged chain length of the macromolecules. The parameters obtained this way are highly empirical, and the authors

have also shown that some systems deviate from the theory[45]. Transition state theory of liquid viscosity has been applied to the viscosity of sulfur, with the assumption that similar to that of the mixture of simple liquids, the total viscosity of liquid sulfur is the product of the viscosity of eight-membered sulfur rings and the viscosity of the polymeric sulfur chains, each raised to the power of its own weight fraction in the mixture. The viscosity of the rings and chains are then each expressed by an Eyring equation, with temperature-independent enthalpy and entropy of activation which are empirical fitting parameters, and the latter one also involves the weight-averaged chain length of the sulfur chains[68]. As has been shown by the authors[68], this mechanism did not accurately describe the experimental data, and they suggested that it was because of the assumption of treating liquid sulfur as a simple liquid mixture.

To remove the empiricism, a fundamental understanding of the viscosity of liquid sulfur needs to be established. Transition zone theory for viscous relaxation, TZT_{rlx}[35], describes liquid relaxation and viscosity on the fundamental level and has been shown to accurately describe the experimental viscosity data of over 70 systems ranging from inorganic network liquids such as SiO_2, to molecular systems such as methanol and ortho-terphenyl, to liquid metals such as gallium, and it affords detailed mechanistic understanding of the viscous relaxation of liquid. Therefore, it is a great test case to apply TZT_{rlx} to the viscosity of sulfur for mechanistic study of the dynamics of the liquid.

2.4.2. Application of TZT_{rlx} to liquid sulfur

Similar to the analysis in section 2.1 of this chapter, the entropic probability to rearrange into a specific TZ configuration is directly proportional to the ratio of the number of microstates of the TZ compared to that of the reactant phase, expressed in Equation (2.39)

$$\exp\left(\frac{\Delta S^{\ddagger}_{rlx}}{R}\right) = \frac{W^{\ddagger}_{rlx}}{W_{non-erg\ l}} \tag{2.39}$$

where $\Delta S_{rlx}^{\ddagger}$ is the entropy of activation for relaxation, $W_{rlx}^{\ddagger}$ and $W_{non\text{-}erg\ l}$ are the number of microstates of the transition zone and the non-ergodic liquid, respectively.

When a liquid is quenched to the Kauzmann temperature[36], T_K, it becomes non-ergodic with the same larger number and probability distribution of accessible configurations as the original high temperature liquid, while relaxation at T_K requires that the atomic/molecular reorganization of the entire system becomes cooperative to reach the Kauzmann condition, thus at T_K $W_{rlx}^{\ddagger} \approx 1$ and $W_{rlx}^{\ddagger}/W_{non\text{-}erg\ l} \rightarrow 0$, and $\Delta S_{rlx}^{\ddagger}$ becomes large and negative. At temperatures higher than T_K, both the non-ergodic liquid and the relaxed ergodic liquid can access an increasing number of configurations, such that $W_{rlx}^{\ddagger}/W_{non\text{-}erg\ l}$ increases, and when the temperature reaches the critical temperature, T_c, the liquid becomes indistinguishable with a gas, and non-ergodic and ergodic liquids are indistinguishable and both indistinguishable with the supercritical fluid, thus $W_{rlx}^{\ddagger}/W_{non\text{-}erg\ l} \approx 1$ and $\Delta S_{rlx}^{\ddagger} = 0$.

For liquid sulfur, however, when the liquid undergoes a sudden temperature change to the polymerization temperature, T_p, or alternatively is exposed to a shearing force at T_p, it becomes non-ergodic and must relax to adapt its energy and configurations to accommodate the new probability distribution of configurations. Since liquid sulfur undergoes a significant amount of structural change at T_p, this relaxation process likely requires a significant amount of atomic/molecular rearrangements. Furthermore, since the 8-membered sulfur rings and long sulfur chains likely coexist and are interchanging in the relaxed liquid at T_p, only one or very few configurations are available that can accommodate such a probability distribution of configurations in the relaxed liquid, and thus $W_{rlx}^{\ddagger} \approx 1$ or very small, while $W_{non\text{-}erg\ l}$ remains

the same larger number as for the liquid at a different temperature or before shearing. Therefore, $W_{rlx}^{\ddagger}/W_{non\text{-}erg\ l} \rightarrow 0$, and $\Delta S_{rlx}^{\ddagger}$ becomes large and negative.

The above discussion suggests that for liquid sulfur, $\Delta S_{rlx}^{\ddagger}$ becomes large and negative at both T_K and T_p. Such a temperature response to the entropy of activation can be modeled by Equation (2.40), where, similar to $\Delta S_{rlx}^{\ddagger}$ of other liquids discussed in Section 2.1, ΔS_{rlx}^{*} and z_{rlx} are material specific parameters that scale the magnitude of $\Delta S_{rlx}^{\ddagger}$ and modulate the temperature/pressure dependence, respectively, while the square root on the denominator makes the part raised to the power of z_{rlx} unitless, and the absolute value indicates that it is the difference between the relaxation temperature and T_p that affects $\Delta S_{rlx}^{\ddagger}$, which accounts for liquid sulfur both below and above T_p.

$$\Delta S_{rlx}^{\ddagger} = \Delta S_{rlx}^{*}\left(\frac{T_c - T}{\sqrt{(T - T_K)|T - T_P|}}\right)^{z_{rlx}} \tag{2.40}$$

The above discussion and Equation (2.40) both suggest a discontinuity in $\Delta S_{rlx}^{\ddagger}$ at T_p, although such discontinuity should only exist if the polymerization in sulfur is exactly a first-order phase transition. Indeed, $W_{rlx}^{\ddagger} = 1$ at T_p is only valid when polymerization is a first order phase transition, and the broader and more second-order the transition is, the more configurations are accessible to accommodate the two coexisting phases, and the larger $W_{rlx}^{\ddagger}$ will be. However, since the structure of liquid sulfur differs significantly below and above T_p, it is likely that the atomic/molecular rearrangements are also significantly different below and above T_p, with the relaxation of liquid sulfur below T_p mostly consists of reorganization of 8-membered sulfur rings, while that above T_p mostly consists of formation/breaking/rearrangement of long sulfur chains. Therefore, for the purpose of studying liquid relaxation, an assumption has been made as a first approximation to treat liquid sulfur

below and above T_p as two different liquids, namely, l_r (below T_p) and l_c (above T_p), which likely exhibit different activation parameters for relaxation.

As discussed in Section 2.1, $\Delta H_{rlx}^{\ddagger}$ is dominated by the energy required for making or breaking bonding or intermolecular interactions in the activation process of relaxation. Since different types of bonding or intermolecular interactions are made or broken in relaxation of l_r and l_c, they likely exhibit $\Delta H_{rlx}^{\ddagger}$ of significantly different magnitudes. When the temperature of l_r approaches T_K, the loss of configurational microstates requires an increased size of the cooperative region for each activation event. If l_r could be supercooled to T_K, the entire system would need to transform as a single cooperative region during relaxation, and the energy (enthalpy) required makes it essentially an impossible condition. Therefore, $\Delta H_{rlx}^{\ddagger}$ for l_r can be modeled by Equation (2.41).

$$\Delta H_{rlx,l_r}^{\ddagger} = \Delta H_{c,l_r}^{*}\left(\frac{T}{T-T_K}\right) \tag{2.41}$$

By contrast, when l_c is quenched, at first, sulfur chains of increased lengths are formed during relaxation by aggregation of the shorter sulfur chains from l_c close to T_c, yet when the temperature of l_c approaches T_p, 8-membered sulfur rings are more likely to be formed from sulfur chains during relaxation, and if l_c could be quenched to T_p, the relaxation process would require the entire system to transform from sulfur chains into 8-membered sulfur rings, resulting in $\Delta H_{rlx}^{\ddagger}$ being large in magnitude and essentially an impossible condition due to the amount of rearrangements required. Under the assumption that liquid sulfur below and above T_p are treated separately as two different liquids, relaxation of l_c below T_p is undefined. Therefore, $\Delta H_{rlx}^{\ddagger}$ for l_c is proportional to the amount of bond

reorganized either by forming longer sulfur chains or by forming 8-membered sulfur rings, which reaches its maximum at T_p and can be modeled by Equation (2.42).

$$\Delta H^{\ddagger}_{rlx,\mathrm{l_c}} = \Delta H^{*}_{c,\mathrm{l_c}} \left(\frac{T}{T - T_p} \right) \tag{2.42}$$

Unlike most liquids where the only structural change with temperature is thermal expansion, the structure of liquid sulfur changes significantly with temperature, thus temperature dependent density and speed of sound should be used in the pre-factor of TZT_{rlx} for the entire temperature range. Density and speed of sound for both liquids at different temperatures were taken from literature[64,69], and linear relationships with temperature were fitted to account for the temperature dependence of each of them, which are then used in the TZT fit to the experimental values of viscosity.

With the above discussion, TZT_{rlx} were fit to viscosity data of sulfur which were taken and digitized from published results by Bacon and Fanelli[63] and by Ruiz-Garcia, Anderson and Greer[66], as shown in Figure 2.8a. The fitting parameters are listed in Table 2.1.

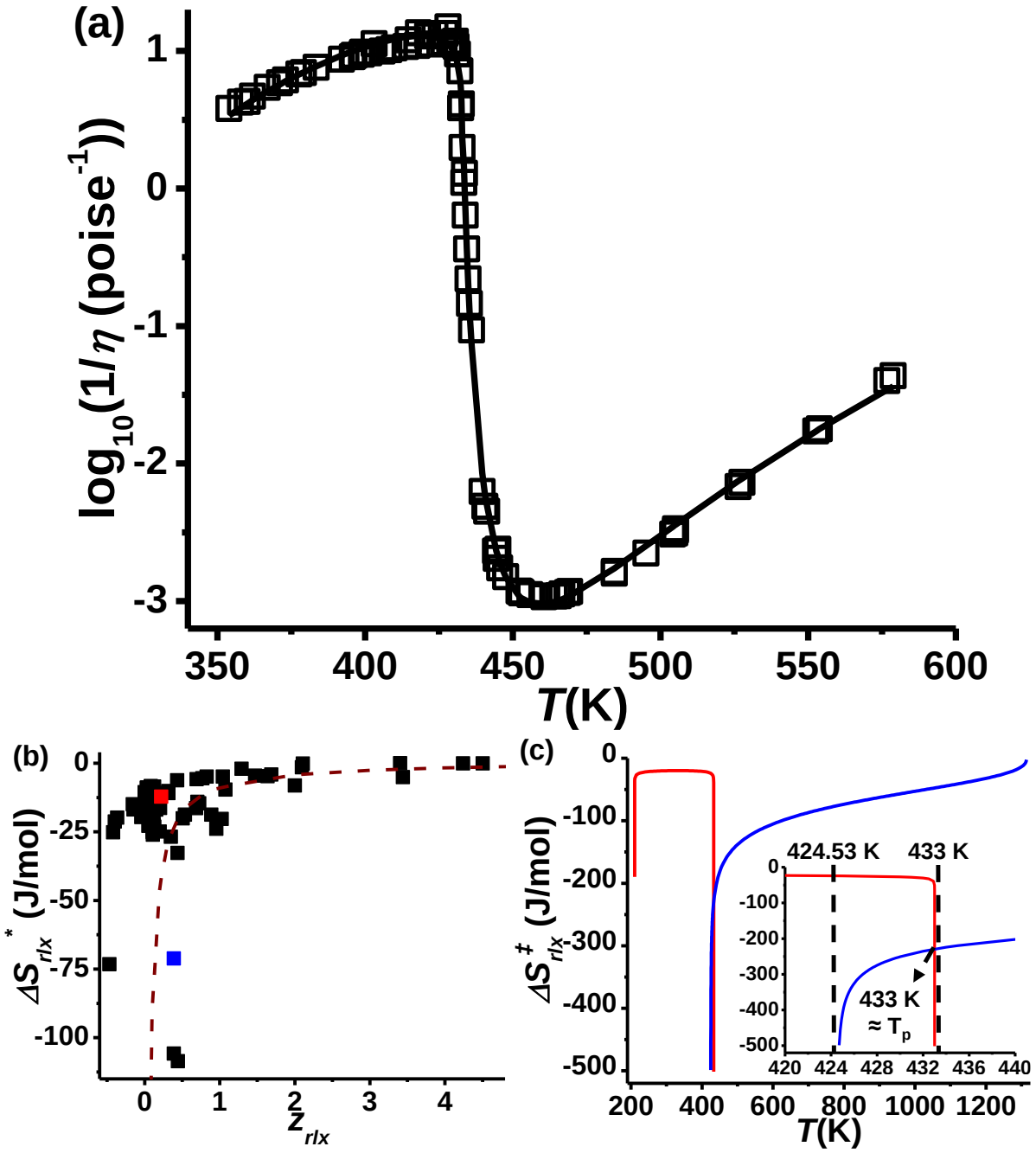

Figure 2.8. (a) Viscosity of sulfur (open squares) and TZT_{rlx} fit (solid curve). (b) Replot of Figure 2.3d, with ΔS_{rlx}^{*} and z_{rlx} for low (red) and high (blue) temperature liquid sulfur added, and all the ΔS_{rlx}^{*} and z_{rlx} for other materials plotted as black squares to highlight ΔS_{rlx}^{*} and z_{rlx} for liquid sulfur. (c) $\Delta S_{rlx}^{\ddagger}$ of sulfur over the entire temperature range where viscosity data are available. The insert is an enlarged 420 – 440 K portion of the plot. The lower limit of $\Delta S_{rlx}^{\ddagger}$ for liquid sulfur above T_p, the higher limit of the $\Delta S_{rlx}^{\ddagger}$ for liquid sulfur below T_p, and the cross point of the above two curves of $\Delta S_{rlx}^{\ddagger}$ are marked in the figure.

Table 2.1. Fitting parameters of TZT_{rlx} for viscosity of sulfur. T_K and T_c were taken from literature, while T_p for l_r and l_c were fitted to temperatures ~1 K above and ~10 K below the literature reported T_p, respectively. The linear functions of T for density and velocity of sound were fitted to data taken from each of their citations. The number in parentheses after the parameters of each linear fit as well as after values of ΔH_{rlx}^*, ΔS_{rlx}^* and z_{rlx} are each of their standard errors.

	l_r	l_c
T_p (K)	433	424.53
T_c (K)	1314.15[70]	1314.15[70]
T_K (K)	210.15[71]	210.15[71]
ρ (kg•m^{-3})[69]	-0.92(3)T+2.162(11)×10^3 R^2 = 0.9104	-0.69(4)T+2.07(2)×10^3 R^2 = 0.8340
v_s (m•s^{-1})[64]	-1.878(15)T+2.100(6) ×10^3 R^2 = 0.9983	-0.98(3)T+1.72(2) ×10^3 R^2 = 0.9902
ΔH_{rlx}^* (kJ•mol^{-1})	5.0(3)	-1.43(2)
ΔS_{rlx}^* (J•mol^{-1}•K^{-1})	-12(1)	-71.2(7)
z_{rlx}	0.22(2)	0.389(6)

A few interesting mechanistic insights is revealed from the TZT_{rlx} fit. Since l_r and l_c have significantly different structures and thus likely different temperature dependence in entropy, they likely also exhibit different values of T_K. The reported value of T_K for sulfur, 210.15 K, used in this work was measured by supercooling liquid sulfur from 175 °C[71], which is close to but above the polymerization temperature, thus T_K = 210.15 K is most likely close to T_K for l_c, although should not be too different from T_K for l_r. Without experimental data available, T_K for l_r is unknown, and thus the same T_K was used for both l_r and l_c as a first approximation. As shown in Figure 2.8b, ΔS_{rlx}^* and z_{rlx} for both l_r and l_c follow the correlation line, with the deviation likely due to the pressure-dependence of the liquid structure. ΔH_{rlx}^* is positive for l_r and negative for l_c. The positive ΔH_{rlx}^* of l_r is consistent with the breaking of bonding and intermolecular interactions to reorganize 8-membered sulfur rings in liquid sulfur below T_p. The negative ΔH_{rlx}^* of l_c indicates that relaxation is dominated by formation of bonding interactions to form long sulfur chains. The temperatures at which viscosity of the

high temperature liquid sulfur was measured are close to T_p, at which it has been experimentally observed that liquid sulfur mainly consists of chains and the chain length increases as temperature increases[64], thus a negative ΔH_{rlx}^* is consistent with the experimental observation, and it is anticipated that a positive ΔH_{rlx}^* may be required for viscous relaxation of liquid sulfur at higher temperatures, especially close to T_c.

As shown in Figure 2.8c, $\Delta S_{rlx}^{\ddagger}$ of l_r and l_c cross at ~432.99 K, close to the reported polymerization temperature of 432.15 K. Additionally, the fitted T_p for l_c is slightly lower than the reported T_p, which leads to the difference between the lower limit of $\Delta S_{rlx}^{\ddagger}$ of l_c and the higher limit of $\Delta S_{rlx}^{\ddagger}$ of l_r being 8.47 K, consistent with the calorimetric experimental observation that polymerization of liquid sulfur starts approximately 10 K below the polymerization temperature[65]. Therefore, even though viscosity data of sulfur were fit by treating liquid sulfur below and above T_p as two different liquids under the assumption that polymerization of sulfur is a first-order phase transition, this 8.47 K difference in temperature likely indicates that the polymerization transition of liquid sulfur contains components of a second-order phase transition. The observation that the viscosity data were still accurately described by TZT_{rlx} likely suggests that an assumption of a first-order phase transition for polymerization of sulfur does not significantly impact TZT_{rlx} fit, which may be due to the polymerization transition being in between first and second order. We further anticipate that for liquids that undergo an exactly first order liquid-liquid phase transition, the temperature difference between the lower and higher limits of $\Delta S_{rlx}^{\ddagger}$ of the two phases should be zero, which leads to a sharp discontinuity in $\Delta S_{rlx}^{\ddagger}$ at exactly the transition temperature; while for liquids that undergo a second order liquid-liquid phase transition, the temperature difference between the lower and higher limits of $\Delta S_{rlx}^{\ddagger}$ of the two phases becomes non-zero due to the lack of

discontinuity in second order phase transition, and the temperature difference increases as the phase transition becomes more gradual and spanning over a larger temperature region; for liquids that only undergo slight or very gradual structural change with temperature, such as the decrease in density as the temperature increases, this temperature difference becomes smoothed out which leads to one continuous $\Delta S_{rlx}^{\ddagger}$ for relaxation of the liquid over the entire temperature region, which is the case for relaxation of most liquids studied in Section 2.1. Those anticipations suggest Equation (2.40), instead of Equation (2.10), should be used for TZT_{rlx} to describe $\Delta S_{rlx}^{\ddagger}$ for liquids that undergo significant structural change with temperature, although further experimental studies are necessary to validate such anticipations.

2.4.3. Conclusion

The viscosity of liquid sulfur undergoes significant change with temperature which is different from the temperature dependence of viscosity for most liquids, due to the structural change in liquid sulfur from 8-membered sulfur rings to long sulfur chains by polymerization, the viscosity of the latter being over four orders of magnitude higher than that of the former. Under the assumption of treating liquid sulfur below and above the polymerization temperature as two different liquids, and with a modified entropy of activation which reaches infinity at both the Kauzmann temperature and the polymerization temperature, transition zone theory accurately describes the experimentally measured viscosity of sulfur below, within and above the polymerization temperature region, and it provides mechanistic understanding into the structural reorganization occurring with temperature in liquid sulfur, with the entropy of activation of relaxation likely indicating the polymerization of liquid sulfur being between first- and second-order transition.

As demonstrated above, with TZT_{rlx}, the relaxation process of liquid sulfur which undergoes polymerization with temperature can be understood from a molecular level. That indicates the potential of applying TZT_{rlx} to investigate liquid-liquid phase transition, as well as the relaxation process and viscosity of other liquids that undergo significant structural change with temperature, such as the liquid monomers during their polymerization processes, which can be applied commonly in polymer industry.

CHAPTER 3

Determination of the Phase-Boundary Velocity of Individual Crystallites in Polycrystalline Growth

3.1. Introduction

The mechanism(s) by which homogeneous liquids and amorphous systems crystallize has been studied in diverse areas of science and technology. The rate of crystallization has been observed to increase with temperature (Arrhenius-like) above the glass transition temperature, T_g, up to some maximum temperature, T_{max}, above which anti-Arrhenius behavior is observed, decreasing to zero at the melting temperature, T_m[5]. For some crystalline materials, due to the high crystallization rates especially at temperatures around T_{max}, extremely small samples or extremely fast cooling rates are required (e.g. 20 ng and 70000 K/s for poly(ε-caprolactone)[72]) to measure crystallization rates at deep supercooling of the melt without crystallization occurring during the cooling process. Therefore, when such small sample sizes or fast cooling rates are not feasible, to measure the crystallization rates over the entire temperature range for mechanistic study, two strategies are mostly used: melt crystallization, where the sample is supercooled directly from its melt to the crystallization isotherm, which is commonly used to measure the rate of crystallization in the anti-Arrhenius temperature region (shallow supercooling); cold crystallization, where the sample is quenched from its melt to the glassy state and heated back up to the crystallization isotherm, which is commonly used to measure the rate of crystallization in the Arrhenius-like temperature region (deep supercooling). It has been observed for numerous materials, such as poly(L-lactic acid)[73-75],

isotactic polystyrene[76], isotactic polybutene[77] and syndiotactic polypropylene[78], that cold crystallization appears to be faster than melt crystallization at identical crystallization isotherms. This phenomenon has been attributed to the additional nuclei in cold crystallization, the formation of which is explained as either the homogeneous nucleation near the glass transition temperature[72,76,79], or the nucleation during the cooling of the melt to the glass[73,75], such that cold crystallization initiates with more nuclei ("initial nuclei") which grow simultaneously into multiple crystallites, and consequently, the time it takes to fully crystallize the same sample is shorter, and the bulk crystal growth rate appear to be faster. Furthermore, it has been observed that additional nuclei are formed in cold crystallization for samples that are aged below the cold crystallization temperature[73,77,79], which exhibits even faster cold crystallization. To study the mechanism of crystallization with both melt and cold crystallization, and further to investigate the mechanisms of both single- and poly-crystalline growth, the impact from initial nuclei needs to be removed to yield material-specific kinetics of crystal growth.

Kinetic parameters of isothermal crystallization from supercooled melts or superheated glasses are often extracted by the Kolmogorov[37]-Johnson and Mehl[38]-Avrami[39-41] (KJMA) model, in which the fraction of the material crystallized, α, is commonly expressed as

$$\alpha(t) = 1 - \exp\left\{-\left[k\left(t - t_0\right)\right]^n\right\} \tag{3.1}$$

with rate constant k, nucleation time t_0 and dimensionality n. It has been demonstrated that these kinetic parameters are strongly dependent on experimental factors[80-82] and do not necessarily reflect the true reaction mechanism[83-85]. Since crystallization is a phase-boundary controlled process (i.e. the phase boundary between the melt and the crystal proceeding in the

melt by atomic rearrangements at the phase boundary to form the crystal), the velocity of the phase boundary, v_{pb}, should be a material-specific value, albeit temperature dependent. With the crystallization process normalized as the fraction of the material crystallized in the KJMA model, the sample volume and geometry information is removed from the experimental signal and placed onto the kinetic parameters, which results in sample volume and geometry dependent k and n. To obtain the material-specific kinetics of crystal growth, i.e., the velocity of the phase boundary, v_{pb}, for mechanistic study, we have previously reintroduced the sample volume and geometry into the KJMA model which yields the modified KJMA model, expressed as

$$v_{pb} = \frac{kg\sqrt[3]{V}}{a_c}$$
$$\alpha(t) = 1 - \exp\left\{-\left[\frac{v_{pb}a_c}{g\sqrt[3]{V}}(t - t_0)\right]^{n'}\right\} \tag{3.2}$$

with sample geometry a_c (aspect ratio), crystal growth geometry g, sample volume V, and apparent bulk dimensionality n'[13,42].

With an increased number of crystallites, the sample is divided into smaller domains growing simultaneously, such that a shorter time is taken to fully crystallize the sample, and the material-specific v_{pb} should be the velocity of the phase boundary between each crystallite and the melt. Therefore, based on the previously demonstrated sample size impact on the KJMA rate constant[13,42], it has become clear that the more nuclei in a sample, the smaller each crystallite, and thus a sample size correction with the total volume of the sample will likely lead to an over-estimation of the rate constant for polycrystalline growth.

In this chapter, investigations into the melt and cold crystallization of the halozeotype CZX-1, $[HN(CH_3)_3]CuZn_5Cl_{12}$[43], is described. CZX-1 crystallizes in the cubic space group $I\bar{4}3m$ with a = 10.5887(3) Å, congruently melts at a moderate melting point of 173 °C and forms a glass near room temperature (around 30 °C), which simplifies melt and cold crystallization studies. For kinetics of polycrystalline growth measured with 2-D temperature- and time- resolved synchrotron X-ray diffraction (TtXRD), v_{pb}'s of each crystallite are directly estimated with our in-group developed program, Ramdog. Furthermore, the relationship between the number of initial nuclei and the time taken to heat each sample from glassy state to crystallization isotherm is evaluated and applied to estimate the v_{pb}'s of each crystallite of polycrystalline growth measured by differential scanning calorimetry (DSC). With the v_{pb}'s of each crystallite, the impact of initial nuclei on crystallization kinetics are removed, and thus material-specific crystallization kinetics are obtained for investigation of the mechanism of melt and cold crystallization.

3.2. Methods

3.2.1. Material Preparation

All manipulations were performed under an inert N_2 atmosphere in a glovebox or using vacuum lines. $ZnCl_2$ was purchased from Aldrich and purified via triple sublimation at 350 °C prior to use. $HN(CH_3)_3Cl$ was purchased from Aldrich and purified via double sublimation at 130 °C prior to use. CZX-1[18] and CuCl[86] were prepared according to previously reported procedures. The purity of all starting materials and CZX-1 was confirmed by powder X-ray diffraction (XRD, INEL CPS-120) and DSC (TA Instruments Q2000).

3.2.2. Isothermal Melt and Cold Crystallization: DSC

All samples were sealed in high-pressure stainless steel DSC pans with gold foil seals (PerkinElmer product No. B0182901). Prior to all crystallization measurements, each sample was melt-crystal cycled on the DSC five times between 40 and 230°C at a constant rate of 5°C/min before isothermal crystallization experiments were performed to remove heterogeneous nucleation sites and to ensure uniform thermal contact between the pan and the sample. Isothermal melt crystallization was performed at isotherms between 145°C and 162°C using the same methods as reported previously[13]. For isothermal cold crystallization, the sample was heated to 230°C on a hot plate, held for 5 – 10 minutes to ensure melt isotropy, then quickly dumped into liquid nitrogen to quench to its glassy state, and transferred back into the DSC and heated back up at the maximum instrumental heating rate of ~100°C/min to the crystallization isotherm (55 – 95°C). When heated above 95°C, the sample started to crystallize before the isotherm was reached, and the crystallization heat flow could not be separated from the instrumental response.

For each sample, the instrumental response, which must be subtracted from the raw signal to obtain the crystallization heat flow, was obtained by repeating the same process on the DSC in each cold crystallization experiment right after crystallization was complete without taking the sample out of the DSC.

3.2.3. Isothermal Melt and Cold Crystallization: 2-D TtXRD

Synchrotron diffraction data for melt crystallization were obtained as reported previously[13], with a few additional data points obtained on beamline 11-ID-B (60 KeV, λ = 0.2114 Å, collimated beam 0.5 × 0.5 mm) at the Advanced Phonon Source (APS), Argonne

National Laboratory using the same experimental procedure, except with a new quenching furnace with two pneumatically switchable metal pipes, one of which has constant air flow at the high-temperature melt isotherm (230 °C) to melt the sample and the other has constant air flow at the crystallization isotherm, instead of a pneumatically switchable manifold that directs airflow through one of two ¾'' in-line air heaters on the previously used quenching furnace. The sample was placed in the air flow above one of the pipes. The instruments for the temperature control of the air flow at each pipe was the same as the old quenching furnace, described previously[13], and the phase transitions of elemental sulfur and the melting temperature of CZX-1 were used as calibrants for the temperature at the sample. With the new furnace, once the pipes were switched, the sample was immediately exposed to the air flow at the desired crystallization isotherm, which affords rapid quenching to the crystallization isotherm within 1s, instead of ~15s with the old quenching furnace, irrespective of the melt and quench temperatures.

Synchrotron diffraction data for isothermal cold crystallization were obtained on beamline 11-ID-B (60 KeV, $\lambda = 0.2114$ Å, collimated beam 0.5 × 0.5 mm) at the Advanced Phonon Source (APS), Argonne National Laboratory with the new quenching furnace. Data were collected in a Debye-Scherrer geometry at a sampling rate of 1Hz, with each diffractogram hereafter referred to as a frame. Samples were sealed into fused silica capillaries (Charles Supper Co., Natrick, MA) of 0.7 mm diameter, melt-crystal cycled between 40 and 230°C, and affixed to a single-axis goniometer head with epoxy. During crystallization experiments, the samples were oscillated 1.2° per frame in synchronization with the duration of X-ray beam exposure to illuminate a larger region of the sample. After each crystallization experiment was complete, a final image was taken with the sample oscillating 18° while being

exposed in the X-ray beam for 15 seconds. The wavelength and detector alignment were calibrated to CeO_2 standard using fit2D to correct all experimental data.

Cold crystallization on TtXRD was performed both with instant heating and different programmed heating rates to the isotherm. Each melted-recrystallized sample ingot in a fused silica capillary was centered in the synchrotron beam. The sample was melted in the high-temperature air flow and held at 230°C for at least 5 minutes to ensure melt isotropy, then the high-temperature air flow was switched away and the sample was immediately quenched to a glass with a freeze spray. Data collection was initiated for at least 15 frames prior to heating to the isotherm. For cold crystallization with instant heating, the pipe with the air flow held at the crystallization isotherm (55 – 155°C) was switched below the glassy sample to heat the sample instantly, and for cold crystallization with programmed heating, the pipe with the air flow held initially at 30 °C was switched below the glassy sample, and the air flow was heated at a certain programmed heating rate (between 30 and 100°C/min) on the heat control device to the isotherm (80, 90, 100°C). Diffraction data was recorded until crystallization was complete.

3.2.4. The In-group Developed Software to Analyze the Growth Rate of Individual Crystallites

The growth rate of each crystallite in a polycrystalline growth measured with 2-D TtXRD was analyzed by the in – group developed software "Ramdog"[87]. In a 2-D TtXRD experiment, frames, or 2-D X-ray images are taken at a certain frequency (e.g. 1 frame/second) throughout the crystal growth process, such that there are a series of 2-D X-ray images corresponding to each 2-D TtXRD experiment, with each image showing the 2-D X-ray

diffraction of the sample at the time point it is taken. In a 2-D X-ray image, each ring corresponds to a diffraction angle from the Bragg's law, and each crystallite in the sample corresponds to an active diffraction spot on each ring. Therefore, if the same active spots are selected from serial 2-D X-ray images of one TtXRD experimental time series, and the intensity of each spot is monitored throughout the whole series, the change in intensity of each spot with experimental time should indicate the growth of each corresponding crystallite in the sample.

Java development kit or Java runtime environment is required to run Ramdog. To open a 2-D X-ray image (either the raw TtXRD frames or TtXRD frames converted to binary file format if the raw format is in .tiff) in Ramdog, the image dimensions (normally: 512×512, 1024×1024, 2048×2048, etc.), the starting byte of the image and the data type are required and can be determined by: image dimensions × data type + starting byte of the image = the file size of the image. Once the image is opened, the color scale is adjusted by changing the intensity of the color levels (normally white and black) to give the robust contrast of the image. The calibration information at the top left corner of the Ramdog interface is required for any data analysis in Ramdog, among which the wavelength of the X-ray used and the pixel size are properties of the 2-D TtXRD instrument, and the center of the 2-D X-ray image and the sample-to-detector distance are obtained by calibration to the CeO2 standard with fit2D[88,89].

Since all active spots on a 2-D X-ray image comprise pixels of high intensity, for every pixel on each 2-D X-ray image, if the 2nd derivatives of its intensity in both the x and the y dimension are negative, then that pixel is around a local maximum of pixel intensity and is likely part of an active diffraction spot. Therefore, after the second derivative of the intensities of each pixel was taken with the Savitsky-Golay method[90], the active diffraction spots are

selected such that each spot contains a certain number of pixels with negative 2nd derivatives of its intensity in both the x and the y dimensions, with the center of the spot having the most negative 2nd derivatives in both dimensions. To better differentiate the signal of a crystallite from the amorphous background, a certain upper-limit value, or "threshold", is set in Ramdog such that only pixels with 2nd derivatives more negative than that will be considered as corresponding to active spots.

For each 2-D TtXRD measurement of crystallization kinetics of CZX-1, spots were selected from the last 2-D X-ray image in the series with the number of pixels per spot between 3 and 5 and threshold between -5 and -50; the exact values varied depending on the size and intensity of spots in each series of frames. The growth of each spot was then analyzed by monitoring the change in intensity of each spot throughout the whole series of frames. The intensity of each spot is then integrated and normalized by Ramdog as a function of time, with the lowest intensity of each spot being zero and the highest being one to obtain the normalized growth curve which represents the fraction crystallized for each spot.

3.3. Results and Discussion

3.3.1. Bulk Growth Rate of Melt and Cold Crystallization

With 2-D TtXRD, it is visible that polycrystalline growth occurs in all cold crystallization experiments, as well as in melt crystallization due to deep supercooling or heterogeneities in the sample[91], as shown in Figure 3.1 a – h, j, l. Single or near-single crystal growth is exhibited in melt crystallization at shallow supercooling at or above T_{max}, as shown in Figure 3.1 i, k. With the new quenching furnace, the crystallization isotherm of melt and cold crystallization can be reached within 1s. By contrast, in the cold crystallization

measurements where the heat controller was programmed to heat the air flow, and thus the sample in it, at a lower heating rate, a longer time was taken to reach the cold crystallization isotherm, which results in even more polycrystalline growth compared to cold crystallization in which the isotherm was reached instantly, as shown in Figure 3.1 c, d, g, h and a quantitative analysis follows later in this chapter.

Figure 3.1. Final 2-D X-ray images of melt and cold crystallization at various isotherms, with the crystallization isotherm and quenching/heating methods to reach the isotherm marked above each final image. The histograms from analysis of individual crystallite growth are placed at the bottom right corner of each of their corresponding 2-D X-ray image, with the x-axis being the v_{pb}'s of individual crystallite growth and the y-axis being the frequency.

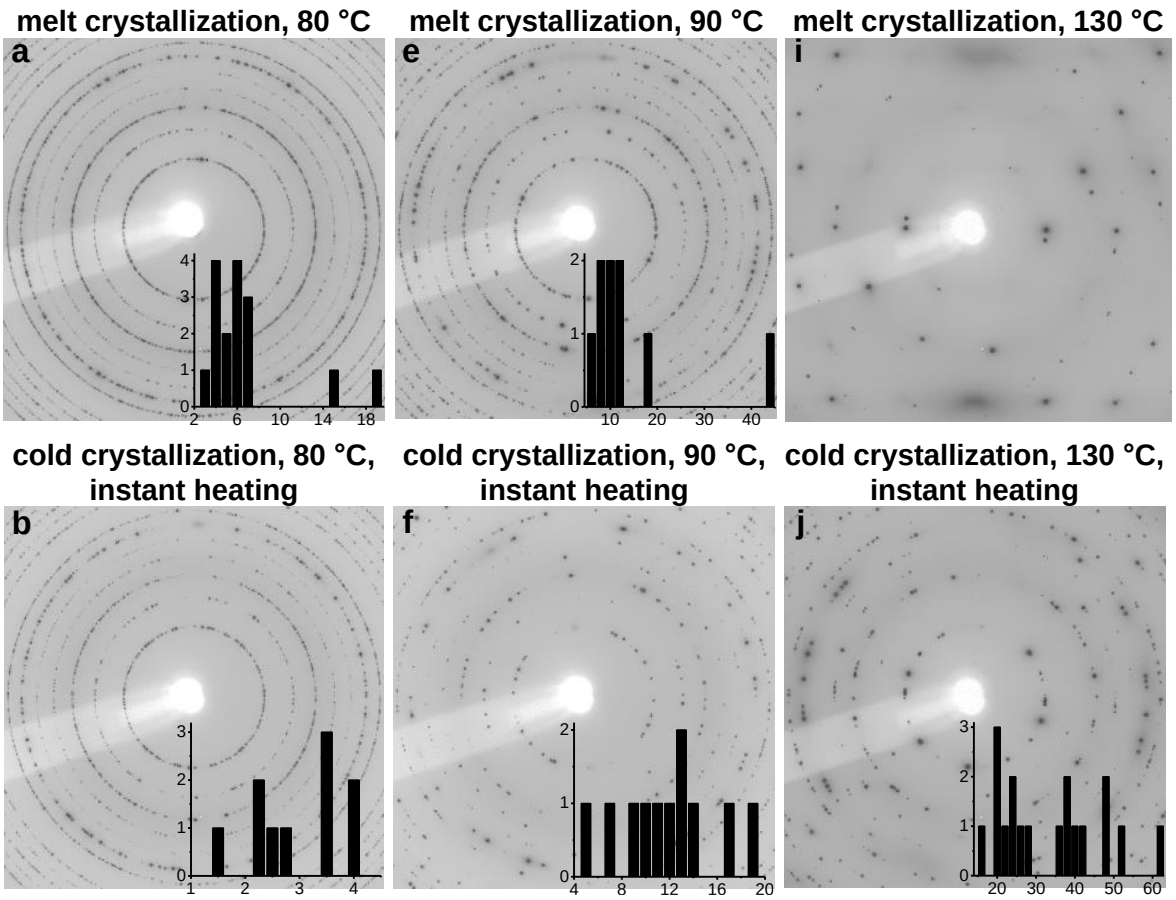
melt crystallization, 80 °C
melt crystallization, 90 °C
melt crystallization, 130 °C
a
e
i
cold crystallization, 80 °C, instant heating
cold crystallization, 90 °C, instant heating
cold crystallization, 130 °C, instant heating
b
f
j

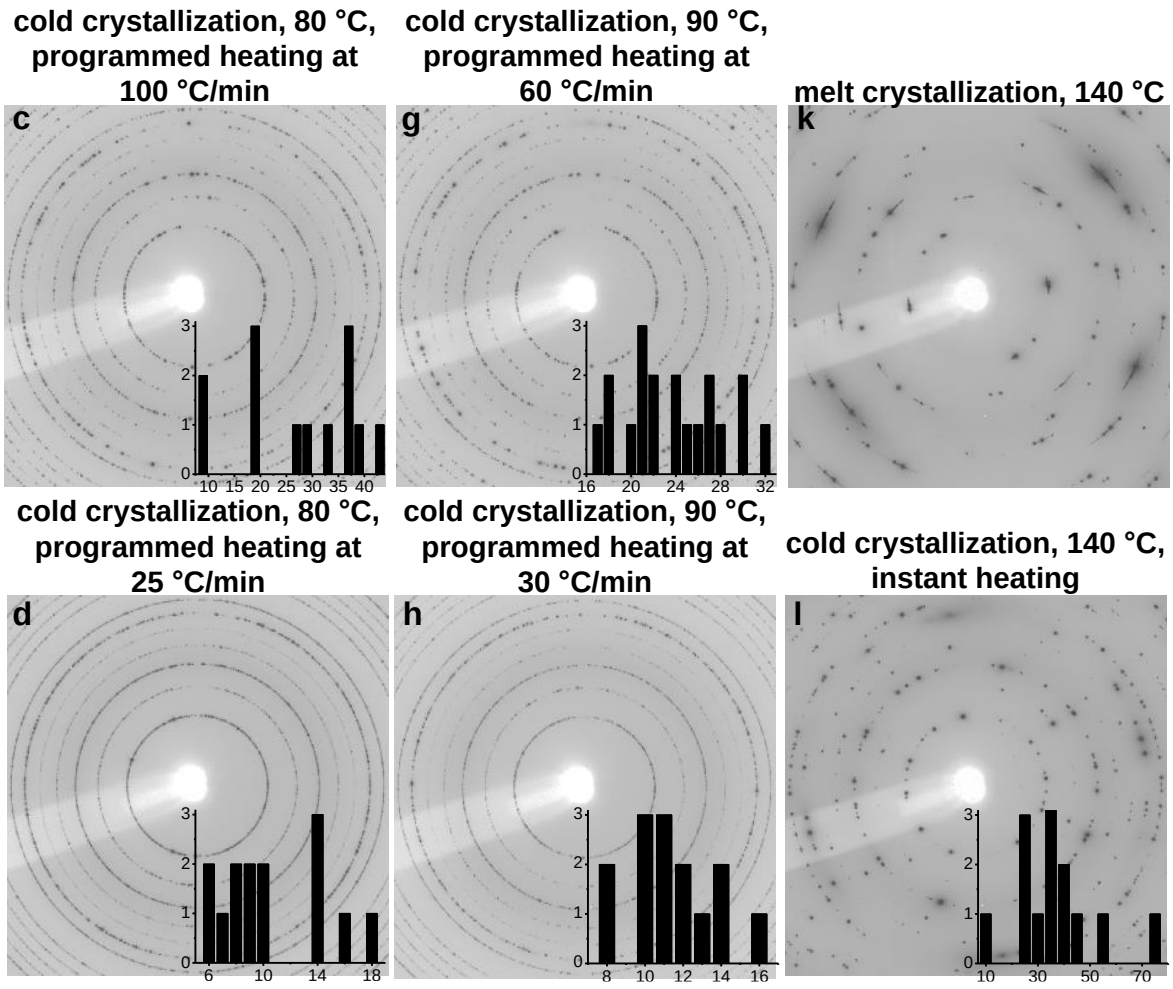
cold crystallization, 80 °C, programmed heating at 100 °C/min
cold crystallization, 90 °C, programmed heating at 60 °C/min
melt crystallization, 140 °C
c
g
k
cold crystallization, 80 °C, programmed heating at 25 °C/min
cold crystallization, 90 °C, programmed heating at 30 °C/min
cold crystallization, 140 °C, instant heating
d
h
l

Similar to previous analysis[13], the normalized growth curve from isothermal crystallization experiments on the DSC was obtained by integration of the exothermic crystallization peak with respect to time, while the serial 2-D X-ray frames for each 2-D TtXRD measurement were azimuthally averaged by fit2D to create 1-D X-ray diffraction patterns, which are then analyzed by singular value decomposition to obtain the time-dependence of the peak intensities, and further normalized into the fraction of the sample crystallized with respect to time. All the normalized growth curves were fit to the KJMA model in Equation (3.1) over the range $0 \leq \alpha \leq 0.5$, with k and t_0 as fitting parameters and n fixed with respect to the sample anisotropy[42]. The bulk crystal growth rate, v_{pb_bulk}, was obtained using Equation (3.2) with the total volume of the sample, geometry factor $g = 1$ as for cubic crystal growth of CZX-1, and sample anisotropy factor a_c for melt crystallization on the DSC. No anisotropy factor was necessary ($a_c = 1$) for melt crystallization on the 2-D TtXRD due to the isotropic sample shapes, or for cold crystallization on either the DSC or the 2-D TtXRD because an increased number of crystallites, obtained from an increased number of initial nuclei, divides the anisotropic sample into smaller, isotropic domains[42]. As shown in Figure 3.2, v_{pb_bulk} of cold crystallization appear to be faster than that of melt crystallization, with cold crystallization on the DSC even faster than that on the 2-D TtXRD, and v_{pb_bulk} of melt crystallization at low temperatures also appear to be higher than the general curve of v_{pb} of melt crystallization.

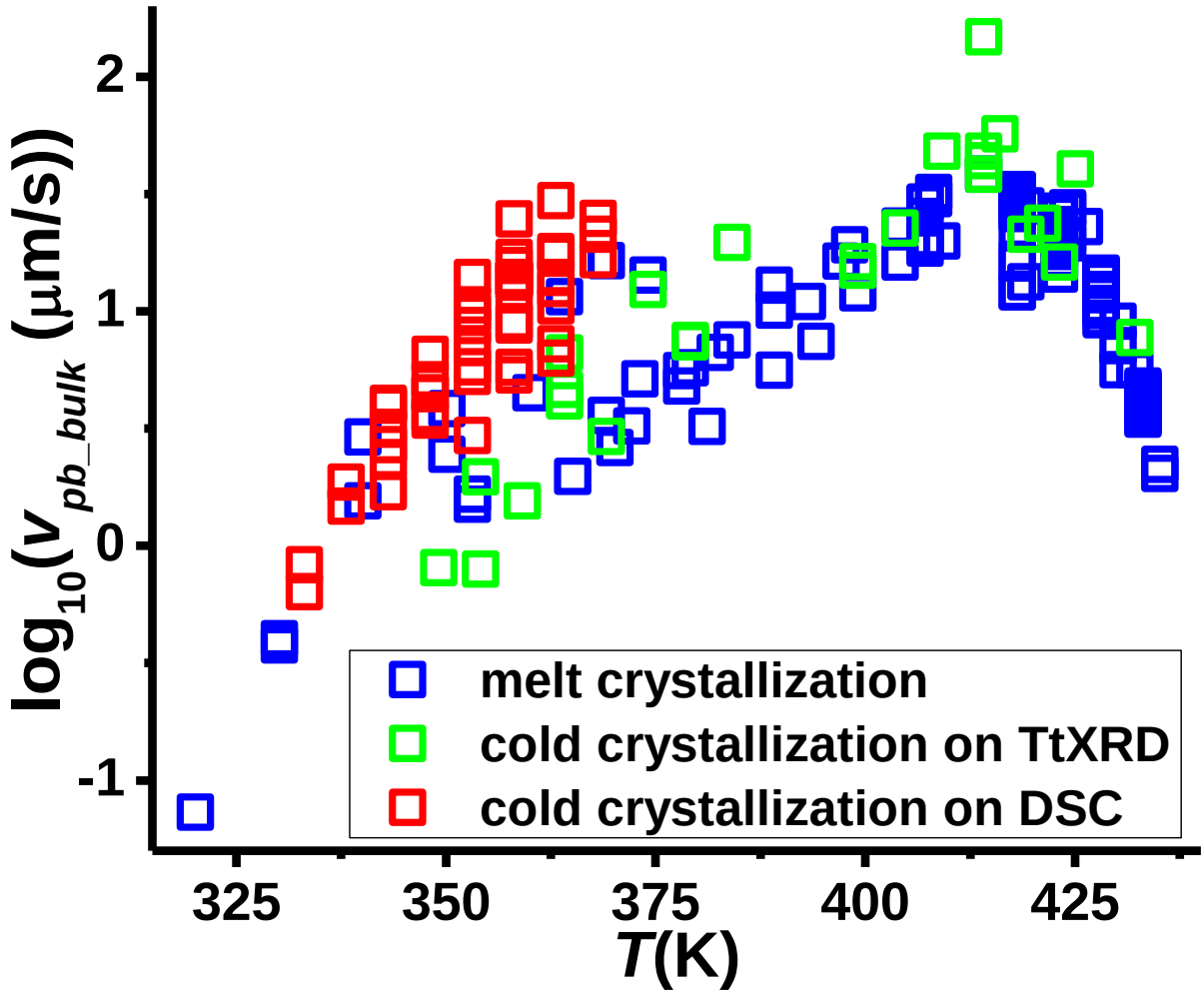

Figure 3.2. v_{pb_bulk} of melt and cold crystallization measured with DSC and 2-D TtXRD.

3.3.2. Growth Rates of Individual Crystallites from Isothermal Crystallization Experiments with 2-D TtXRD

The normalized growth curve of each active spot in each series of 2-D X-ray images from 2-D TtXRD experiments was obtained with Ramdog; a screen shot of the Ramdog interface is shown in Figure 3.3a. The spots on the rings of each 2-D X-ray image with the scattering vector (q) corresponding to the most intense peaks in the 1-D XRD pattern, with the least noisy normalized growth curve and reasonably high final intensity were selected such

that spots that correspond to noise, crystallites that started in the X-ray beam but grew out of the beam, and crystallites that moved in and out of the X-ray beam with the oscillation of the sample were avoided. For each series of 2-D X-ray images of polycrystalline growth, at least 3 rings were selected for analysis, and at least 3 spots were analyzed from each ring. The normalized growth curve of each selected spot was fit to the KJMA model in Equation (3.1) over the range $0 \leq \alpha \leq 0.5$.

As shown in Figure 3.3b, spots with higher final intensity, which as a first approximation correspond to larger crystallites, exhibit lower KJMA rate constants. Previously, we have observed sample-volume dependence of the KJMA rate constant, *k*, such that a larger sample crystallizing exhibits lower *k*. As the crystallization process is normalized as the fraction of the sample crystallized in the KJMA model, the sample volume and geometry information is removed from the experimental signal and placed onto the kinetic parameters, such that a longer time is required to crystallize a larger sample, which results in a lower KJMA rate constant. Here, similar to the sample-volume dependence of *k*, since the growth curve of each crystallite is normalized as the fraction of the crystallite grew in the KJMA model, the crystallite volume information is placed onto the kinetic parameters, such that a longer time is required for a larger crystallite to grow, which results in a lower *k*. Therefore, similar to Equation (3.2), the velocity of the phase boundary for each individual crystallite, $v_{pb\_individual}$, is expressed as

$$v_{pb\_individual} = \frac{kg\sqrt[3]{V_i}}{a_c} \tag{3.3}$$

where V_i is the volume of the crystallite.

Figure 3.3. (a) Ramdog interface. An example of spot-picked 2-D X-ray image, which is the last one in the series of 2-D X-ray images from cold crystallization at the isotherm of 140 °C, is shown with all the picked spots highlighted in green. (b) Normalized growth curves of three spots picked off the ring that corresponds to the (*211*) 1-D X-ray diffraction peak in the serial 2-D X-ray images also from cold crystallization at the isotherm of 140 °C. Each curve corresponds to the growth of one spot, and each spot corresponds to a crystallite of a distinct size indicated by the fraction of the intensity of each spot in the total intensity of the ring. The curves shown through the points in the same colors are the fit of each normalized growth curve with the KJMA model. The fraction of the intensity of each spot in the total intensity of the ring, as well as the corresponding rate constant *k* in the KJMA model, is shown in the figure legend.

a

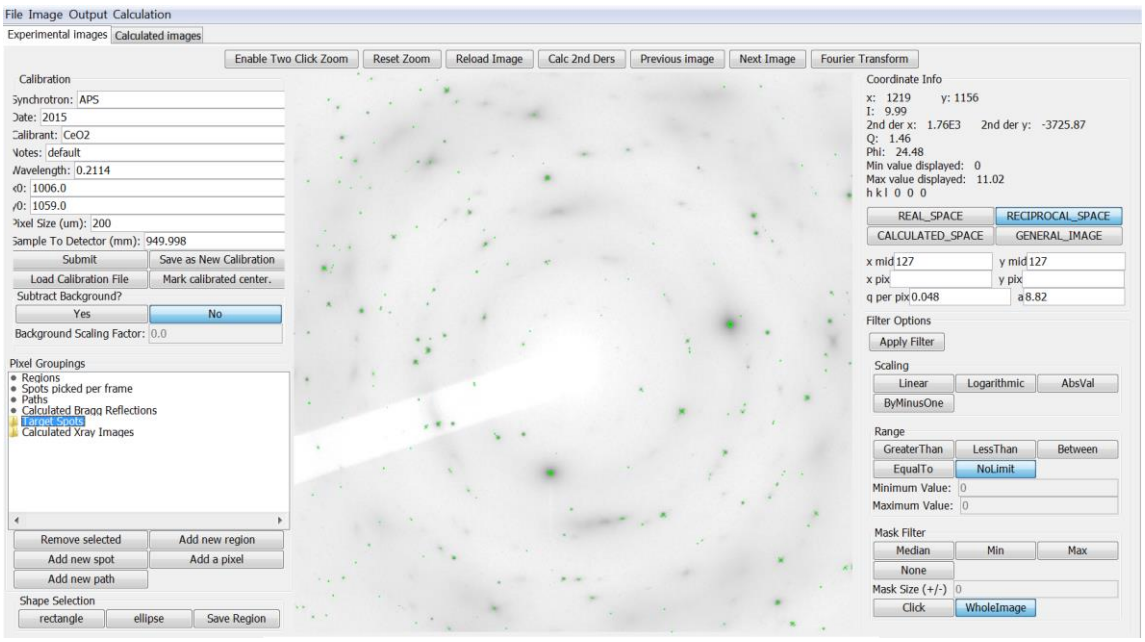
File Image Output Calculation
Experimental images
Calculated images
Enable Two Click Zoom
Reset Zoom
Reload Image
Calc 2nd Ders
Previous image
Next Image
Fourier Transform
Calibration
Synchrotron: APS
Date: 2015
Calibrant: CeO2
Notes: default
Wavelength: 0.2114
x0: 1006.0
y0: 1059.0
Pixel Size (um): 200
Sample To Detector (mm): 949.998
Submit
Save as New Calibration
Load Calibration File
Mark calibrated center.
Subtract Background?
Yes
No
Background Scaling Factor: 0.0
Pixel Groupings
Regions
Spots picked per frame
Paths
Calculated Bragg Reflections
Found Spots
Calculated Xray Images
Remove selected
Add new region
Add new spot
Add a pixel
Add new path
Shape Selection
rectangle
ellipse
Save Region
Coordinate Info
x: 1219 y: 1156
I: 9.99
2nd der x: 1.76E3 2nd der y: -3725.87
Q: 1.46
Phi: 24.48
Min value displayed: 0
Max value displayed: 11.02
h k l 0 0 0
REAL_SPACE
RECIPROCAL_SPACE
CALCULATED_SPACE
GENERAL_IMAGE
x mid 127
y mid 127
x pix
y pix
q per pix 0.048
a 8.82
Filter Options
Apply Filter
Scaling
Linear
Logarithmic
AbsVal
ByMinusOne
Range
GreaterThan
LessThan
Between
EqualTo
NoLimit
Minimum Value: 0
Maximum Value: 0
Mask Filter
Median
Min
Max
None
Mask Size (+/-) 0
Click
WholeImage

b

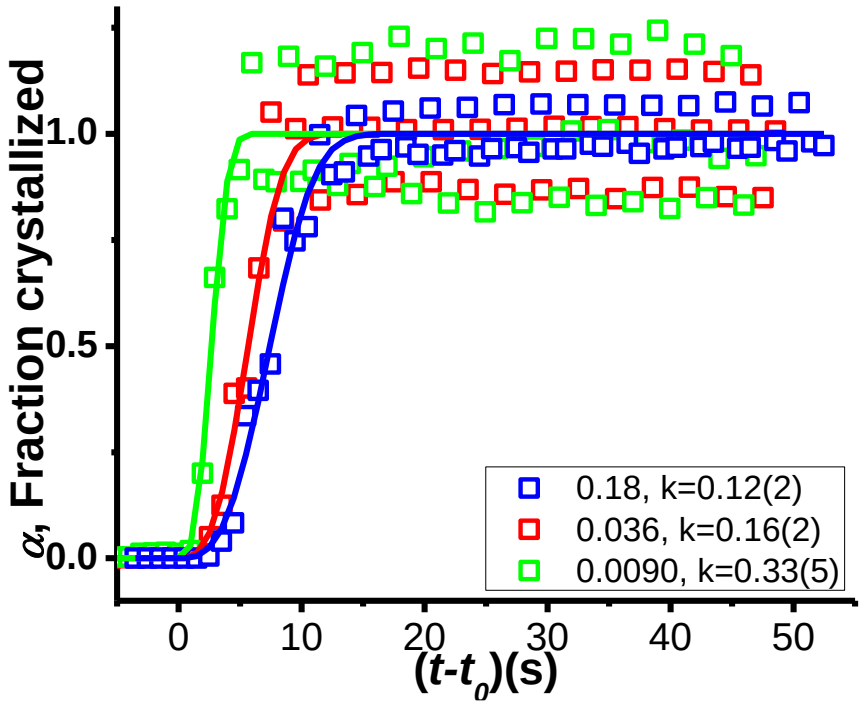
α, Fraction crystallized
1.0
0.5
0.0
0
10
20
30
40
50
(t-t0)(s)
0.18, k=0.12(2)
0.036, k=0.16(2)
0.0090, k=0.33(5)

As discussed earlier in this chapter, for polycrystalline growth of CZX-1, $g = 1$ due to cubic crystal growth, and $a_c = 1$ since the increased amount of crystallites divide the anisotropic sample into smaller, more isotropic domains, such that each individual crystallite has an isotropic geometry. As a first approximation to estimate V_i, the percentage of the volume of each crystallite in the total volume of the sample was estimated as the percentage of the final intensity of the corresponding spot in the total final intensity of the ring it belongs to. Therefore, for each crystallite in each 2-D TtXRD measurement of polycrystalline growth, $v_{pb\_individual}$ was obtained with k extracted from the KJMA fit to the normalized growth curve of the corresponding spot and V_i of the crystallite. For each 2-D TtXRD measurement of polycrystalline growth, a histogram was made with $v_{pb\_individual}$'s of all the spots selected and analyzed by Ramdog to further rule out the occasional outliers that may have abnormally high (dead pixels or crystallites that grew at the edge of the X-ray beam) or low (crystallites of highly anisotropic geometries) values of $v_{pb\_individual}$. A few examples are shown in Figure 3.1. The selected $v_{pb\_individual}$'s by the histograms normally span over a factor of 2, which is within the normally observed error caused by crystallites grow at different places in the sample[13,42], and an abnormally broad histogram or $v_{pb\_individual}$'s, such as the ones in Figure 3.1 c, d, g and h likely indicates the temperature is unstable during the crystallization process such that crystallites grow non-isothermally during the experiment. Once all the selected $v_{pb\_individual}$'s are averaged, the impact of the increased amount of crystallites on the crystallization kinetics is removed, and the material-specific v_{pb} for crystal growth is obtained at the crystallization isotherm. All the material-specific v_{pb}'s of melt and cold crystallization measured with 2-D TtXRD are shown in Figure 3.5.

3.3.3. The Relationship between the Density of Initial Nuclei and the Time Elapsed to Reach the Crystallization Isotherm

It has been shown that n_i is affected by the time it takes to reach the crystallization isotherm in cold crystallization, such as the quenching rate from melt to glassy state[5,9], or aging both below and above the glass transition temperature, T_g[3,7,9]. For each isothermal cold crystallization experiment on 2-D TtXRD with programmed heating rates to reach the crystallization isotherms, it takes different amounts of time to heat the sample from its glassy state until the crystallization started, which is shown in Figure 3.1 to impact n_i, and the impact is quantitatively analyzed in this section.

For each isothermal crystallization experiment with polycrystalline growth, the initial nuclei will likely grow into crystallites of similar volumes due to mostly identical growth conditions. Therefore, for polycrystalline growth where the volume of individual crystallites can not be obtained, such as isothermal cold crystallization measured by the DSC, V_i in Equation (3.3) can be approximated as the average volume of those crystallites, i.e., V/n_i, where V is the total volume of the sample and n_i is the number of initial nuclei, and thus Equation (3.3) becomes

$$v_{pb\_individual} = \frac{kg\sqrt[3]{V / n_i}}{a_c} \tag{3.4}$$

Comparing Equations (3.3) and (3.4), with g = 1 and a_c = 1 for crystallization of CZX-1, n_i can be obtained as

$$n_i = \left(\frac{v_{pb\_bulk}}{v_{pb\_individual}} \right)^3 \tag{3.5}$$

Therefore, for isothermal cold crystallization of CZX-1 measured by 2-D TtXRD with programmed heating rates, with both v_{pb_bulk} and $v_{pb\_individual}$ available, n_i can be obtained with Equation (3.5).

As shown in Figure 3.2, v_{pb_bulk} of isothermal cold crystallization measured by the DSC is about the same as or even higher than v_{pb_bulk} of isothermal cold crystallization measured by 2-D TtXRD at the same isotherm, which indicates the samples on the DSC are divided into domains of around the same or smaller sizes as domains in the polycrystalline growth samples on 2-D TtXRD with an increased amount of crystallites in cold crystallization. Since the samples on the DSC are significantly larger in volume than samples on 2-D TtXRD, that indicates that the amount of crystallites in the DSC samples must be larger and proportional to the volume of the DSC samples, which further indicates that it is the density, rather than the number, of the initial nuclei that is material specific at each crystallization isotherm. Here the density of initial nuclei, d_i, is defined as n_i/m where m is the mass of the sample.

Therefore, for each isothermal cold crystallization experiment on 2-D TtXRD with programmed heating rates to reach the crystallization isotherms, d_i is obtained and plotted against the time interval between when the sample started to be heated from its glassy state (t_{glass}) and when the crystallization started (t_0) in Figure 3.4. No significant dependence of d_i on crystallization isotherms are exhibited, yet d_i exhibits a clear dependence on (t_0-t_{glass}), approximated with a linear function shown in Figure 3.4.

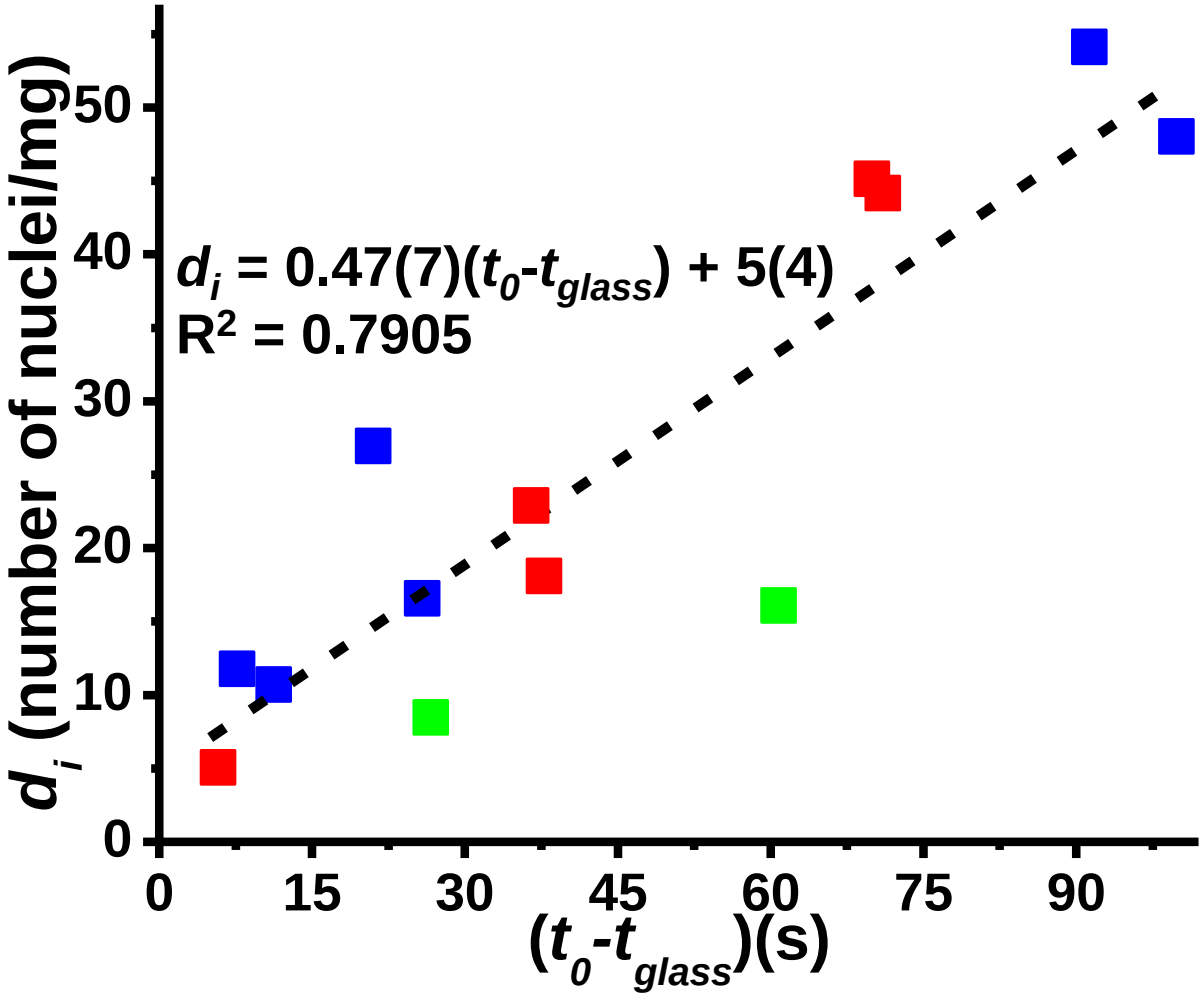

Figure 3.4. The relationship between d_i and (t_0-t_{glass}), obtained by cold crystallization with programmed heating rates to heat the samples from their glassy state to the crystallization isotherms at 80 °C (blue), 90 °C (red) and 100 °C (green). The linear function, shown as dashed line in the plot with its equation shown next to the line, is an empirical fit to the relationship. The numbers in parentheses after the slope and intercept of the linear function are each of their standard errors.

3.3.4. Growth Rates of Individual Crystallites from Isothermal Crystallization

Experiments with DSC

Isothermal melt crystallization on the DSC was performed at temperatures ranging between 145 and 162°C, which is close to the melting point, and within which it has been observed in 2-D TtXRD experiments, both previously and in this work, that mainly single

crystal growth occurs in each sample due to the slow nucleation rate and fast crystal growth rate[13,92]. Therefore, no correction with respect to number of initial nuclei is needed for isothermal melt crystallization on the DSC.

For isothermal cold crystallization on the DSC, it can be experimentally measured that a longer time elapsed (~2-5 minutes) to heat the sample from its glassy state to the crystallization isotherm, compared to the melt and cold crystallization on 2-D TtXRD in which the sample was heated or quenched to the isotherm instantly, and thus a higher density of initial nuclei is expected. Since d_i does not significantly depend on the crystallization isotherm, the same linear relationship between d_i and (t_0-t_{glass}) is applied to all the isothermal cold crystallization on the DSC to estimate d_i, and further n_i, which is then substituted into Equation (3.4) to estimate the material-specific $v_{pb\_individual}$ for each cold crystallization experiment on the DSC. All the material-specific v_{pb}'s of melt and cold crystallization measured with DSC are shown in Figure 3.5.

3.3.5. Probing the Mechanisms of Melt and Cold Crystallization with Transition Zone Theory

With the number of initial nuclei taken into account, material-specific values of v_{pb} of melt and cold crystallization of CZX-1 are obtained and plotted as a function of temperature in Figure 3.5. Our recently developed transition zone theory for crystal growth (TZT_c)[35], expressed in Equation (3.6), has been shown to accurately describe the kinetics of crystal growth for 14 diverse materials, and the enthalpic and entropic activation parameters, ΔH_c^*, ΔS_c^* and z_c, afford mechanistic understanding of the crystal growth process.

$$v_{pb} = \lambda \frac{k_B T}{h} \exp\left(\frac{-\Delta H_c^*}{R(T - T_K)} \right) \exp\left(\frac{\Delta S_c^*}{R} \left(\frac{T - T_K}{T_m - T} \right)^{z_c} \right) \tag{3.6}$$

Here T_K and T_m are the Kauzmann temperature and the melting point of the material, respectively, which can all be measured experimentally, and λ is the characteristic wavelength to form a standing wave pattern in the material, which equals to twice the lattice constant of the crystalline material[35]. Therefore, TZT_c can be applied to v_{pb}'s of melt and cold crystallization of CZX-1 with the enthalpic and entropic activation parameters ΔH_c^*, ΔS_c^* and z_c as fitting parameters, and comparison of those activation parameters indicates the similarity or difference in the mechanisms of melt and cold crystallization. v_{pb}'s of melt crystallization, cold crystallization and all crystallization of CZX-1 and the TZT_c fitting curves through each set of v_{pb}'s are shown in Figure 3.5. The activation parameters are shown in Table 3.1, which indicates that the parameters are statistically identical. Therefore, the mechanism of melt and cold crystallization is the same.

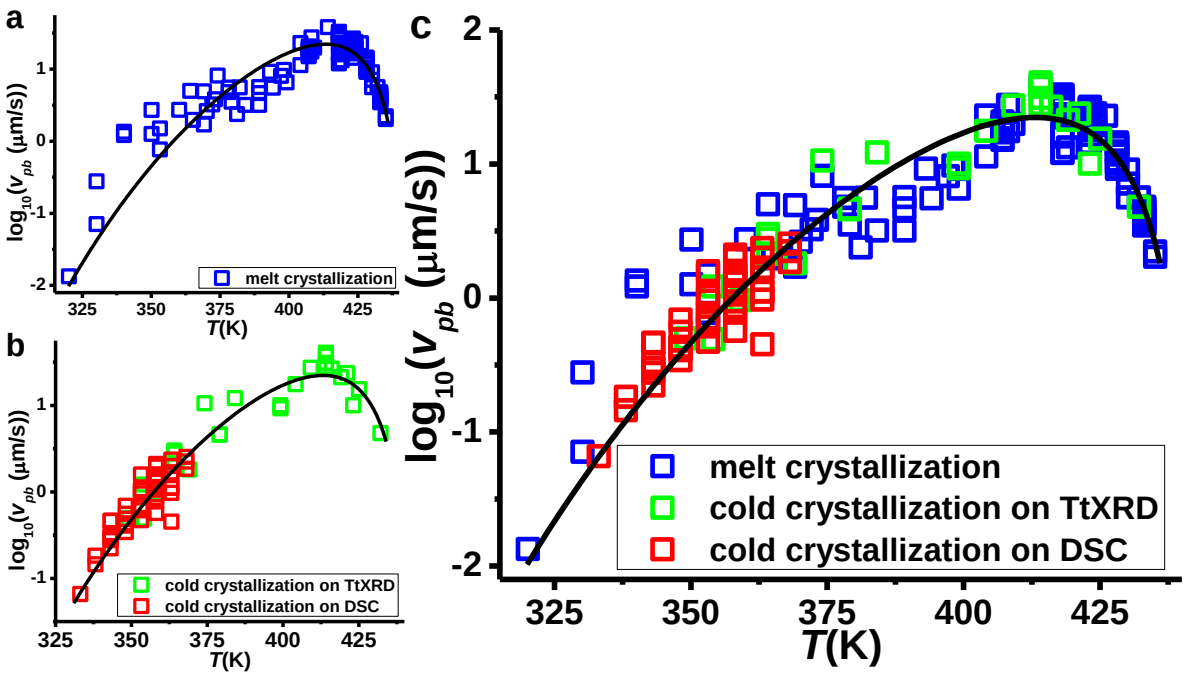

Figure 3.5. v_{pb}'s of melt and cold crystallization of CZX-1, obtained with the modified KJMA model and with the number of crystallites taken into account. The black curves through the data points are the TZT_c fits for (a) melt crystallization (b) cold crystallization (c) all.

Table 3.1. Enthalpic and entropic activation parameters of TZT_c fits to v_{pb} of melt crystallization, cold crystallization and all. T_m and T_K are experimentally measured with DSC and temperature-modulated DSC, respectively, and the experimental procedure of the measurement of T_K is described in Appendix A1. The number in the parentheses after each parameter is the standard error.

	Melt Crystallization	Cold Crystallization	All
T_m(K)	446	446	446
T_K(K)	150	150	150
ΔH_c^*(kJ/mol)	38.7(5)	37.8(7)	38.1(3)
ΔS_c^*(J/mol/K)	-5(1)	-7(2)	-7(1)
z_c	0.70(6)	0.64(11)	0.65(4)

3.4. Conclusion

Polycrystalline growth has been observed both in isothermal melt crystallization with heterogeneities in the melt or at deep supercooling and in isothermal cold crystallization, the latter of which has been shown to start with additional initial nuclei. Besides the previous

modification of the KJMA model by reintroducing the sample volume, sample geometry and crystal growth geometry, for polycrystalline growth, the volume of each individual crystallite, rather than the total volume of the sample, is introduced into the KJMA model to address the impact of the number of crystallites initiating and growing simultaneously in polycrystalline growth. For polycrystalline growth measured with 2-D TtXRD, with our in-group developed software, Ramdog, the kinetics of growth of each individual crystallite in each sample can be analyzed by monitoring the growth of the intensity of each spot on the corresponding series of 2-D X-ray images, and the number of initial nuclei can be calculated by comparing that to the bulk rate of crystal growth of the same sample. For cold crystallization, an empirical, linear function was fit to the relationship between the time taken to heat each sample from glassy state to crystallization isotherm and the corresponding density of initial nuclei obtained, such that the number of initial nuclei can be estimated for cold crystallization measured with the DSC to extract the material-specific kinetics of crystal growth since the direct analysis of the growth of each individual crystallite is not feasible.

The analysis described above, as well as the further modified KJMA model, is applied to the crystal growth kinetics of our model system, CZX-1. With the material-specific kinetics of crystal growth extracted, it is possible to carry out a mechanistic study with transition zone theory for crystal growth, which shows that despite the apparent difference in kinetics of crystal growth as has been observed previously, the material-specific kinetics of melt and cold crystallization are actually the same, and they likely share the same mechanism, which has enabled investigation of crystallization kinetics over a broader temperature range by both melt and cold crystallization.

CHAPTER 4

Kinetic Isotope Effect on Crystallization with Transition Zone Theory

4.1. Introduction

The kinetic isotope effect (KIE) is the ratio of reaction rates of two different isotopically labeled molecules in a chemical reaction. An isotopic substitution can greatly modify the reaction rate by modifying the activation barrier of the reaction, especially when the isotopic replacement is in a chemical interaction that is broken or formed in the rate limiting step[93], therefore, KIE has been widely applied in studies of reaction mechanisms, such as mechanisms of organometallic reactions, organic reactions and the solvent isotope effect on the hydrolysis reactions[94-97]. Comparatively, only a few studies of isotope effect have been reported in mechanisms of crystallization, most of which focused on the impact of isotopic substitution in the solvent or environment from which crystals form[98,99], and to our best knowledge, the studies on the isotope effect on crystallization from congruent melt are mostly qualitative, none of which was about isotope effect on crystallization kinetics[100,101]. Since kinetics of crystal growth from the congruent melt have been shown to be temperature dependent for most materials[5,46], temperature-dependent KIE's are anticipated to be extracted if KIE studies were conducted on crystal growth from the melt. Such temperature dependence of KIE is likely the obstacle to obtain quantitative, material-specific KIE on crystallization from the melt. In order to study the KIE on crystallization, and thus further investigate the chemical processes involved in crystallization, material-specific isotope effect on crystallization must be obtained.

Transition zone theory for crystal growth (TZT_c)[35], expressed in Equation (4.1), has been proposed to explain the mechanism of crystal growth, which extends the concept of transition state theory[34] to explain crystallization from the melt by considering a transition zone instead of a single transition state. In TZT_c, the attempt frequency for crystallization, $\lambda(k_BT/h)$, where λ equals twice the lattice constant, is the velocity of the propagation of the transition zone formed by the lattice vibrational modes that lead to formation of a standing wave pattern in the material. The probability for these lattice vibrational modes to cooperate is governed by the free energy of activation, which, unlike the traditional transition state theory, are temperature dependent based on the Kauzmann configurational entropy concept[36].

$$v_{pb} = \lambda \frac{k_B T}{h} \exp\left(\frac{-\Delta H_c^*}{R\left(T - T_K\right)} \right) \exp\left(\frac{\Delta S_c^*}{R} \left(\frac{T - T_K}{T_m - T} \right)^{z_c} \right) \tag{4.1}$$

In Equation (4.1), the enthalpic activation parameter, ΔH_c^*, indicates the energy required for the reorganization of the intermolecular/atomic interactions during crystallization; while the entropic activation parameters, ΔS_c^* and z_c, demonstrates the extent of structural organization necessary for crystallization and modulates the temperature dependence of the entropy of activation, respectively, and z_c has been shown to be correlated with ΔS_c^*. Both enthalpy and entropy of activation are modulated by the extent of cooperativity[47] required for crystallization, with limits of complete cooperativity at the Kauzmann temperature, T_K[36], and its absence at the melting point, T_m[35]. TZT_c has been shown to accurately describe the kinetics of crystal growth which are represented by v_{pb}, the velocity of the phase boundary between the melt phase and the crystalline phase, and the enthalpic and entropic activation parameters, ΔH_c^*, ΔS_c^* and z_c, have been shown to afford mechanistic understanding of the crystal growth process. Therefore, it is possible to apply TZT_c to study the isotope effect on crystallization by

comparing enthalpic and entropic activation parameters of crystallization for a material with different isotopic substitution.

Halozeotype materials[18,43] are formed by metal-halide framework and templating cations that either have a higher charge density or are able to hydrogen bond to the metal-halide framework. Alkylammonium cations are commonly used as templates (structure-directing agents) because of both the relative ease with which hydrogen bonding occurs to the framework and the rather large variation in size and shape that are available to template with. In the absence of the structure-directing hydrogen bonding of the template or the high charge density, no crystallization will take place[102]. Therefore, templates are critical to crystallization of halozeotype materials. Despite its importance, the influence of the template on the crystallization process remains unclear.

In this chapter, the impact of the template reorientation on crystallization is studied by investigating the impact of differently isotopically substituted templates on the kinetics of crystallization. The model system, halozeotype CZX-1 ($[HN(CH_3)_3]CuZn_5Cl_{12}$), is a templated derivative of $ZnCl_2$, in which 1/6 of the Zn^{2+} is replaced by Cu^+, and trimethylammonium cation is added as charge balancing and structural-directing template by forming hydrogen bonds to one of the four sets of chloride anions inside each metal-halide cage, as shown in Figure 4.1a and b. CZX-1 crystallizes in the cubic space group $I\bar{4}3m$ with a = 10.5887(3) Å, and is isostructural to sodalite (see Figure 4.1c)[43]. In order to study the impact of template reorientation on crystallization of CZX-1, and to further understand the mechanism of CZX-1 crystallization on a molecular level, CZX-1 was prepared with various deuterium-substituted templates, namely, d_0-CZX-1, in which none of the hydrogen atoms in the template is substituted by deuterium; d_1-CZX-1, in which the hydrogen atom in the hydrogen bonding

between the template and the metal-halide cage is substituted by deuterium; d_9-CZX-1, in which the hydrogen atoms in the methyl groups are substituted by deuterium, and d_{10}-CZX-1, in which all the hydrogen atoms in the template are substituted by deuterium. TZT_c is applied to the experimentally measured kinetics of crystal growth of d_0-, d_1-, d_9- and d_{10}-CZX-1 to obtain the enthalpic and entropic activation parameters for each of them. Comparison of those parameters between the lighter species (d_0- and d_1-CZX-1) and the heavier species (d_9- and d_{10}-CZX-1) indicates the influence of the mass of the template, or the entire template reorientation, on crystallization, while comparison of those parameters between the hydrogen-bonding species (d_0- and d_9-CZX-1) and the deuterium-bonding species (d_1- and d_{10}-CZX-1) indicates the influence of hydrogen bonding between the template and the metal-halide cage on crystallization.

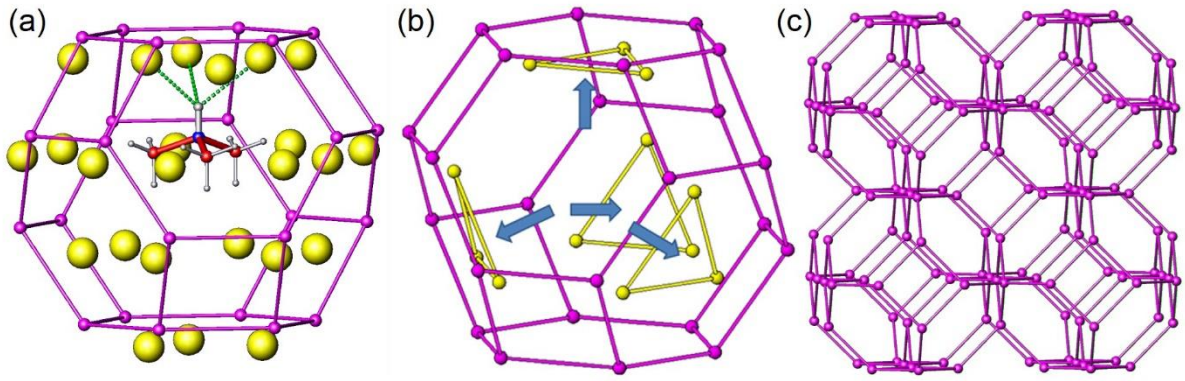

Figure 4.1. (a) Hydrogen bonding (green dashed lines) between the trimethylammonium template and the set of chloride anions of the metal halide cage. (b) Four equivalent sets of chloride anions that can form hydrogen bonding to the template. (c) Body-centered cubic arrangement of the metal halide cages.

4.2. Experimental Methods

4.2.1. Material Preparation and Measurement of the Kauzmann Temperature

All manipulations were performed under an inert N_2 atmosphere in a glovebox or using vacuum lines. $DN(CD_3)_3Cl$ (Cambridge Isotope Laboratories) and $HN(CH_3)_3Cl$ (Alrdich) was purified via double sublimation at 130°C for 6h prior to use. $DN(CH_3)_3Cl$ and $HN(CD_3)_3Cl$ were prepared by bubbling $N(CH_3)_3$ (Matheson) /$N(CD_3)_3$ (Cambridge Isotope Laboratories) gas into wt. 35% DCl/D_2O (Aldrich)/ wt. 37.1% HCl/H_2O (Fisher Scientific) solutions, respectively, followed by evaporation of the solvents at 100 °C and sublimation of the yielded $DN(CH_3)_3Cl$ and $HN(CD_3)_3Cl$ at 130 °C. The purity of the sublimed $H/DN(CH/D_3)_3Cl$ was confirmed by powder X-ray diffraction (XRD, INEL CPS-120). $ZnCl_2$ and CuCl were prepared and purified as reported previously. d_1-, d_9- and d_{10}-CZX-1 were prepared by melting together $ZnCl_2$, CuCl and the corresponding templating $H/DN(CH/D_3)_3Cl$ at a molar ratio of 5:1:1, same as synthesis of d_0-CZX-1[18,86]. The purity of the synthesized d_1-, d_9- and d_{10}-CZX-1 was confirmed by differential scanning calorimetry (DSC, TA Instruments Q2000), and lattice constants of d_1-, d_9- and d_{10}-CZX-1 were measured by powder X-ray diffraction (XRD, INEL CPS-120).

The Kauzmann temperatures[36] of d_1-, d_9- and d_{10}-CZX-1 was each measured with temperature-modulated DSC (TA Instruments Q2000), the same as for d_0-CZX-1[35] and the experimental procedure is described in Appendix A1.

4.2.2. Isothermal Melt and Cold Crystallization

Isothermal melt and cold crystallization of d_0-CZX-1 were performed as described in Chapter 3 as well as in previously published works[13]. Isothermal crystallization of d_1-, d_9- and

d_{10}-CZX-1 were performed with DSC (TA Instruments Q2000) at crystallization isotherms between 145 and 160 °C (between 138.6 and 157.6 °C for d_{10}-CZX-1) for melt crystallization and between 50 and 100 °C for cold crystallization. Isothermal melt crystallization of d_1-, d_9- and d_{10}-CZX-1 were also performed with 2-D temperature- and time-resolved synchrotron X-ray diffraction (2-D TtXRD) on beamline 11-ID-B (60 KeV, $\lambda = 0.2114$ Å, collimated beam 0.5 × 0.5 mm) at the Advanced Phonon Source (APS), Argonne National Laboratory at crystallization isotherms between 66 and 166 °C which were reached within one second with the new quenching furnace. The experimental procedures for isothermal melt and cold crystallization of d_1-, d_9- and d_{10}-CZX-1 on the DSC and on 2-D TtXRD are the same as those for d_0-CZX-1 as described in Chapter 3.

4.3. Results and Discussion

4.3.1 The Isotope Effect on the Overall Kinetics of Crystallization

The material-specific crystallization kinetics, represented as the velocity of the phase boundary, v_{pb}, of d_1-, d_9- and d_{10}-CZX-1, were obtained using the same methods as described for d_0-CZX-1 in Chapter 3. As shown in Figure 4.2, v_{pb} of d_0-, d_1-, d_9- and d_{10}-CZX-1 are slightly different. However, with the spread in values of v_{pb} at each crystallization isotherm, especially around the isotherm where crystallization rates are the highest, such differences are sometimes even less than the experimental error. Furthermore, due to the temperature dependence of v_{pb}, different KIE can be extracted at different temperatures. Therefore, TZT_c, as described in Equation (4.1), is fit to crystallization kinetics to obtain enthalpic and entropic activation parameters, ΔH_c^*, ΔS_c^* and z_c, for d_0-, d_1-, d_9- and d_{10}-CZX-1, such that the impact of isotopic substitution can be investigated by comparing both those parameters and the

magnitude and temperature dependence of enthalpy and entropy of activation, $\Delta H_c^{\ddagger}$ and $\Delta S_c^{\ddagger}$, as shown in Figure 4.3 and Table 4.1.

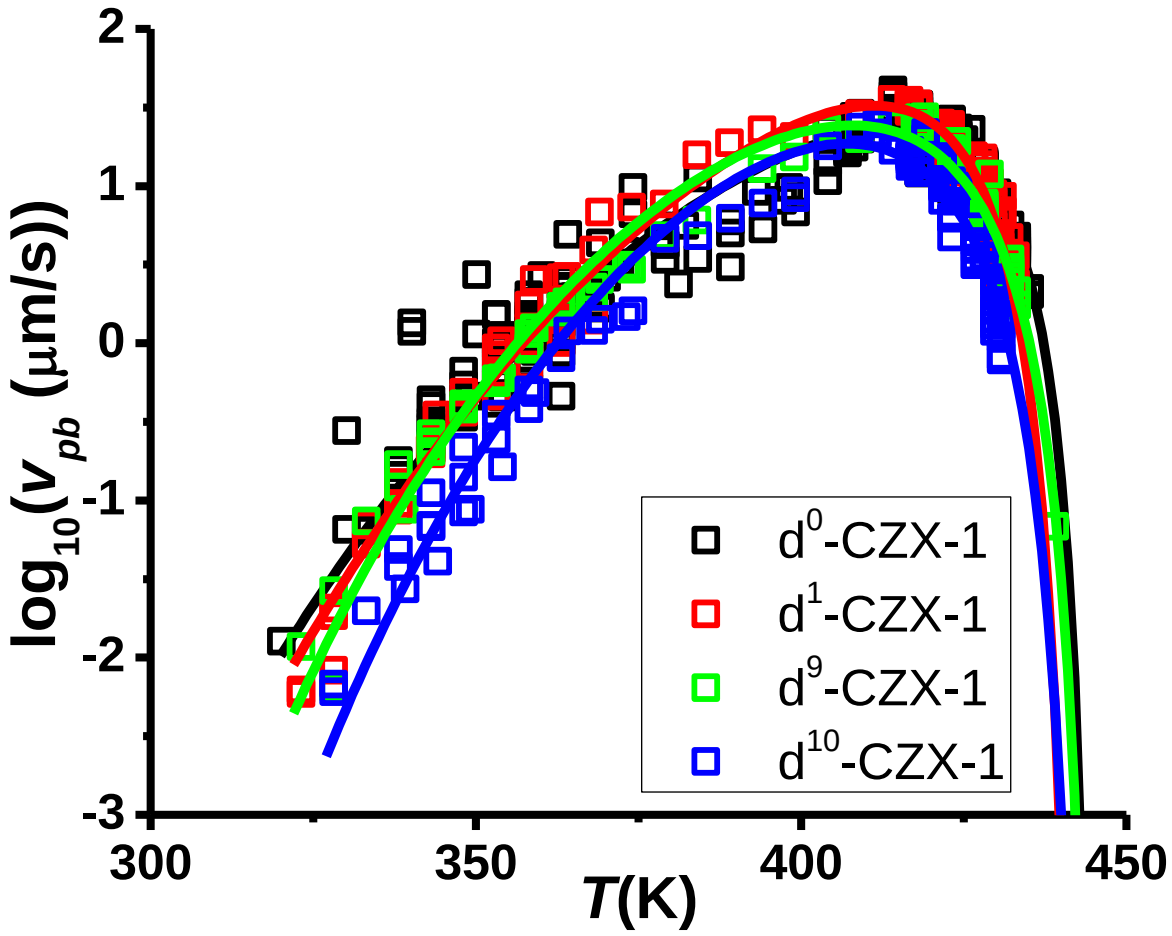

Figure 4.2. Data points of v_{pb} with curves of the best fit to Equation (4.1) for d_0-, d_1-, d_9- and d_{10}-CZX-1.

Figure 4.3. The coloring in each part of the figure is the same as in Figure 4.2, with d_0-, d_1-, d_9- and d_{10}-CZX-1 represented by black, red, green and blue colors, respectively. The temperature dependent (a) $\Delta H_c^{\ddagger}$ and (b) $\Delta S_c^{\ddagger}$ for d_0-, d_1-, d_9- and d_{10}-CZX-1, obtained from TZT_c fits to v_{pb}'s of crystallization of d_0-, d_1-, d_9- and d_{10}-CZX-1, are plotted over the entire temperature range in which v_{pb} was measured. The formulae of the temperature-dependent $\Delta H_c^{\ddagger}$ and $\Delta S_c^{\ddagger}$ are incorporated into each figure. The insert in (b) is an enlarged T = 400 – 445 K portion of the plot. The experimentally measured T_K and the activation parameters ΔH_c^*, ΔS_c^* and z_c from TZT_c fits to v_{pb}'s of crystallization of d_0-, d_1-, d_9- and d_{10}-CZX-1 are plotted against each of their moment of inertia relative to that of d_0-CZX-1 in parts (c) – (f) of the figure, respectively.

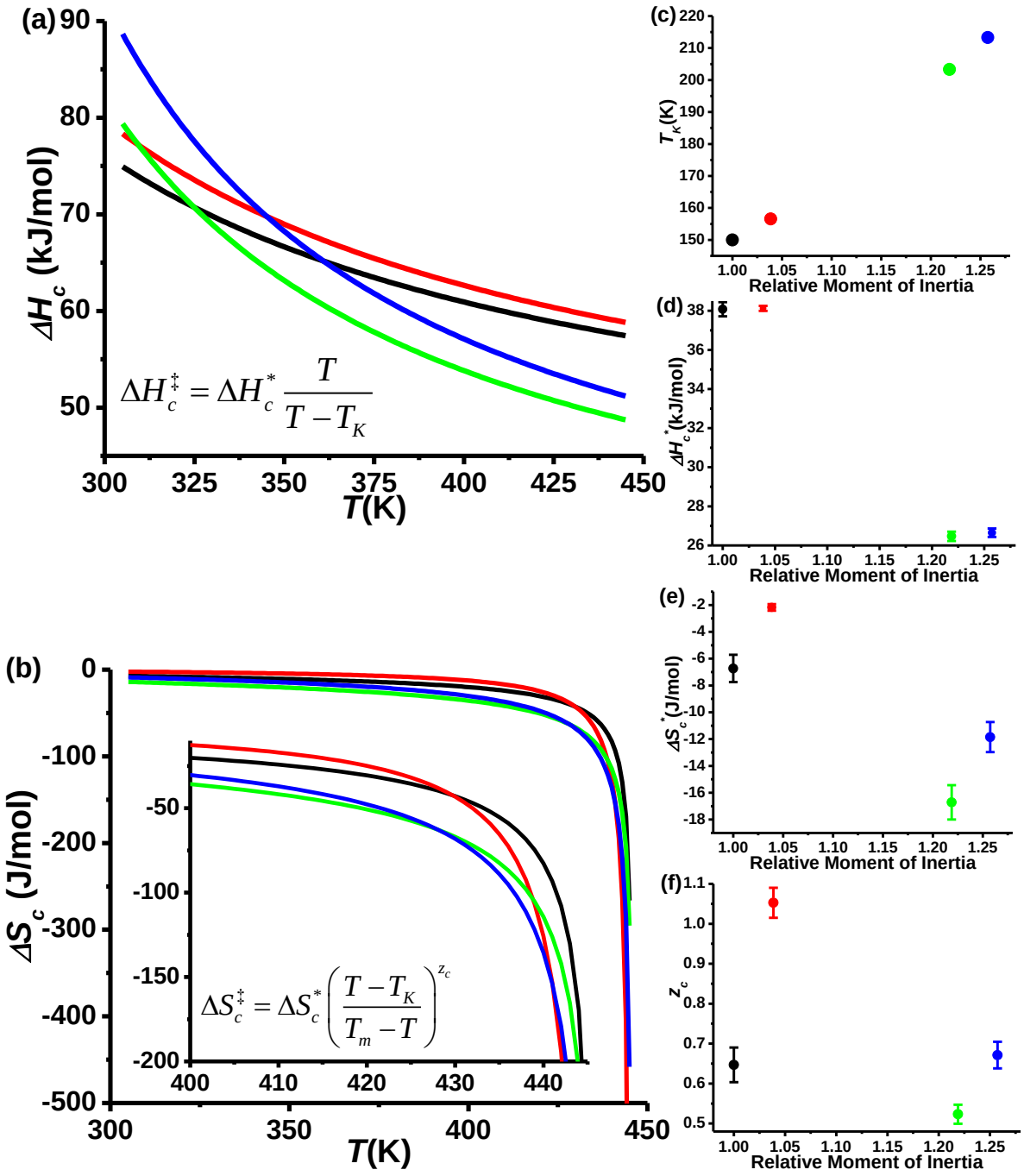
(a)
ΔH_c (kJ/mol)
T(K)
$\Delta H_c^{\ddagger} = \Delta H_c^{*} \frac{T}{T - T_K}$
(b)
ΔS_c (J/mol)
T(K)
$\Delta S_c^{\ddagger} = \Delta S_c^{*} \left(\frac{T - T_K}{T_m - T} \right)^{z_c}$
(c)
T_K(K)
Relative Moment of Inertia
(d)
ΔH_c^{*}(kJ/mol)
Relative Moment of Inertia
(e)
ΔS_c^{*}(J/mol)
Relative Moment of Inertia
(f)
z_c
Relative Moment of Inertia

Table 4.1. Enthalpic and entropic activation parameters of TZT_c fits to v_{pb}'s of crystallization of d_0-, d_1-, d_9- and d_{10}-CZX-1. The number in the parentheses after each parameter is the standard error. The melting point, T_m and the Kauzmann temperature, T_K, were measured experimentally with DSC and temperature-modulated DSC, respectively, and the experimental procedure of the measurement of T_K is described in Appendix A1.

	d_0-CZX-1	d_1-CZX-1	d_9-CZX-1	d_{10}-CZX-1
T_m(K)	446	446	446	446
T_K(K)	150	157	203	213
ΔH_c^*(kJ/mol)	38.1(4)	38.12(13)	26.5(2)	26.6(2)
ΔS_c^*(J/mol/K)	-7(1)	-2.2(2)	-17(1)	-12(1)
z_c	0.64(4)	1.05(4)	0.52(2)	0.67(3)

4.3.2. Impact of Template Mass on Crystallization Kinetics

As shown in Figure 4.3, the enthalpic and entropic activation parameters (ΔH_c^*, ΔS_c^* and z_c), as well as the temperature dependent enthalpy and entropy of activation ($\Delta H_c^\ddagger$ and $\Delta S_c^\ddagger$), exhibits significant inertial impacts, which indicates that the mass of the template, and thus the reorientation of the entire template significantly affects the crystallization kinetics.

As a first approximation, the template-cage interaction can be treated as a two-body problem, with the reorientation of the template modeled by the rotational and vibrational modes, the energy levels of which are both inversely proportional to the reduced mass. Therefore, similar to what has been argued in the H-D isotope effect in molecular systems[103,104], the increased template mass, and thus the increased reduced mass leads to more narrowly spaced rotational and vibrational energy levels, such that the higher energy levels are more likely to be populated. Enthalpically, this indicates that the template-cage interaction of CZX-1 with heavier template (d_9- and d_{10}-CZX-1) is more likely to be at its excited states, and thus they are more likely to be activated with less energy (enthalpy) required than their lighter analogs (d_0- and d_1-CZX-1), hence the lower ΔH_c^*, as shown in Figure 4.3d.

Similar to the traditional transition state theory[34], the $\Delta H_c^{\ddagger}$ of crystallization is also dominated by the energy required for reorganizing (making or breaking) bonding interactions in the given transformation. Additionally, $\Delta H_c^{\ddagger}$ of crystallization is determined by the cooperativity of the system[35,47]. As the temperature of a liquid approaches the Kauzmann temperature, T_K[36], the loss of configurational microstates requires an increased size of the cooperative region for each activation event; correspondingly, an increased number of bonding interactions need to be reorganized simultaneously, and thus a higher $\Delta H_c^{\ddagger}$ is required. If a liquid could be supercooled to T_K, the entire sample would need to transform as a single cooperative region; the amount of energy required in the transformation makes it essentially an impossible condition. Therefore, $\Delta H_c^{\ddagger}$ of crystallization is proportional to the size of the cooperative regions, which is temperature-dependent and increases as the temperature approaches T_K. The experimentally measured T_K's, shown in Figure 4.3(c), has an approximately linear relationship with the relative moment of inertia, which indicates T_K is mostly affected by the mass of the template with minimal impact from hydrogen bonding. As the temperature decreases, for CZX-1 with heavier templates, T_K is approached more rapidly, and thus the size of the cooperative regions increases more rapidly. Therefore, stronger temperature dependence of $\Delta H_c^{\ddagger}$ is observed as the mass of the template increases, as shown in Figure 4.3a.

Entropically, with an increased template mass, the higher energy levels of the template-cage interaction are more likely to be populated, and thus more microstates are accessible, such that d_9- and d_{10}-CZX-1 melts have higher entropy and require more rearrangements in the crystallization process, hence the more negative ΔS_c^*. Due to the correlation between ΔS_c^* and z_c[35], d_9- and d_{10}-CZX-1 also exhibits smaller z_c, suggesting less temperature dependence of

$\Delta S_c^{\ddagger}$, which is observed and shown in Figures 4.3b and 4.3f. With the $\Delta S_c^{\ddagger}$ for crystallization of d_9- and d_{10}-CZX-1 being already more negative (larger in magnitude), the change in the magnitude of $\Delta S_c^{\ddagger}$ becomes not as significant, hence the less temperature – dependent $\Delta S_c^{\ddagger}$, as shown in Figure 4.3b.

4.3.3. Impact of Hydrogen Bonding on Crystallization Kinetics

As has been discussed above, minimal impact from hydrogen bonding is exhibited on T_K's of d_0-, d_1-, d_9- and d_{10}-CZX-1. By contrast, ΔH_c^*, ΔS_c^* and z_c exhibit significant hydrogen bonding impact, which increases both ΔH_c^* and ΔS_c^*, such that the inertial effect is masked out on ΔH_c^* and even reversed on ΔS_c^* for the deuterium bonding species (d_1- and d_{10}-CZX-1) compared to the hydrogen bonding species (d_0- and d_9-CZX-1), as shown in Figures 4.3d and 4.3e. Due to the correlation between ΔS_c^* and z_c[35], an increased z_c is also observed for the less negative ΔS_c^* of the deuterium bonding species, indicating a stronger temperature dependence of $\Delta S_c^{\ddagger}$, as shown in Figures 4.3b and 4.3f. This result suggests that the hydrogen bonding between the template and the metal-halide cage significantly affects the kinetics of crystallization, likely by affecting the directing ability of the template to rearrange the metal halide cages into an ordered structure by template reorientation during crystallization.

Enthalpically, increased ΔH_c^* and $\Delta H_c^{\ddagger}$ are observed for each of the deuterium bonding species compared to their hydrogen bonding analogs, which suggests that an increased amount of energy (enthalpy) is required for bond reorganization in the activation process of crystallization, likely due to a stronger template-cage interaction that needs to be reorganized during template reorientation with the deuterium substitution in the hydrogen bonding between the template and the metal-halide cage. As has been discussed in the previous section, the

temperature dependence of $\Delta H_c^{\ddagger}$ corresponds to the temperature dependence of the cooperativity of the system which is mainly affected by T_K, and thus should mostly exhibit inertial impact with no significant impact from the deuterium substitution in the hydrogen bonding.

Entropically, less negative ΔS_c^*, as well as less negative $\Delta S_c^{\ddagger}$ at low temperatures, are observed for the deuterium bonding species compared to their hydrogen bonding analogs, which suggests a stronger directing force from the template reorientation in crystallization with the deuterium substitution in the template-cage hydrogen bonding, and likely also further suggests a stronger template-cage interaction with the deuterium substitution. However, as the temperature approaches the melting point, $\Delta S_c^{\ddagger}$ for the deuterium bonding species becomes more negative than $\Delta S_c^{\ddagger}$ for the hydrogen bonding species due to their stronger temperature dependence. It is likely that as the temperature approaches the melting point, the cooperativity of the metal-halide cages in the system is lost, yet the stronger template-cage interaction with the deuterium bonding tends to hold the cages together at where they are in the melt phase, thus more rearrangements are needed in the activation process of crystallization to separate the cages and rearrange them through smaller cooperative regions, which results in more negative $\Delta S_c^{\ddagger}$ for the deuterium bonding species.

4.4. Conclusion

Kinetic isotope effect (KIE) studies have been widely applied to investigate reaction mechanism in molecular reactions, yet few KIE studies have been conducted on mechanism of crystallization from the congruent melt, during which temperature dependent KIE's are likely to be extracted by only comparing the rates of crystallization. In this work, we have studied

the crystallization kinetics of the halozeotype CZX-1 with deuterium substitutions in the hydrogen bonding to the metal-halide cage and/or the methyl groups of its trimethylammonium cation template (d_0-, d_1-, d_9- and d_{10}-CZX-1), and with our recently developed transition zone theory for crystallization, we have investigated the isotope effect on crystallization kinetics of CZX-1 by comparing the enthalpy and entropy of activation of crystallization for CZX-1 with differently isotopically substituted templates to understand the role of the template reorientation in crystallization. Only inertial impact from the template has been shown on the experimentally measured Kauzmann temperature, T_K, which indicates that T_K, and furthermore the cooperativity of the material, is significantly dependent on the mass of the template with minimal impact from the hydrogen bonding to the metal-halide cage. By contrast, both the changed template mass and the isotopic substitution in the hydrogen bonding between the template and the metal-halide cage exhibit significant impact on the enthalpy and entropy of activation of crystallization, which indicates that the template reorientation likely plays a dominant role in the activation process of crystallization of CZX-1, with impacts from both the template-cage interaction and the inertia of the entire template.

With the transition zone theory for crystallization, material-specific isotope effects on kinetics crystallization can be obtained by comparing the enthalpy and entropy of activation for crystallization, which affords mechanistic details of crystallization, and further demonstrates the possibility of higher-level mechanistic investigations with transition zone theory for crystallization by utilizing measurements of activation processes to articulate details of chemical processes involved in crystallization.

CHAPTER 5

Transition Zone Theory of the Glass Transition

This chapter was previously published: Martin, J. D.; Hou, F. *Nature* **2015**, Under Review.

5.1. Introduction

Glasses, both naturally occurring and synthetic, have captured human imagination for millennia, with artisans and industrialists perfecting strategies to fabricate and manipulate them for diverse purposes. Nevertheless an understanding of the atomic and molecular processes and structures that create and define the glass state has been much more difficult to resolve. In 1995, Andersen suggested, "The deepest and most interesting unsolved problem in solid state theory is probably the theory of the nature of glass and the glass transition."[1] Subsequently, numerous reports have articulated the current state of understanding, and enumerated further perspectives[4,23-26,105,106]. Divergent viewpoints wrestle with the question whether the glass transition is a kinetic or thermodynamic phenomenon. A majority of theories are based on the classic VFT theory of liquid relaxation and viscosity[28-30], and/or the expectation of a temperature dependent crossover from VFT to Arrhenius theory. Having recently articulated our Transition Zone Theory (TZT) that requires no such crossover temperature while accurately describing/predicting the temperature dependent rates of crystallization and relaxation over the entire temperature ranges T_g (glass transition temperature) to T_m (melting point) and T_g to T_c (critical point), respectively[35], we here consider the application of TZT to the glass transition enigma.

Like Eyring's molecular based Transition State Theory[34], TZT is based on an articulation of the attempt frequency and probability of the transforming events. Instead of the events being molecular collisions, TZT recognizes that the structural reorganization required for crystallization and viscous relaxation requires Adam-Gibbs-type[47] cooperative interactions of phonons[2,3].

The attempt frequency for crystallization, $\lambda(k_BT/h)$, is the product of the number of lattice vibrational modes that lead to formation of the transition zone for crystal growth and the velocity of the transition zone; λ is a characteristic wavelength of vibrations that lead to growth, equal to twice the average lattice dimension. The probability for these lattice vibrational modes to cooperate is governed by the free energy of activation. Unlike transition state theory[34], in the condensed phase the entropy and enthalpy of activation are not temperature independent constants. Instead, for crystallization, at the Kauzmann temperature, T_K[36], the enthalpy of activation, $\Delta H_c^{\ddagger}$, goes to infinity while the entropy of activation, $\Delta S_c^{\ddagger}$, goes to zero. By contrast, because with increasing temperature the configurational entropy of the reactant ergodic liquid increases much faster than that of the crystal transition zone, the $\Delta H_c^{\ddagger}$ decreases while the $\Delta S_c^{\ddagger}$ increases; $\Delta S_c^{\ddagger} \rightarrow -\infty$ at T_m. Together these yield the TZT_c expression, Equation (5.1), shown to accurately describe crystal growth rates of fourteen diverse materials ranging from the fragile small molecule *o*-terphenyl, OTP, to the strong framework of SiO_2[35].

$$v_{pb} = \lambda \frac{k_B T}{h} \exp\left(\frac{-\Delta H_c^*}{R\left(T - T_K\right)} \right) \exp\left(\frac{\Delta S_c^*}{R} \left(\frac{T - T_K}{T_m - T} \right)^{z_c} \right) \tag{5.1}$$

Here v_{pb} is the velocity of the crystallization phase boundary, ΔH_c^* and ΔS_c^* are enthalpic and entropic activation parameters, and z_c is an empirical parameter that modulates the temperature dependence and is strongly correlated to ΔS_c^*.

By contrast, for viscous relaxation, only phonons with the fastest wave velocity, i.e. the speed of sound, v_s, can travel through the entire liquid leading to rearrangements necessary to make it ergodic. Thus the attempt frequency for dynamic viscous relaxation ($1/\eta$) is $(4\pi/v_s^2\rho)(k_BT/h)$, where ρ is the material's density. The probability of relaxation is also governed by temperature dependent free energy of activation. However, while the Adam-Gibbs-type cooperativity[47] results in similar temperature dependence of the enthalpy of activation for relaxation, $\Delta H_{rlx}^{\ddagger}$, to that observed for crystal growth, inverse temperature dependence is observed for the entropic probability of relaxation, $\Delta S_{rlx}^{\ddagger}$. At T_K the transition zone to achieve relaxation to an ergodic liquid, like the ergodic liquid itself, essentially has a single configuration, whereas the reactant non-ergodic liquid has a large number of configurations, thus $\Delta S_{rlx}^{\ddagger} \rightarrow -\infty$ at T_K. By contrast at the critical point, T_c, the configurational entropy of the supercritical fluid, non-ergodic and ergodic liquids are equivalent, thus $\Delta S_{rlx}^{\ddagger} \rightarrow 0$. Together these yield the TZT_{rlx} expression, Equation (5.2), shown to accurately describe viscous relaxation from T_g to T_m for seventy diverse materials ranging from the very fragile methane to the strong liquid network of SiO_2[35].

$$\frac{1}{\eta} = \frac{4\pi}{v_s^2\rho}\frac{k_BT}{h}\exp\left(\frac{-\Delta H_{rlx}^*}{R\left(T-T_K\right)}\right)\exp\left(\frac{\Delta S_{rlx}^*}{R}\left(\frac{T_c-T}{T-T_K}\right)^{z_{rlx}}\right) \tag{5.2}$$

Here ΔH_{rlx}^* and ΔS_{rlx}^* are enthalpic and entropic activation parameters, and z_{rlx} is an empirical parameter that modulates the temperature dependence and is strongly correlated to ΔS_{rlx}^*, but also accounts for the pressure dependence of T_K.

5.2. Transition Zone Theory of the Glass Transition (TZT_{glass})

Because the $\Delta S_c^{\ddagger}$ and $\Delta S_{rlx}^{\ddagger}$ exhibit opposing temperature effects, and $\Delta H_c^{\ddagger}$ should be greater than $\Delta H_{rlx}^{\ddagger}$, for most materials there will be a temperature at which the free energy of activation for crystallization and relaxation are equivalent, $\Delta G_c^{\ddagger} = \Delta G_{rlx}^{\ddagger}$, Equation (5.3).

$$\left(\Delta H_c^*\left(\frac{T}{T-T_K}\right)\right)-T\left(\Delta S_c^*\left(\frac{T-T_K}{T_m-T}\right)^{z_c}\right)=\left(\Delta H_{rlx}^*\left(\frac{T}{T-T_K}\right)\right)-T\left(\Delta S_{rlx}^*\left(\frac{T_c-T}{T-T_K}\right)^{z_{rlx}}\right) \quad (5.3)$$

The respective temperature dependence of the $\Delta G^{\ddagger}$ of crystallization and relaxation for *o*-terphenyl (OTP) are shown in Figure 5.1, for which the temperature of the equivalence point can be solved numerically. At the equivalence temperature, the probability of crystallization is equal to the probability of liquid relaxation. Below this temperature, the probability of crystallization is greater than that of relaxing to a bulk ergodic liquid. However, under these conditions, crystal growth can only propagate over length scales that molecules rearrange cooperatively during relaxation, presumably related to length scale of liquid intermediate range order of the pre-quenched melt, i.e. "local ergodicity." Various measurements have suggested that the cooperative region for bulk glass formers is 1-4 nm in the vicinity of T_g[107-110].

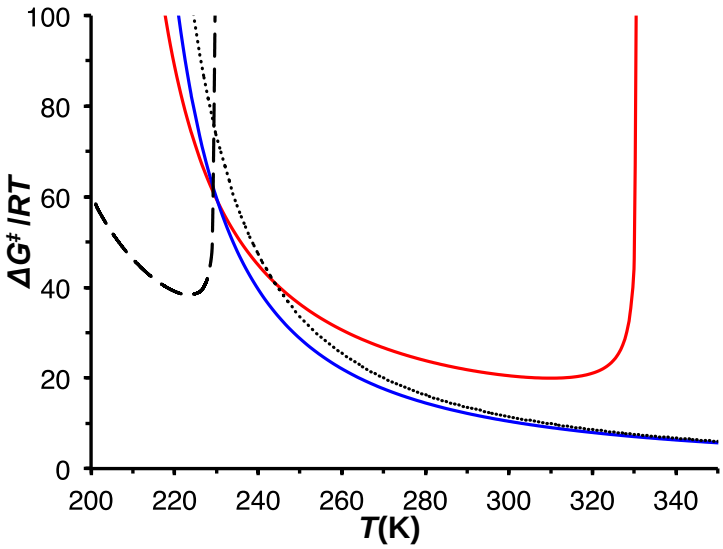

Figure 5.1. RT normalized free energy of activation as a function of temperature. Data are plotted (relaxation (blue) and crystallization (red)) using activation parameters for OTP from reference 34, for which $\Delta G_c^{\ddagger} = \Delta G_{rlx}^{\ddagger}$ at 230 K. The dotted line represents a time-temperature shifted relaxation by using z_{rlx} = 1.55 (instead of 1.47) which accounts for literature reported T_g = 244 K[52]. The dashed line represents the proposed function for aperiodic crystallization with $T_g = T_{m\,APC}$ = 230 K and T_K' = 170 K.

In a significantly structured liquid, local ergodicity may reach length scales where the onset of long-range order is observed. Under such conditions nano-domain crystallization (NDC) may occur. If, however, the local ergodicity of the liquid is smaller than the length scale of long – range order, then below the $\Delta G^{\ddagger}$ equivalence point, an intermediate range crystal-like organization, described as aperiodic crystallization (APC), occurs with greater probability than bulk crystallization or relaxation. However, while insufficiently organized to exhibit long-range order, the APC is too organized to allow bulk relaxation to an ergodic liquid. The APC process is conceptually related to the previously described random first-order transition theory of glass formation[26,105]. This condition, where crystallization and viscous relaxation mutually frustrate the other process, thus defines the metastable glassy state.

Because bulk crystallization occurs from the relaxed ergodic liquid[22], the rate of crystal growth is anticipated to be independent of sample history. By contrast, the rate of relaxation exhibits significant sample history dependence, and thus a history dependent $\Delta G^{\ddagger}$ equivalence point; the likely origin of the previously described time-temperature superposition[31,111]. According to TZT_{rlx}, $\Delta S_{rlx}^{\ddagger}$ is dependent upon the ratio of the number of configurations of the transition zone, $W_{rlx}^{\ddagger}$ and the reactant phase, $W_{nonerg\ liq}$; $\Delta S_{rlx}^{\ddagger} = R\ln(W_{rlx}^{\ddagger}/W_{nonerg\ liq})$[35]. $W_{rlx}^{\ddagger}$ is dependent on the temperature of the relaxation isotherm as well as the frequency of the measurement. The isotherm dependence being a result of Adam-Gibbs-type cooperativity with larger cooperative regions (smaller $W_{rlx}^{\ddagger}$) observed at lower temperature[47]. The frequency-of-measurement dependence results from the ability of different size molecular fragments to respond to an external stimulus on the timescale of the measurement, resulting in a smaller $W_{rlx}^{\ddagger}$ at higher frequency. $W_{nonerg\ liq}$ is determined by the relaxation isotherm temperature, as well as the difference in pre-quench and isotherm temperatures and the rate at which it is quenched, $f(\Delta T)$, or the extent and frequency at which it is mechanically perturbed, $f(\Delta v)$.

The effect of time-temperature quenching on the configurational entropy of the liquid is schematically represented in Figure 5.2. At the critical temperature, T_c (not shown), the configurational entropy of non-ergodic and ergodic liquids is equivalent. Below T_c, as the quenching rate $f(\Delta T)$ or $f(\Delta v)$ exceeds the rate of relaxation, the temperature dependent configurational entropy lines of the non-ergodic and ergodic liquids diverge, increasing $W_{nonerg\ liq}$. Thus, more extreme thermal or mechanical quenching results in more negative $\Delta S_{rlx}^{\ddagger}$, depressing the rate of relaxation. We have not yet obtained data to define these time-temperature effects, but propose the effect can be approximated with a larger value of z_{rlx} in

Equations (5.2) and (5.3), as demonstrated in Figure 5.1 where the dotted line represents such a slightly depressed rate of relaxation.

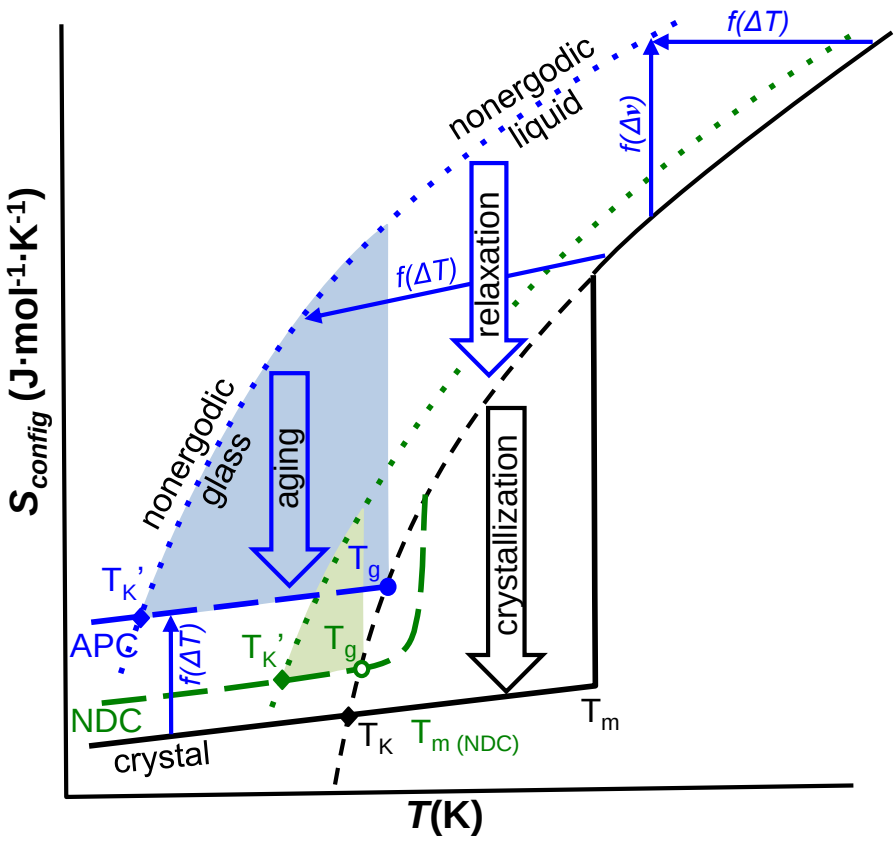

Figure 5.2. Schematic of the temperature dependence of configurational entropy. Solid black lines represent the thermodynamically favored liquid and crystalline states. The short-dashed line represents a supercooled melt. Rapid and/or deep quenching by $f(\Delta T)$ or $f(\Delta \nu)$ (solid blue arrows) determine the shifts to a non-ergodic liquid (dotted blue line) and APC (long-dashed blue line). Quenching into the shaded region results in glass formation, which ages with time. Box arrows represent the activated processes of relaxation, crystallization, and glass aging. Shallow quenching results in shifts to a non-ergodic liquid with smaller number of configurations (green dotted line). For a highly structured liquid NDC (green long-dashed line) is observed instead of APC.

The configurational entropy of the APC and NDC, for which the extent of order is determined by the magnitude of the local ergodicity, will also be dependent on sample history. When a system is quenched, the local ergodic length scale of the pre-quenched melt is projected onto the free energy landscape of the lower temperature isotherm. If the system is quenched to an isotherm where the probability of relaxation is less than the probability of crystal growth,

this becomes the maximum length scale over which crystallization can occur. The shorter the locally ergodic length scale, the greater the residual configurational entropy of the NDC or APC. As the ergodic length scale decreases from greater than the long-range order of the bulk crystal to that of the intermediate range order of the liquid, T_m decreases to $T_{m\ (NDC)}$. Such particle size dependence of the melting point has been studied for β-tin, where T_m begins to decrease for nanocrystals r < 50 nm, to a minimum nearly 100 K below the bulk T_m for r = 3 nm particles[112]. The minimum is presumed to be indicative of the critical length scale for the liquid to exist. APC represents crystal-like organization at or below this critical length scale of a liquid for which $T_{m\ (APC)}$ alternatively can be described as the glass transition, T_g. That the length scale of APC determines glass formation is further born out in a recent report of metallic glass formation in pure iron when particles are less than 15 nm[113].

Quenching perturbations that create the non-ergodic liquid and APC or NDC curves establish two interesting points on this configurational entropy diagram, Figure 5.2. At low temperature there is a point where the configurational entropy of the non-ergodic liquid and the APC or NDC are equivalent, designated T_K' that mirrors the thermodynamic Kauzmann condition[36]. A second point exists where the configurational entropy of the APC or NDC is equivalent to that of the ergodic supercooled liquid. At temperatures above this isentropic point, a quenched non-ergodic liquid will relax to an ergodic liquid, and subsequently crystallize if the isotherm is below T_m. Below this point, APC or NDC will form before the system can relax to a bulk ergodic supercooled liquid. Therefore, we suggest this point defines the glass transition temperature, T_g. The absence of a singularity between the APC or NDC and the ergodic liquid but change in temperature dependent slope of the configurational entropy is consistent with thermodynamic measurements (ΔH or C_p vs. T) that exhibit no singularity

through the glass transition. Notably, if the quench rate is slower than the rate of relaxation but faster than the onset of crystallization, the length scale of "local ergodicity" would be equivalent to the ergodicity the bulk sample, such that T_g and T_K' collapse to T_K; i.e. formation of an ideal glass. The extent to which T_g and T_K' deviate from T_K is governed by the temperature dependence of $\Delta C_p/T$ of liquid and solid phases. But clearly, with increased $f(\Delta T)$ or $f(\Delta v)$ the APC(NDC)/ergodic liquid isentropic point shifts to higher temperature, consistent with the observed time-temperature dependence of T_g[114].

Importantly, the APC only appears as a metastable phase on the energy landscape below the point where the probability of crystal growth becomes greater than the probability of relaxation. Thus the crystallization-relaxation $\Delta G^{\ddagger}$ equivalence point, which identifies the temperature at which the metastable APC does or does not exist, also describes $T_{m\ (APC)}$. As such, TZT_{glass} predicts that the $\Delta G^{\ddagger}$ equivalence point, determined from the experimentally measured rate of crystal growth and viscosity is equivalent to the APC/ergodic liquid isentropic point, and is the material's T_g corresponding to the time-temperature conditions by which the viscosity was measured. In Figure 5.3, the TZT_{glass} calculated value of T_g is plotted against literature reported values for diverse systems for which we have identified temperature dependent crystallization and viscosity data. The literature reference data and TZT parameters are summarized in Appendix Table B.1. There is a high correlation between the calculated and experimental values of T_g, with the largest outliers being disodium silicate, $Na_2Si_2O_5$, and anorthite, $CaAl_2Si_2O_8$, for which a variation in composition between samples used for crystallization and viscosity measurements, respectively, likely accounts for the discrepancy.

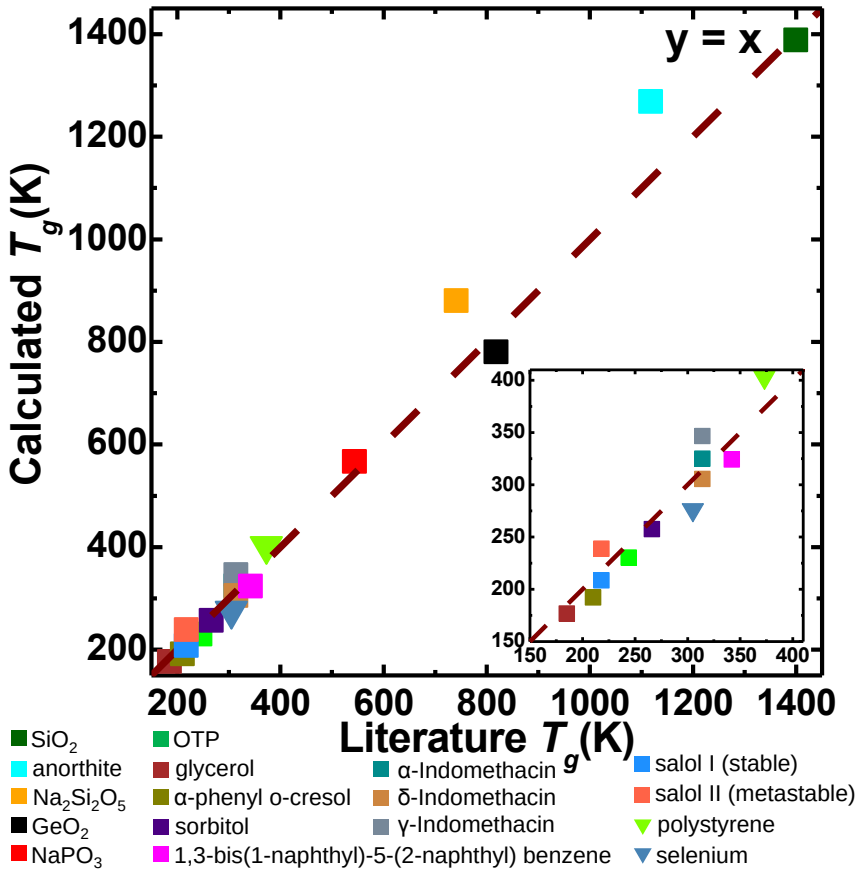

Figure 5.3. TZT_{glass} calculated vs. literature reported experimental T_g. Inset is an enlarged 150 to 400 K portion of the plot. Dashed line is the equivalence line. (Note: crystallization data are reported for three polymorphs of indomethacin and two polymorphs of salol, which are each compared to the viscosity of their single liquid phases.)

Almost all of the T_g values calculated by TZT_{glass} are at slightly lower temperatures than literature reported values. This deviation is likely a result of a time-temperature shift resulting from the difference in the frequency of the measurements used to determine viscosity and T_g[111,115]. Here the reported viscosities used to extract activation parameters were determined based on the rate of melt flow, which becomes very slow (hours to days) as T_g is approached, and thus should exhibit minimal time-temperature shift. By contrast T_g measurements are frequently conducted at higher frequencies (minutes). This results in a time-temperature shift from the materials' intrinsic viscosity, as demonstrated by the shift from the

solid blue to dotted line in Figure 5.1, which results in a higher temperature $\Delta G^{\ddagger}$ equivalence point, and thus higher value for T_g.

5.3. Glass Aging and the Glass-to-Crystal Transition

The above discussion articulates that the glass transition is the APC(NDC)/ergodic liquid isentropic point below which relaxation and crystallization are mutually frustrated. However, practically, glasses form immediately upon quenching, but also evolve with a reduction of free volume upon aging[116]. Aged glasses exhibit enhanced order[117] and exhibit a greater number of nuclei upon cold crystallization[77,79]. The experimental signatures of reduced free volume and enhanced order are also expected for APC, therefore, we propose the rate of APC formation likely describes glass aging. An instantaneously, deeply quenched glass faces a free energy of activation barrier too high for relaxation or crystallization, yielding a non-ergodic glassy state reflective of the configurations of the pre-quenched melt, i.e. the frozen liquid approximation. By contrast, a melt quenched to between T_K' and T_g (or a deeply quenched glass subsequently heated) should exhibit a free energy of activation for APC that is smaller than that of either relaxation or bulk crystallization, thus in time crystal-like organization over the length scale of "local ergodicity" will occur.

Analogous to bulk crystallization[35], the T_g and T_K' points should define the limiting boundaries for $\Delta S_{APC}^{\ddagger}$, where $\Delta S_{APC}^{\ddagger} \rightarrow -\infty$ at T_g, and $\Delta S_{APC}^{\ddagger} \rightarrow 0$ at T_K'. Because the structure of bulk crystals and APC is essentially equivalent on the short- and intermediate-length scale, we assume the physical processes dictating the rate of the progression of phase boundary should be similar for both bulk crystallization and APC formation. Thus to a first approximation, we propose to use the intrinsic activation parameters ΔH_c^*, ΔS_c^* and z_c from

the fit of bulk crystallization to Equation (5.1) to estimate the rate of APC formation. T_g is taken as the crystallization-relaxation $\Delta G^{\ddagger}$ equivalence point. Though actually determined by the temperature dependence of $\Delta C_p/T$ of the non-ergodic liquid and APC phases, based on the schematic of Figure 5.2, T_K' can be approximated by a shift to a temperature lower than T_K by a similar magnitude as T_g was shifted higher than T_K, i.e. $(T_g - T_K) \approx (T_K - T_K')$. With the substitutions of T_K' and T_g for T_K and T_m, we propose Equation (5.1) describes the rate of APC formation; an estimated $\Delta G_{APC}^{\ddagger}$ is plotted as the dashed line in Figure 5.1.

Like the glass transition, the kinetics of glass aging is non-Arrhenius, and models are largely empirical[115,118,119]. Experimental measurements of glass aging indicate that below T_g the rate of aging increases to a maximum within tens of degrees, then slows at lower temperatures to essentially zero at the highest secondary transition, T_β[116]. Calorimetric measurements also demonstrate an enthalpy overshoot at the glass transition with increased aging time[119]. While detailed analysis of glass aging is beyond the scope of this present manuscript, we note the rate of APC formation, as described by TZT_{glass}, correctly predicts the temperature dependent trends in the rate of aging, with a maximal rate slightly below T_g, and the enthalpy overshoot in aged glasses may be a signature of an APC "melting" transition.

It is further interesting to consider the previously reported glass-to-crystal (GC) transition, sometimes described as diffusionless crystallization, observed for a variety of organic glass formers[120-122]. We suggest the observed characteristics of the GC transition resemble an aging-type process described by TZT_{glass}, where the local ergodicity of the quenched melt begins to exhibit long-range order, i.e. NDC. As schematically described in Figure 2, GC (NDC formation) can only occur for a system that has been quenched to below the NDC/ergodic liquid equivalence point, T_g. However, upon heating the glass, NDC remains

a viable intermediate phase above its T_g up to the $T_{m\,(NDC)}$, as observed in several GC forming systems[120-122]. Two of the materials used in this analysis of TZT_{glass}, OTP[120] and Salol[121], are known to exhibit such GC transitions. As shown in Appendix Figure B.2, the temperature dependent rate of GC formation is remarkably fit with the TZT model by taking: the TZT_c activation parameters (ΔH_c^*, ΔS_c^* and z_c) fit to the experimental data for regular crystallization, the maximum temperature for which the primary type of GC is observed as the T_g for the employed time-temperature conditions (255 K for OTP and 226 K for Salol), and T_K' being the only parameter of Equation (5.1) fit to the GC data using non-linear least squares methods (166 K for OTP and 129 K for Salol). As previously suggested[122,123], TZT also implies that the GC phenomenon should only be observed for systems in which there is a high structural similarity between the melt and crystalline phases such that local ergodicity of a quenched melt can extend to length scales characteristic of long-range order.

5.4. The Glass Transition in Non-crystalline Systems.

The above derivation of TZT_{glass} presupposes that at some set of conditions a crystalline phase is thermodynamically favored. Nevertheless, many non-crystalline materials also form glasses. If TZT_{glass} is the relevant theory, it must also account for glass formation of non-crystalline materials. Here we suggest that polystyrene is a useful prototype for consideration. Isotactic and syndiotactic polystyrene, for which the phenyl substituents are ordered along the polymer backbone, are highly crystalline. By contrast, atactic polystyrene, for which phenyl substituents are randomly distributed across the polymer backbone, is non-crystalline. The random organization of the atactic congener essentially makes this system permanently non-ergodic with respect to crystallization. While non-ergodic on the length scale of crystalline

order, it is highly likely the random distribution of substituents will result in small lengths over which the polymer is locally isotactic or syndiotactic. As long as domains exist that are pseudo isotactic or syndiotactic then APC, and thus glass formation should be possible.

Literature data for temperature dependent viscosity of atactic and crystallization rate of isotactic polystyrene are well fit by TZT_{rlx} and TZT_c, respectively (see Appendix Figure B.1q and Figure 2.7a, respectively). As shown in Figure 5.4, the free energies of activation for atactic relaxation and isotactic crystallization never cross, with viscous relaxation of the random polymer being most probable at all temperatures. We note, however, that there is a minimum in the difference between these crystal growth and relaxation curves at 403 K (inset of Figure 5.4), slightly above the reported T_g of atactic polystyrene. Using the minimum in $\Delta(\Delta G^{\ddagger})$ as the value for $T_{m\,APC}$, and selecting T_K' to be shifted to lower temperature by the same magnitude from T_K as $T_{m\,APC}$ was shifted to higher temperature, a $\Delta G_{APC}^{\ddagger}$ can be calculated (dashed line in Figure 5.4). Notably this $\Delta G_{APC}^{\ddagger}$ curve crosses the atactic $\Delta G_{rlx}^{\ddagger}$ curve at 378 K, very close to the literature reported T_g of atactic polystyrene (373K)[124]. Furthermore, while significantly more work is needed to accurately relate TZT_{glass} to the rate of aging, it is notable that a simplistic aging expression, aging = $(k_BT/h)\ exp(-\Delta G_{APC}^{\ddagger}/RT)$, exhibits a maximum at 335 K, consistent with the reported maximum aging shift rate[116], and goes essentially to zero [$log(aging) < -1$] below 285 K, consistent with the 300-310 K temperature range reported for T_β of polystyrene[125].

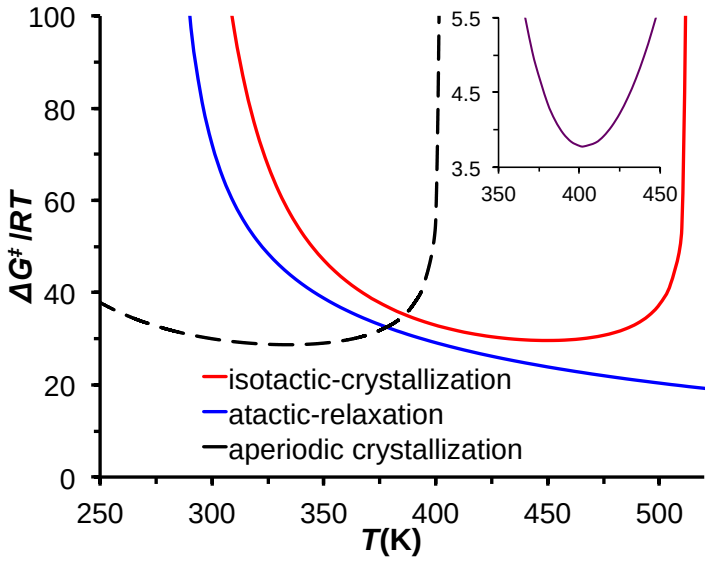

Figure 5.4. RT normalized free energy of activation for a non-crystalline glass forming system. Data are plotted for relaxation of atactic polystyrene (blue) and crystallization of isotactic polystyrene (red). The inset shows $\Delta(\Delta G^{\ddagger})$. The dashed line represents the proposed function for aperiodic crystallization with $T_{m\,APC}$ = 403 K and T_K' = 155 K.

TZT_{glass} thus suggests that glass formation in non-crystalline materials is dependent on the length scale of order possible to the system. In the example of atactic polystyrene, the relaxed polymer can only be described as ergodic when averaging over large domains. At the length scale required for bulk crystallization, covalent linkages prevent the system from ever becoming ergodic. However, ergodicity over a local length scale may allow APC formation, and thus a glass transition at the APC/liquid isentropic point. By contrast, in a system that, for example by random cross-linking, cannot form even locally ergodic domains, no glass transition will be observed.

5.5. Conclusion

Utilizing our recently articulated Transition Zone Theory of crystallization and viscous relaxation, we demonstrate that normally there is a temperature at which the free energy of

activation for relaxation and crystallization are equivalent. Below this temperature, the probability of crystallization is greater than the probability of relaxation. But because the system can only crystallize over the length scale for which the system has relaxed, bulk crystallization cannot occur. However, crystal-like growth without long-range order, described as aperiodic crystallization (APC) that exhibits higher configurational entropy than that of the perfect bulk crystal, is possible. The point at which the configurational entropy of the APC is equivalent to that of the ergodic liquid formally establishes the glass transition temperature. The extent of the configurational entropy difference between bulk crystals and APC is a result of the time-temperature history of the sample, and thus accounts for the sample-history dependent glass transitions. For non-crystalline systems, such as atactic polystyrene, for which there is no crystallization-relaxation $\Delta G^{\ddagger}$ equivalence point, there may still be a length scale over which APC can form, resulting in T_g at the temperature where the free energy of relaxation and APC curves cross. The rate of formation of APC is further correlated to the aging process in glasses.

Historic descriptions of glass formation recognized there exists mutual frustration between the processes of viscous relaxation and crystallization. Transition Zone Theory finally establishes the relationship between these competing processes providing a quantitative description of the glass transition that is based on first principles of thermodynamics and activated processes.

REFERENCES

(1) Anderson, P. W. *Science* **1995**, *267*, 1615.

(2) Galwey, A. K.; Brown, M. E. *P R Soc-Math Phys Sc* **1995**, *450*, 501.

(3) Sestak, J. *J Therm Anal Calorim* **2012**, *110*, 5.

(4) Stillinger, F. H.; Debenedetti, P. G. *Annu Rev Conden Ma P* **2013**, *4*, 263.

(5) Wilson, H. A. *Philos Mag* **1900**, *50*, 238.

(6) Fisher, J. C.; Hollomon, J. H.; Turnbull, D. *J Appl Phys* **1948**, *19*, 775.

(7) Hollomon, J. H.; Turnbull, D. *Prog Met Phys* **1953**, *4*, 333.

(8) Turnbull, D.; Fisher, J. C. *J Chem Phys* **1949**, *17*, 71.

(9) Cahn, J. W. *Acta Metall Mater* **1960**, *8*, 554.

(10) Frenkel, J. *Phys. Z. Sowjetunion* **1932**, *1*, 498.

(11) Turnbull, D.; Cohen, M. H. In *Modern Aspects of the Vitreous State*; MacKenzie, J. D., Ed.; Butterworths: London, 1960, p 38.

(12) Volmer, M.; Marder, M. *Z. Phys. Chem. A* **1931**, *154*, 97.

(13) Dill, E. D.; Josey, A. A.; Folmer, J. C. W.; Hou, F.; Martin, J. D. *Chem Mater* **2013**, *25*, 3932.

(14) Jackson, K.; Uhlmann, D. R.; Hunt, J. *J Cryst Growth* **1967**, *1*, 1.

(15) Howe, J. M. *Philos Mag A* **1996**, *74*, 761.

(16) Zykova-Timan, T.; Ceresoli, D.; Tartaglino, U.; Tosatti, E. *The Journal of chemical physics* **2005**, *123*, 164701.

(17) Debye, P.; Scherrer, P. *Nachrichten von der Gesellschaft der Wissenschaften zu Göttingen, Mathematisch-Physikalische Klasse* **1916**, *1916*, 16.

(18) Martin, J. D.; Goettler, S. J.; Fosse, N.; Iton, L. *Nature* **2002**, *419*, 381.

(19) Salmon, P. S.; Martin, R. A.; Mason, P. E.; Cuello, G. J. *Nature* **2005**, *435*, 75.

(20) Stillinger, F. H.; Weber, T. A. *Science* **1984**, *225*, 983.

(21) Wright, A. C. *Glass Phys Chem+* **1998**, *24*, 148.

(22) An, H. N.; Li, X. Y.; Geng, Y.; Wang, Y. L.; Wang, X.; Li, L. B.; Li, Z. M.; Yang, C. L. *J Phys Chem B* **2008**, *112*, 12256.

(23) Chakrabarty, S.; Karmakar, S.; Dasgupta, C. *Scientific reports* **2015**, *5*.

(24) Angell, C. A. *Science* **1995**, *267*, 1924.

(25) Debenedetti, P. G.; Stillinger, F. H. *Nature* **2001**, *410*, 259.

(26) Shintani, H.; Tanaka, H. *Nat Phys* **2006**, *2*, 200.

(27) Angell, C. A. *J Non-Cryst Solids* **1991**, *131*, 13.

(28) Fulcher, G. S. *J Am Ceram Soc* **1925**, *8*, 339.

(29) Tammann, G.; Hesse, W. *Z Anorg Allg Chem* **1926**, *156*, 245.

(30) Vogel, H. *Phys. Z* **1921**, *22*, 645.

(31) Williams, M. L.; Landel, R. F.; Ferry, J. D. *J Am Chem Soc* **1955**, *77*, 3701.

(32) Schonhals, A.; Kremer, F.; Hofmann, A.; Fischer, E. W. *Physica A* **1993**, *201*, 263.

(33) Stickel, F.; Fischer, E. W.; Richert, R. *J Chem Phys* **1996**, *104*, 2043.

(34) Eyring, H. *J Chem Phys* **1935**, *3*, 107.

(35) Hou, F.; Martin, J. D.; Dill, E. D.; Folmer, J. C.; Josey, A. A. *Chem Mater* **2015**, *27*, 3526.

(36) Kauzmann, W. *Chem Rev* **1948**, *43*, 219.

(37) Kolmogorov, A. N. *Bull. Acad. Sci. USSR, Math. Ser* **1937**, *1*, 355.

(38) Johnson, W. A.; Mehl, R. F. *T Am I Min Met Eng* **1939**, *135*, 416.

(39) Avrami, M. *J Chem Phys* **1939**, *7*, 1103.

(40) Avrami, M. *J. Chem Phys* **1940**, *8*, 212.

(41) Avrami, M. *J Chem Phys* **1941**, *9*, 177.

(42) Dill, E. D.; Folmer, J. C. W.; Martin, J. D. *Chem Mater* **2013**, *25*, 3941.

(43) Martin, J. D.; Greenwood, K. B. *Angewandte Chemie-International Edition in English* **1997**, *36*, 2072.

(44) Urbanovici, E.; Schneider, H. A.; Cantow, H. J. *J Polym Sci Pol Phys* **1997**, *35*, 359.

(45) Kauzmann, W.; Eyring, H. *J Am Chem Soc* **1940**, *62*, 3113.

(46) Kirkpatrick, R. J. *Am Mineral* **1975**, *60*, 798.

(47) Adam, G.; Gibbs, J. H. *J Chem Phys* **1965**, *43*, 139.

(48) Thompson, C. V.; Spaepen, F. *Acta Metall Mater* **1979**, *27*, 1855.

(49) Bleris, G. L.; Karakostas, T.; Stoemenos, J.; Economou, N. A. *Phys Status Solidi A* **1976**, *34*, 243.

(50) Mei, Q.; Benmore, C. J.; Weber, J. K. R. *Phys Rev Lett* **2007**, *98*.

(51) Hodge, I. M. *J Res Natl Inst Stan* **1997**, *102*, 195.

(52) Angell, C. A. *J Res Natl Inst Stan* **1997**, *102*, 171.

(53) Chen, K.; Yao, A. P.; Zheng, E. E.; Lin, J. L.; Zheng, Y. *J Ultras Med* **2012**, *31*, 2001.

(54) Oestreicher, H. L. *J Acoust Soc Am* **1951**, *23*, 707.

(55) Takahara, S.; Yamamuro, O.; Suga, H. *J Non-Cryst Solids* **1994**, *171*, 259.

(56) Fine, R. A.; Millero, F. J. *J Chem Phys* **1973**, *59*, 5529.

(57) Morishige, K.; Kato, T. *J Chem Phys* **1999**, *111*, 7095.

(58) Micoulaut, M.; Cormier, L.; Henderson, G. *Journal of Physics: Condensed Matter* **2006**, *18*, R753.

(59) Pawlus, S.; Paluch, M.; Ziolo, J.; Roland, C. M. *J Phys-Condens Mat* **2009**, *21*.

(60) Chushak, Y.; Hafner, J.; Kahl, G. *Phys Chem Liq* **1995**, *29*, 159.

(61) Brow, R. K. *J Non-Cryst Solids* **2000**, *263*, 1.

(62) Byrd, J. N.; Bartlett, R. J.; Montgomery, J. A. *J Phys Chem A* **2014**, *118*, 1706.

(63) Bacon, R. F.; Fanelli, R. *J Am Chem Soc* **1943**, *65*, 639.

(64) Kozhevnikov, V. F.; Payne, W. B.; Olson, J. K.; McDonald, C. L.; Inglefield, C. E. *J Chem Phys* **2004**, *121*, 7379.

(65) Fairbrother, F.; Gee, G.; Merrall, G. T. *J Polym Sci* **1955**, *16*, 459.

(66) Ruizgarcia, J.; Anderson, E. M.; Greer, S. C. *J Phys Chem-Us* **1989**, *93*, 6980.

(67) Touro, F. J.; Wiewioro.Tk *J Phys Chem-Us* **1966**, *70*, 239.

(68) Powell, R. E.; Eyring, H. *J Am Chem Soc* **1943**, *65*, 648.

(69) Espeau, P.; Ceolin, R. *Thermochim Acta* **2007**, *459*, 127.

(70) Horvath, A. L. *J Chem Educ* **1973**, *50*, 335.

(71) Yu, P.; Wang, W. H.; Wang, R. J.; Lin, S. X.; Liu, X. R.; Hong, S. M.; Bai, H. Y. *Appl Phys Lett* **2009**, *94*.

(72) Zhuravlev, E.; Wurm, A.; Poetschke, P.; Androsch, R.; Schmelzer, J. W. P.; Schick, C. *Eur Polym J* **2014**, *52*, 1.

(73) Androsch, R.; Di Lorenzo, M. L. *Macromolecules* **2013**, *46*, 6048.

(74) De Santis, F.; Pantani, R.; Titomanlio, G. *Thermochim Acta* **2011**, *522*, 128.

(75) Sanchez, M. S.; Mathot, V. B. F.; Poel, G. V.; Ribelles, J. L. G. *Macromolecules* **2007**, *40*, 7989.

(76) Cheng, S. Z. D.; Lotz, B. *Polymer* **2005**, *46*, 8662.

(77) Stolte, I.; Androsch, R.; Di Lorenzo, M. L.; Schick, C. *J Phys Chem B* **2013**, *117*, 15196.

(78) Supaphol, P.; Spruiell, J. E. *Polymer* **2001**, *42*, 699.

(79) Zhuravlev, E.; Schmelzer, J. W. P.; Wunderlich, B.; Schick, C. *Polymer* **2011**, *52*, 1983.

(80) Escleine, J. M.; Monasse, B.; Wey, E.; Haudin, J. M. *Colloid Polym Sci* **1984**, *262*, 366.

(81) Hargis, M. J.; Grady, B. P. *Thermochim Acta* **2006**, *443*, 147.

(82) Korobov, A. *Phys Rev B* **2007**, *76*.

(83) Lorenz, B.; Orgzall, I.; Dässler, R. *International Journal of High Pressure Research* **1991**, *6*, 309.

(84) Pusztai, T.; Granasy, L. *Phys Rev B* **1998**, *57*, 14110.

(85) Shepilov, M. P.; Baik, D. S. *J Non-Cryst Solids* **1994**, *171*, 141.

(86) Kauffman, G. B. F., L. *McGraw-Hill: New York* **1983**, *XXII*, 101.

(87) Dill, E. D.; Folmer, J. C. W.; Martin, J. D. *ZENODO* **2014**, *10.5281/zenodo.12268*.

(88) Hammersley, A.; Svensson, S.; Thompson, A. *Nuclear Instruments and Methods in Physics Research Section A: Accelerators, Spectrometers, Detectors and Associated Equipment* **1994**, *346*, 312.

(89) Hammersley, A. P. *ESRF Internal Report* **1997**, *ESRF97HA02T*.

(90) Savitzky, A.; Golay, M. J. E. *Anal Chem* **1964**, *36*, 1627.

(91) Granasy, L.; Pusztai, T.; Borzsonyi, T.; Warren, J. A.; Douglas, J. F. *Nat Mater* **2004**, *3*, 645.

(92) Josey, A. A. Doctorate thesis, North Carolina State University, 2008.

(93) Collins, C. J.; Bowman, N. S. *Isotope effects in chemical reactions*; Van Nostrand Reinhold: New York,, 1971.

(94) Wayland, B. B.; Ba, S. J.; Sherry, A. E. *Inorg Chem* **1992**, *31*, 148.

(95) Chou, C. H.; Trahanovsky, W. S. *J Am Chem Soc* **1986**, *108*, 4138.

(96) Casey, C. P.; Johnson, J. B. *J Org Chem* **2003**, *68*, 1998.

(97) Heppolette, R.; Robertson, R. E. *J Am Chem Soc* **1961**, *83*, 1834.

(98) Walton, R. I.; O'Hare, D. *J Phys Chem B* **2001**, *105*, 91.

(99) Dutta, P. K.; Puri, M.; Bowers, C. *Acs Sym Ser* **1989**, *398*, 98.

(100) Johari, G. P.; Hallbrucker, A.; Mayer, E. *J Chem Phys* **1990**, *92*, 6742.

(101) Kirichek, O.; Soper, A.; Dzyuba, B.; Callear, S.; Fuller, B. *Plos One* **2015**, *10*.

(102) Martin, J. D. *Inorganic Chemistry in Focus. III* **2006**, 267.

(103) Nordman, C. E.; Lipscomb, W. N. *J Chem Phys* **1951**, *19*, 1422.

(104) Rundle, R. E. *J Chem Phys* **1953**, *21*, 937.

(105) Lubchenko, V.; Wolynes, P. G. *Annu Rev Phys Chem* **2007**, *58*, 235.

(106) Martinez, L. M.; Angell, C. A. *Nature* **2001**, *410*, 663.

(107) Berthier, L.; Biroli, G.; Bouchaud, J. P.; Cipelletti, L.; El Masri, D.; L'Hote, D.; Ladieu, F.; Pierno, M. *Science* **2005**, *310*, 1797.

(108) Hempel, E.; Hempel, G.; Hensel, A.; Schick, C.; Donth, E. *J Phys Chem B* **2000**, *104*, 2460.

(109) Qiu, X. H.; Ediger, M. D. *J Phys Chem B* **2003**, *107*, 459.

(110) Tracht, U.; Wilhelm, M.; Heuer, A.; Feng, H.; Schmidt-Rohr, K.; Spiess, H. W. *Phys Rev Lett* **1998**, *81*, 2727.

(111) Olsen, N. B.; Christensen, T.; Dyre, J. C. *Phys Rev Lett* **2001**, *86*, 1271.

(112) Wronski, C. R. M. *Brit J Appl Phys* **1967**, *18*, 1731.

(113) Greer, A. L. *Nat Mater* **2015**, *14*, 542.

(114) Moynihan, C. T.; Easteal, A. J.; Wilder, J.; Tucker, J. *J Phys Chem-Us* **1974**, *78*, 2673.

(115) Li, R. Z. *Mat Sci Eng a-Struct* **2000**, *278*, 36.

(116) Struik, L. C. E. *Physical aging in amorphous polymers and other materials*; Elsevier Scientific Pub. Co. ; distributors for the U.S. and Canada, Elsevier North-Holland: Amsterdam ; New York, New York, 1978.

(117) Song, H. H.; Roe, R. J. *Macromolecules* **1987**, *20*, 2723.

(118) Debolt, M. A.; Easteal, A. J.; Macedo, P. B.; Moynihan, C. T. *J Am Ceram Soc* **1976**, *59*, 16.

(119) Williams, G.; Watts, D. C. *T Faraday Soc* **1970**, *66*, 80.

(120) Hikima, T.; Adachi, Y.; Hanaya, M.; Oguni, M. *Phys Rev B* **1995**, *52*, 3900.

(121) Konishi, T.; Tanaka, H. *Phys Rev B* **2007**, *76*.

(122) Sun, Y.; Xi, H. M.; Chen, S.; Ediger, M. D.; Yu, L. *J Phys Chem B* **2008**, *112*, 5594.

(123) Hatase, M.; Hanaya, M.; Oguni, M. *J Non-Cryst Solids* **2004**, *333*, 129.

(124) Fox, T. G.; Flory, P. J. *J Appl Phys* **1950**, *21*, 581.

(125) Miwa, Y.; Urakawa, O.; Doi, A.; Yamamoto, K.; Nobukawa, S. *J Phys Chem B* **2012**, *116*, 1282.

(126) Zhou, D. L.; Zhang, G. G. Z.; Law, D.; Grant, D. J. W.; Schmitt, E. A. *J Pharm Sci-Us* **2002**, *91*, 1863.

(127) Doremus, R. H. *J Appl Phys* **2002**, *92*, 7619.

(128) Melosh, H. J. *Meteorit Planet Sci* **2007**, *42*, 2079.

(129) Nascimento, M. L. F.; Aparicio, C. *Physica B* **2007**, *398*, 71.

(130) Polian, A.; Vo-Thanh, D.; Richet, P. *Europhys Lett* **2002**, *57*, 375.

(131) Wagstaff, F. E. *J Am Ceram Soc* **1969**, *52*, 650.

(132) Wright, A. F.; Leadbetter, A. J. *Philos Mag* **1975**, *31*, 1391.

(133) Avramov, I.; Zanotto, E. D.; Prado, M. O. *J Non-Cryst Solids* **2003**, *320*, 9.

(134) *Physical properties of glycerine and its solutions*; Glycerine Producers' Association, 1963.

(135) Haynes, W. M.; Bruno, T. J.; Lide, D. R. In *CRC handbook of chemistry and physics*; CRC Press: 2014, p 47.

(136) Van Koningsveld, H. *Recueil des Travaux Chimiques des Pays-Bas* **1968**, *87*, 243.

(137) Privalko, V. P. *J Phys Chem-Us* **1980**, *84*, 3307.

(138) Bryan, J. C.; Delmau, L. H.; Hay, B. P.; Nicholas, J. B.; Rogers, L. M.; Rogers, R. D.; Moyer, B. A. *Struct Chem* **1999**, *10*, 187.

(139) Cukierma.M; Lane, J. W.; Uhlmann, D. R. *J Chem Phys* **1973**, *59*, 3639.

(140) Cunha, D. L.; Coutinho, J. A. P.; Daridon, J. L.; Reis, R. A.; Paredes, M. L. L. *J Chem Eng Data* **2013**, *58*, 2925.

(141) Laughlin, W. T.; Uhlmann, D. R. *J Phys Chem-Us* **1972**, *76*, 2317.

(142) Murthy, S. S. N.; Paikaray, A.; Arya, N. *J Chem Phys* **1995**, *102*, 8213.

(143) Scherer, G.; Uhlmann, D. R. *J Cryst Growth* **1972**, *15*, 1.

(144) Higashigaki, Y.; Wang, C. H. *J Chem Phys* **1981**, *74*, 3175.

(145) Scherer, G.; Uhlmann, D. R.; Miller, C. E.; Jackson, K. A. *J Cryst Growth* **1974**, *23*, 323.

(146) Tolle, A. *Rep Prog Phys* **2001**, *64*, 1473.

(147) Avramov, I.; Gutzow, I.; Grantscharova, E. *J Cryst Growth* **1988**, *87*, 305.

(148) GUTZOW, I. *Phosphorus Research Bulletin* **1996**, *6*, 107.

(149) Immirzi, A.; Porzio, W. *Acta Crystallogr B* **1982**, *38*, 2788.

(150) Pawlak, Z.; Yarlagadda, P.; Frost, R.; Hargreaves, D. *Journal of Achievements in Materials and Manufacturing Engineering* **2009**, *37*, 458.

(151) Ophir, J.; Mcwhirt, R. E.; Maklad, N. F. *Ultrasonic Imaging* **1979**, *1*, 265.

(152) Rault, J. *J Non-Cryst Solids* **2000**, *271*, 177.

(153) Wu, T.; Yu, L. *J Phys Chem B* **2006**, *110*, 15694.

(154) Yu, L. A. *Cryst Growth Des* **2003**, *3*, 967.

(155) Andronis, V.; Zografi, G. *Pharmaceut Res* **1997**, *14*, 410.

(156) Fakhraai, Z.; Still, T.; Fytas, G.; Ediger, M. D. *J Phys Chem Lett* **2011**, *2*, 423.

(157) Hancock, B. C.; Dupuis, Y.; Thibert, R. *Pharmaceut Res* **1999**, *16*, 672.

(158) Farber, D. L.; Williams, Q. *Am Mineral* **1996**, *81*, 273.

(159) Kahlenberg, V.; Rakic, S.; Weidenthaler, C. *Z Kristallogr* **2003**, *218*, 421.

(160) Meiling, G. S.; Uhlmann, D. R. *Phys Chem Glasses* **1967**, *8*, 62.

(161) Meyer, A.; Schober, H.; Dingwell, D. B. *Europhys Lett* **2002**, *59*, 708.

(162) Li, Z. L.; Sun, W. H.; Jin, X. L.; Shao, C. X. *Synlett* **2001**, 1947.

(163) Magill, J. H.; Plazek, D. J. *J Chem Phys* **1967**, *46*, 3757.

(164) Plazek, D. J.; Magill, J. H. *J Chem Phys* **1968**, *49*, 3678.

(165) Dingwell, D. B.; Knoche, R.; Webb, S. L. *Phys Chem Miner* **1993**, *19*, 445.

(166) Haines, J.; Cambon, O.; Philippot, E.; Chapon, L.; Hull, S. *J Solid State Chem* **2002**, *166*, 434.

(167) Kurkjian, C.; Douglas, R. *Phys. Chem. Glasses* **1960**, *1*, 19.

(168) Vergano, P. J. Doctorate Thesis, Massachusetts Institute of Technology, 1969.

(169) Bohmer, R.; Ngai, K. L.; Angell, C. A.; Plazek, D. J. *J Chem Phys* **1993**, *99*, 4201.

(170) Ai, Y. H.; Lange, R. A. *J Geophys Res-Sol Ea* **2008**, *113*.

(171) Cranmer, D.; Salomaa, R.; Yinnon, H.; Uhlmann, D. R. *J Non-Cryst Solids* **1981**, *45*, 127.

(172) Cukierma.M; Uhlmann, D. R. *J Geophys Res* **1973**, *78*, 4920.

(173) Kempster, C. J.; Radoslovich, E. W.; Megaw, H. D. *Acta Crystallogr* **1962**, *15*, 1005.

(174) Kirkpatrick, R. J.; Robinson, G. R.; Hays, J. F. *J Geophys Res* **1976**, *81*, 5715.

(175) Klein, L.; Uhlmann, D. R. *J Geophys Res* **1974**, *79*, 4869.

(176) Scarfe, C. M.; Cronin, D. J.; Wenzel, J. T.; Kauffman, D. A. *Am Mineral* **1983**, *68*, 1083.

(177) Taniguchi, H. *Contrib Mineral Petr* **1992**, *109*, 295.

(178) Bilgram, J. H.; Durig, U.; Wachter, M.; Seiler, P. *J Cryst Growth* **1982**, *57*, 1.

(179) Sabirov, L. M.; Starunov, V. S.; Fabelins.Il *Sov Phys Jetp-Ussr* **1971**, *33*, 82.

(180) Sidebottom, D. L.; Sorensen, C. M. *Phys Rev B* **1989**, *40*, 461.

(181) Taborek, P.; Kleiman, R. N.; Bishop, D. J. *Phys Rev B* **1986**, *34*, 1835.

(182) Hammond, R. B.; Jones, M. J.; Roberts, K. J.; Kutzke, H.; Klapper, H. *Z Kristallogr* **2002**, *217*, 484.

(183) Campbell, A. N.; Epstein, S. *J Am Chem Soc* **1942**, *64*, 2679.

(184) Cherin, P.; Unger, P. *Inorg Chem* **1967**, *6*, 1589.

(185) Crystal, R. G. *Journal of Polymer Science Part A-2: Polymer Physics* **1970**, *8*, 2153.

(186) Kostal, P.; Malek, J. *J Non-Cryst Solids* **2010**, *356*, 2803.

(187) Kozhevnikov, V. F.; Payne, W. B.; Olson, J. K.; Allen, A.; Taylor, P. C. *J Non-Cryst Solids* **2007**, *353*, 3254.

(188) Privalko, V. P. *Polymer* **1978**, *19*, 1019.

(189) Boon, J.; Challa, G.; Vankreve.Dw *J Polym Sci A2* **1968**, *6*, 1791.

(190) Karasz, F. E.; Bair, H. E.; Oreilly, J. M. *J Phys Chem-Us* **1965**, *69*, 2657.

(191) Kono, R. *J Phys Soc Jpn* **1960**, *15*, 718.

(192) Natta, G.; Corradini, P.; Bassi, I. *Il Nuovo Cimento (1955-1965)* **1960**, *15*, 68.

(193) Spencer, R. S.; Dillon, R. E. *J Coll Sci Imp U Tok* **1949**, *4*, 241.

(194) Arimoto, H.; Ishibash.M; Hirai, M.; Chatani, Y. *J Polym Sci Part A* **1965**, *3*, 317.

(195) Magill, J. *Polymer* **1965**, *6*, 367.

(196) Brandrup, J.; Immergut, E. H.; McDowell, W. *Polymer handbook*; 2d ed.; Wiley: New York,, 1975.

(197) Dorset, D. L.; McCourt, M. P. *Polymer* **1997**, *38*, 1985.

(198) Angell, C. A.; Smith, D. L. *J Phys Chem-Us* **1982**, *86*, 3845.

(199) Xiang, H. W.; Laesecke, A.; Huber, M. L. *J Phys Chem Ref Data* **2006**, *35*, 1597.

(200) Angell, C. A.; Rao, K. J. *J Chem Phys* **1972**, *57*, 470.

(201) Naziev, Y. M.; Shakhverdiev, A. N.; Abdullaev, T. S.; Mekhtieva, G. R. *J Appl Chem-Ussr* **1991**, *64*, 1443.

(202) Wohlfarth, C. In *Landolt-Börnstein: Numerical Data and Functional Relationships in Science and Technology. Physical Chemistry.*; Springer: New York, 2009, p 1 online resource.

(203) Hassaine, M. Doctorate Thesis, Universidad Autónoma de Madrid, 2013.

(204) Ribeiro, A. F.; Langa, E.; Mainar, A. M.; Pardo, J. I.; Urieta, J. S. *J Chem Eng Data* **2006**, *51*, 1846.

(205) Al-Jimaz, A. S.; Al-Kandary, J. A.; Abdul-Latif, A. H. M. *Fluid Phase Equilibr* **2004**, *218*, 247.

(206) Al-Kandary, J.; Al-Jimaz, A. S.; Abdul-Latif, A. M. *Phys Chem Liq* **2009**, *47*, 210.

(207) Audonnet, F.; Padua, A. A. H. *Int J Thermophys* **2002**, *23*, 1537.

(208) Domańska, U.; Żołek-Tryznowska, Z. *The Journal of Chemical Thermodynamics* **2010**, *42*, 651.

(209) Saleh, M. A.; Akhtar, S.; Begum, S.; Ahmed, M. S.; Begum, S. K. *Phys Chem Liq* **2004**, *42*, 615.

(210) Domanska, U.; Krolikowska, M. *J Chem Eng Data* **2010**, *55*, 2994.

(211) Rauf, M. A.; Stewart, G. H.; Farhataziz *J Chem Eng Data* **1983**, *28*, 324.

(212) Matsuo, S.; Makita, T. *Int J Thermophys* **1989**, *10*, 833.

(213) Swamy, K. M.; Narayana, K. L. *J Chem Eng Data* **1993**, *38*, 617.

(214) Rossini, F. D.; American Petroleum Institute. *Selected values of physical and thermodynamic properties of hydrocarbons and related compounds, comprising the tables of the American Petroleum Institute Research Project 44 extant as of December 31, 1952*; Published for the American Petroleum Institute by Carnegie Press: Pittsburgh,, 1953.

(215) Younglove, B. A.; Ely, J. F. *J Phys Chem Ref Data* **1987**, *16*, 577.

(216) Lewis, O. G. *J Chem Phys* **1965**, *43*, 2693.

(217) Chavez, M.; Palacios, J. M.; Tsumura, R. *J Chem Eng Data* **1982**, *27*, 350.

(218) Ball, S. J.; Trusler, J. P. M. *Int J Thermophys* **2001**, *22*, 427.

(219) Hasanov, V. H. *High Temp+* **2012**, *50*, 44.

(220) Aminabhavi, T. M.; Patil, V. B. *J Chem Eng Data* **1997**, *42*, 641.

(221) Landaverde-Cortes, D. C.; Iglesias-Silva, G. A.; Ramos-Estrada, M.; Hall, K. R. *J Chem Eng Data* **2008**, *53*, 288.

(222) Banipal, T. S.; Garg, S. K.; Ahluwalia, J. C. *J Chem Thermodyn* **1991**, *23*, 923.

(223) Khasanshin, T.; Samuilov, V.; Shchemelev, A. *Journal of Engineering Physics and Thermophysics* **2008**, *81*, 760.

(224) Junquera, E.; Aicart, E.; Tardajos, G. *J Chem Thermodyn* **1989**, *21*, 1223.

(225) Aminabhavi, T. M.; Patil, V. B. *Journal of Chemical & Engineering Data* **1997**, *42*, 641.

(226) Khasanshin, T. S.; Shchamialiou, A. P. *High Temp-High Press* **2000**, *32*, 663.

(227) Yucel, H. G.; Uysal, A. In *17th European Conference on Thermophysical Properties Collection of Manuscripts* 2005.

(228) Aminabhavi, T. M.; Gopalkrishna, B. *J Chem Eng Data* **1994**, *39*, 529.

(229) Garcia, B.; Alcalde, R.; Aparicio, S.; Leal, J. M. *Ind Eng Chem Res* **2002**, *41*, 4399.

(230) Knapstad, B.; Skjolsvik, P. A.; Oye, H. A. *J Chem Eng Data* **1989**, *34*, 37.

(231) Dovnar, D. V.; Lebedinskii, Y. A.; Khasanshin, T. S.; Shchemelev, A. P. *High Temp* **2001**, *39*, 835.

(232) Outcalt, S.; Laesecke, A.; Fortin, T. J. *J Chem Thermodyn* **2010**, *42*, 700.

(233) Daridon, J. L.; Carrier, H.; Lagourette, B. *Int J Thermophys* **2002**, *23*, 697.

(234) Dutour, S.; Daridon, J. L.; Lagourette, B. *Int J Thermophys* **2000**, *21*, 173.

(235) De Podesta, M. *Understanding the properties of matter*; 2nd ed.; Taylor & Francis: London ; New York, 2001.

(236) Yaws, C. L. *Chem Eng-New York* **2007**, *114*, 44.

(237) Chiong, Y. S. *Proc R Soc Lon Ser-A* **1936**, *157*, 0264.

(238) Grosse, A. V. *Science* **1965**, *147*, 1438.

(239) Assael, M. J.; Kalyva, A. E.; Antoniadis, K. D.; Banish, R. M.; Egry, I.; Wu, J. T.; Kaschnitz, E.; Wakeham, W. A. *J Phys Chem Ref Data* **2010**, *39*.

(240) Gordon, R. *Acta Metall Mater* **1959**, *7*, 1.

(241) Ternovoi, V. Y.; Filimonov, A. S.; Fortov, V. E.; Lomonosov, I. V.; Nikolaev, D. N.; Pyalling, A. A. *Aip Conf Proc* **1998**, *429*, 87.

(242) Belashchenko, D. K.; Zhuravlev, Y. V. *Inorg Mater+* **2008**, *44*, 939.

(243) Assael, M. J.; Kakosimos, K.; Banish, R. M.; Brillo, J.; Egry, I.; Brooks, R.; Quested, P. N.; Mills, K. C.; Nagashima, A.; Sato, Y.; Wakeham, W. A. *J Phys Chem Ref Data* **2006**, *35*, 285.

(244) Nasch, P. M.; Manghnani, M. H.; Secco, R. A. *J Geophys Res-Sol Ea* **1994**, *99*, 4285.

(245) Assael, M. J.; Armyra, I. J.; Brillo, J.; Stankus, S. V.; Wu, J. T.; Wakeham, W. A. *J Phys Chem Ref Data* **2012**, *41*.

(246) Hess, H.; Kaschnitz, E.; Pottlacher, G. *International Journal of High Pressure Research* **1994**, *12*, 29.

(247) Scopigno, T.; Balucani, U.; Ruocco, G.; Sette, F. *Phys Rev Lett* **2000**, *85*, 4076.

(248) Gering, K.; Sauerwald, F. *Z Anorg Allg Chem* **1935**, *223*, 204.

(249) Bryk, T.; Wax, J. F. *J Chem Phys* **2010**, *132*.

(250) Cahill, J.; Grosse, A. *The Journal of Physical Chemistry* **1965**, *69*, 518.

(251) Spells, K. E. *P Phys Soc* **1936**, *48*, 299.

(252) Kunnen, J. *Rheol Acta* **1988**, *27*, 575.

(253) Almond, D. P.; Blairs, S. *J Phys E Sci Instrum* **1980**, *13*, 964.

(254) Turdukozhaeva, A. M. *Russ J Phys Chem a+* **2013**, *87*, 1595.

(255) Grosse, A. V. *J Phys Chem-Us* **1964**, *68*, 3419.

(256) Haynes, W. M.; Bruno, T. J.; Lide, D. R. In *CRC handbook of chemistry and physics*; CRC Press: 2014, p 122.

(257) Hallett, J. *P Phys Soc Lond* **1963**, *82*, 1046.

(258) Kestin, J.; Sokolov, M.; Wakeham, W. A. *J Phys Chem Ref Data* **1978**, *7*, 941.

(259) Korson, L.; Drosthan.W; Millero, F. J. *J Phys Chem-Us* **1969**, *73*, 34.

(260) Faranda, S.; Foca, G.; Marchetti, A.; Tassi, L.; Ulrici, A.; Zucchi, C. *J Solution Chem* **2004**, *33*, 1181.

(261) Outcalt, S. L.; Laesecke, A.; Fortin, T. J. *J Mol Liq* **2010**, *151*, 50.

(262) CAMEO Chemicals, NOAA. Data Page for Cyclohexanol. http://cameochemicals.noaa.gov/chris/CHN.pdf (1999).

(263) Reddy, K. R.; Kumar, D. B. K.; Rao, G. S.; Anila, P.; Rambabu, C. *Thermochim Acta* **2014**, *590*, 116.

(264) Kinart, C. M.; Miecznik, P.; Klimczak, M. *J Mol Liq* **2009**, *149*, 81.

(265) Lunkenheimer, P.; Kastner, S.; Kohler, M.; Loidl, A. *Phys Rev E* **2010**, *81*.

(266) Tsierkezos, N. G.; Palaiologou, M. M. *Phys Chem Liq* **2009**, *47*, 447.

(267) Aralaguppi, M. I.; Jadar, C. V.; Aminabhavi, T. M. *J Chem Eng Data* **1999**, *44*, 446.

(268) Heiks, J. R.; Orban, E. *J Phys Chem-Us* **1956**, *60*, 1025.

(269) Hernandez-Galvan, M. A.; Garcia-Sanchez, F.; Macias-Salinas, R. *Fluid Phase Equilibr* **2007**, *262*, 51.

(270) Raman, C. V. *Nature* **1923**, *111*, 600.

(271) Santos, F. J. V.; de Castro, C. A. N.; Dymond, J. H.; Dalaouti, N. K.; Assael, M. J.; Nagashima, A. *J Phys Chem Ref Data* **2006**, *35*, 1.

(272) Luning Prak, D. J.; Cowart, J. S.; McDaniel, A. M.; Trulove, P. C. *Journal of Chemical & Engineering Data* **2014**.

(273) Speedy, R. J. *Biophys Chem* **2003**, *105*, 411.

(274) Oswal, S. L.; Gardas, R. L.; Phalak, R. P. *J Mol Liq* **2005**, *116*, 109.

(275) Rathnam, M. V.; Jain, K.; Kumar, M. S. S. *J Chem Eng Data* **2010**, *55*, 1722.

(276) Kumar, M.; Rattan, V. *Journal of Thermodynamics* **2013**, *2013*.

(277) Kondrin, M. V.; Gromnitskaya, E. L.; Pronin, A. A.; Lyapin, A. G.; Brazhkin, V. V.; Volkov, A. A. *J Chem Phys* **2012**, *137*.

(278) Wilson, G. M.; VonNiederhausern, D. M.; Giles, N. F. *J Chem Eng Data* **2002**, *47*, 761.

(279) Sarkar, B. K.; Choudhury, A.; Sinha, B. *J Solution Chem* **2012**, *41*, 53.

(280) Gonzalez, B.; Dominguez, A.; Tojo, J. *J Chem Eng Data* **2004**, *49*, 1590.

(281) Greiner-Schmid, A.; Has, M.; Lüdemann, H.-D. *Zeitschrift für Naturforschung. A, A Journal of physical sciences* **1990**, *45*, 1281.

(282) Niepmann, R.; Schmidt, U. *J Chem Thermodyn* **1980**, *12*, 1133.

APPENDICES

Appendix A

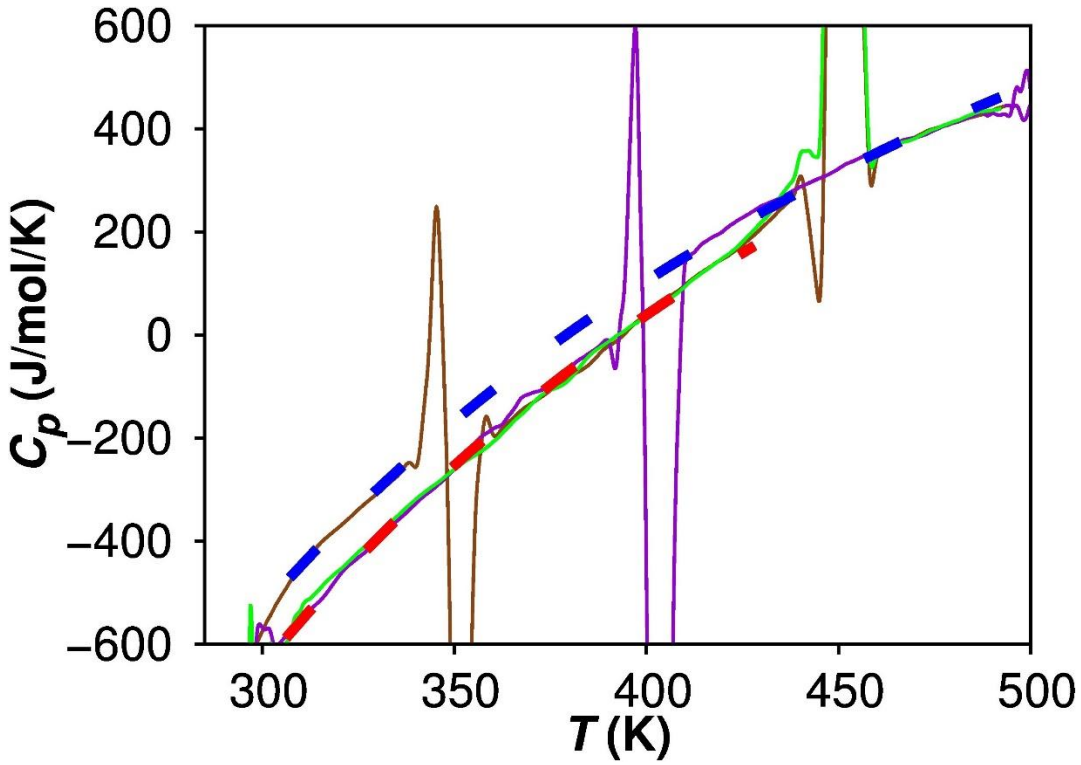

Figure A.1. Data and method for measurement of T_K for CZX-1. Shown in the figure are the heat capacities (C_p) of the liquid CZX-1 supercooled from above the melting point (purple) and heated from the glass (brown), and of the crystal CZX-1 heated through the melt (green), measured by temperature-modulated DSC (TMDSC).

In a sealed fused silica capilary, a glass sample (melted at 250 °C and quenched in liquid N_2) was heated and cooled at a rate of 5 °/min with a modulation of ± 0.5°C/min through the temperature range -20 °C → 250 °C → dwell 5 min → 25 °C → 250 °C. The temperature dependence of the C_p of both liquid and crystalline phases was fit to a reciprocal function of temperature[126] to extrapolate beyond the measured temperature ranges, and the fitted C_p of the liquid phase and that of the solid phase are represented by blue and red dashed line, respectively. The negative values are due to the instrumental baseline being shifted off zero.

The temperature dependence of $\Delta C_p = C_p$ (liquid) – C_p (solid) were calculated from the fitted lines.

The entropy difference between the liquid and the solid at temperature T' can be expressed as[48]:

$$\Delta S = \frac{\Delta H_m}{T_m} - \int_{T'}^{T_m} \frac{\Delta C_p}{T} dT \qquad \text{(A.1)}$$

where ΔH_m is the enthalpy of melting, measured by integration of the melting peak from the standard DSC. When $T' = T_K$,

$$\Delta S = \frac{\Delta H_m}{T_m} - \int_{T_K}^{T_m} \frac{\Delta C_p}{T} dT = 0 \qquad \text{(A.2)}$$

For CZX-1, T_K = 150 K was determined using Equation (A.2) and it is the average of ten TMDSC measurements.

Appendix B

Table B.1. Composite tabulation of material data, TZT_c parameters for all the crystalline materials, TZT_{rlx} parameters for those materials that also had viscosity data available, and the literature reported T_g and calculated T_g as plotted in Figure 5.3.

				crystallization[c]				viscosity[c]						
Material	T_c (K)[b]	T_m (K)	T_K (K)[b]	Averaged lattice constant (Å)	ΔH_c* (kJ/mol)	ΔS_c* (J/mol)	z_c	$v^2\rho$ (GPa)	ΔH_{rlx}* (kJ/mol)	ΔS_{rlx}* (J/mol)	z_{rlx}	Literature T_g (K)	Calculated T_g (K)	References
SiO_2	5400[a]	2007	139(351.60)	7.1487	240(32)	-95(22)	0.038(12)	47.05	322(3)	-0.03(8)	4(1)	1399	1388.41	127–133
glycerol	850	291	134	7.5975	14.4(2)	-56(2)	0.196(7)	4.35	2(2)	-20(4)	1.03(3)	185	176.70	12,27,134–137
α-phenyl o-cresol[d]	(751.02)	324.5	181.2	12.662	9.79(14)	-69(2)	0.182(8)	2.11	3(2)	-9(5)	1.08(8)	210	192.18	138–143
OTP	857	331	200	10.950	14.7(2)	-11(2)	0.66(4)	3.72	3(1)	-4(2)	1.47(13)	244	230.38	27,51,139, 144–146
$NaPO_3$[e]	(4273.52)	898	466(128.41, 487.40)[f]	10.104	80(2)	-49(4)	0.207(14)	29.75	17.8(2)	-73(16)	-0.47(12)	544	567.02	133,147–150
Sorbitol	(814.67)	368	229(196.01)	13.450	21.1(5)	-40(6)	0.27(6)	2.66	14.0(4)	-1.5(4)	2.10(12)	266	257.59	51,151–154
α-indomethacin		426	256(256.81)	13.576	16.2(5)	-67(5)	0.13(2)					314	324.89	153,155
γ-indomethacin	(1158.73)	433	256(229.22)	9.5394	26.2(4)	-26(3)	0.36(4)	1.20	6(12)	-5(10)	1.6(6)	314	346.64	153,155–157
δ-indomethacin		400	256(259.46)	11.558[g]	15.0(4)	-70(5)	0.12(2)					314	305.55	153,155
$Na_2O.2SiO_2$	(5599.98)	1148	381(458.02)	10.036	77.5(7)	-55(1)	0.163(4)	20.00	44(17)	-33(2)	0.4(2)	741	880.60	133,158–161
1,3-bis(1-naphthyl)-5-(2-naphthyl) benzene	(1055.11)	472	200(209.41)	13.487	43.7(2)	-2.3(5)	0.88(5)	3.72[h]	6(2)	-8(2)	2.00(13)	342	324.25	137,162–164
GeO_2	(2419.62)	1388	(290.28)	5.0062	133(6)	-74(8)	0.092(12)	8.08	85(4)	-106(4)	0.390(8)	818	780.59	165–169
anorthite	(6364.71)	1825	815	11.025	68.6(9)	-66(2)	0.178(5)	20.1	24(74)	-19(19)	0.888(14)	1118	1268.26	51,170–177

salol I (stable)	(726.85)	315	167	12.800	16.30(11)	-14(1)	0.48(2)	1.58	4.5(9)	-4(2)	1.69(13)	218	208.59	51,121,139,141,178–181
salol II (metastable)		302	167(183.90)	10.170	10.8(3)	-52(5)	0.16(2)					218	238.88	51,121,182
selenium	1757	492	215	4.3406	28(1)	-55(8)	0.56(8)	0.405	25.2(5)	-0.001(6)	3(1)	305	276.12	69,137,183–188
polystyrene[i]	(1039.37)	513	279	14.031	23.7(3)	-76(2)	0.350(11)	0.225	2(9)	-109(18)	0.44(11)	373	402.76	124,189–193
nylon 6		500	255	8.6414	13.3(4)	-86(3)	0.32(2)							188,194, 195
poly(propyl-ene oxide)		348	162	7.0591	9.6(9)	-96(8)	0.28(2)							188,196
poly(ethylene succinate)		381	190	9.3381	17.5(3)	-51(3)	0.51(2)							188,196
nylon 66		545	210	6.6466	12(1)	-105(7)	0.21(2)							188,196
poly(ethylene adipate)		343	175	7.5188	16(1)	-58(12)	0.41(6)							188,196
poly(ethylene terephthalate)		557	228	6.0434	35.2(6)	-32(3)	0.87(5)							188,196
poly(tetra-methyl-p-silphenyl siloxane)		423	180	10.788	15.6(3)	-78(3)	0.36(1)							188,196, 197

Table B.2. Composite tabulation of material data and TZT_{rlx} parameters for materials that only had viscosity data available.

material				viscosity			references
	T_c	T_m	T_K	H_{rlx}*	S_{rlx}*	z_{rlx}	
methanol	513	175	64	3.88(2)	-14.98(12)	0.168(2)	135,198, 199
ethanol	514	159.15	71	2.30(8)	-26.8(4)	0.350(4)	33,135, 200
n-propanol	536.8	147.15	73(77)	6.9(2)	-8.3(9)	0.08(12)	33,135, 200
n-butanol	562	188	80	4.3(3)	-20(1)	0.507(6)	201–203
n-pentanol	580	195	(102.74)	7(1)	-6(5)	0.43(11)	202,204
n-hexanol	610.5	226	(100.02)	4(1)	-19(6)	0.538(14)	205–209
n-heptanol	633	238.25	(102.22)	7(6)	-6(21)	0.7(3)	205,206, 209–211
n-octanol	655	257	(105.05)	5(4)	-16(13)	0.69(6)	205,206, 208–212
n-nonanol	672	267	(107.40)	8(5)	-5(19)	0.8(4)	205,206,209–211
n-decanol	690	279.6	(110.97)	5(5)	-14(19)	0.73(10)	205,206, 209–212
n-undecanol	704	288.45	(113.07)	8(12)	-5(39)	1(1)	202,209, 213
n-dodecanol	719.4	297	(116.01)	6(4)	-14(13)	0.70(4)	209,212, 213
methane	190.6	85.7	44.9(64.20)	0.110(7)	-8.49(8)	0.127(13)	214–216
ethane	305.3	101	25.8(67.38)	0.162(6)	-10.87(5)	0.218(4)	214–216
propane	369.9	85.5	28.4(39.77)	1.45(12)	-8.93(7)	0.028(9)	214–216
n-butane	425	136	-12.9(65.25)	0.85(4)	-16.9(2)	0.153(6)	214–216
n-pentane	469.8	143.4	54.5(55.06)	2.25(8)	-14.5(4)	0.02(2)	214,216, 217
n-hexane	507.6	178	58.9(96.25)	1.403(7)	-21.3(4)	0.0642(13)	214,216, 218
n-heptane	540	182.6	71.3(86.17)	2.50(5)	-17.7(2)	0.031(9)	202,214, 216,219
n-octane	568.9	216.15	69.6(112.95)	1.98(5)	-19.8(2)	0.067(8)	202,214, 216,219
n-nonane	595	219.5	81.2(118.57)	2.215(13)	-19.60(6)	0.075(2)	214,216, 220,221
n-decane	617.8	243.3	79.4(125.18)	2.50(6)	-22.8(2)	0.051(6)	202,214, 216,222, 223
n-undecane	639	247.4	85.4(143.24)	1.951(6)	-21.17(2)	0.1114(7)	214,216, 224
n-dodecane	658.2	263.5	84.9(136.15)	2.67(8)	-21.2(3)	0.077(9)	202,214, 216,225

n-tridecane	676	268	88.1(164.32)	1.72(2)	-24.60(9)	0.120(2)	214,216, 226,227
n-tetradecane	693	278.7	88.2(168.80)	1.79(3)	-23.17(10)	0.130(2)	214,216, 228-230
n-pentadecane	708	283	91.8(167.44)	2.090(8)	-26.04(3)	0.1085(7)	214,216, 227,231
n-hexadecane	722	291	91.7(169.49)	2.223(6)	-22.68(3)	0.1229(6)	214,216, 232
n-heptadecane	734	295.1	96.9(169.90)	2.430(7)	-24.19(3)	0.1098(5)	214,216, 233
n-octadecane	747	301	96.4(175.17)	2.40(2)	-24.78(8)	0.111(2)	214,216, 234
n-nonadecane	755	304	101.6(179.61)	2.41(2)	-25.03(8)	0.111(1)	214,216, 234
n-eicosane[j]	768	310	103.1(180.94)	2.53(2)	-25.18(6)	0.1090(12)	214,216
potassium	2223[a]	336.65	-6.5(118.57)	1.2(2)	-19.7(2)	-0.045(15)	69,235–238
sodium	2573[a]	370.944	-55(135.96)	1.95(5)	-16.83(5)	-0.146(7)	69,235–238
tin	5809[a]	505.08	(94.12)	2.82(5)	-19.8(2)	-0.365(9)	69,239–241
copper	5421[a]	1357.77	(612.30)	4.29(15)	-18.484(14)	0.030(6)	69,239, 242
iron	5966[a]	1811.15	(673.35)	12.2(2)	-14.14(6)	0.111(6)	69,243, 244
cobalt	5400[a]	1768.15	(476.20)	11(4)	-11(1)	0.32(7)	69,245, 246
aluminum	8550[a]	933.473	(410.66)	2.44(8)	-10.56(15)	0.001(10)	69,243, 247
cadmium	2960[a]	594.219	(170.52)	0.21(5)	-18.632(10)	0.013(4)	69,235, 236,248
thallium	2329[a]	577.15	(60.30)	2(4)	-16(3)	0.10(13)	69,236, 245,249, 250
gallium	7620[a]	302.915	-131.2(8.69)	1.38(9)	-21.2(8)	-0.40(2)	69,235, 236,251, 252
indium	6730[a]	429.749	(53.69)	2.48(2)	-25.2(2)	-0.420(4)	69,236, 245,253
mercury	1764.15[a]	234.321	42.3(176.39)	0.206(11)	-14.94(5)	-0.158(5)	235,236, 252,254–256
water	647	273.15	149.4(178.00)	2.326(11)	-8.86(4)	0.035(7)	135,252, 257–259
2-butanol	536	158.45	(57.51)	9.65(4)	-5.1(2)	3.44(10)	260,261
cyclo-hexanol	645	299.08	128	12(3)	-5(10)	1.0(7)	200,262, 263
ethylene glycol	720	261	115	8.97(3)	-0.03(2)	4.2(6)	198,202, 264

α-propylene glycol	625	214	127	2.5(8)	-24(3)	0.96(4)	202,265, 266
benzene	564	278.65	(94.84)	3.34(9)	-12.1(4)	0.105(4)	252,267–270
toluene	593	177.9	96	2.89(3)	-13.70(13)	0.024(7)	51,267, 271
ethyl-benzene	617	177.8	88	2.31(6)	-16.3(2)	0.207(5)	202,214, 272,273
propyl-benzene	638.4	173	(94.44)	3.50(5)	-13.9(2)	0.024(8)	214,274
butyl-benzene	660.5	185.1	(106.23)	3.42(3)	-14.96(12)	0.025(6)	214,275
isopropyl-benzene	631.1	177.1	110(109.82)	3(3)	-2(5)	1.3(5)	27,137, 276
propylene carbonate	762.7[a]	225	128	5.7(3)	-0.14(15)	2.1(3)	33,51,277, 278
dimethoxy-methane	480.6	168	(154.92)	0.685(12)	-20.09(8)	0.118(2)	202,279
acetic acid	593	289.6	(108.14)	1(2)	-25(7)	0.20(11)	202,280
Octamethyl-cyclotetra-siloxane	585.7	290	52(43.64)	8.2(3)	-12.6(9)	0.05(3)	202,281, 282

a. T_c is from one of the references for the material. The T_c's without this superscript are from the NIST website http://webbook.nist.gov/.
b. When literature values are not available, or when literature reports are the fitted VFT T_0 values, values for T_K or T_c were fitted, and are reported in ().
c. In the columns of ΔH^*, ΔS^* and z parameters for crystallization and viscosity, the values in parentheses are the standard errors.
d. The $v^2\rho$ of *o*-cresol is used since its own $v^2\rho$ is unavailable.
e. $v^2\rho$ is approximated as the bulk modulus and is calculated with Young's modulus (35.7 GPa) and a Poisson's ratio of 0.3.
f. Different fitted T_K's are used for crystallization (128.41K) and viscosity (487.40K), presumed to be a result of the change in structure from rings to chains in the liquid.
g. The averaged lattice constant is the average of the lattice constants of the other two polymorphs, since its own lattice constant is unavailable.
h. The $v^2\rho$ of OTP is used since its own $v^2\rho$ is unavailable.
i. Data and TZT_c fit for crystallization is for isotactic polystyrene, while data and TZT_{rlx} fit for viscosity is for atactic polystyrene.
j. The $v^2\rho$ of *n*-nonadecane since its own $v^2\rho$ is unavailable.

Figure B.1. Experimentally measured viscosity data and fit to TZT_{rlx} Equation (2.11) (solid lines) for materials described in this work. (a) – (b) Viscosity of *n*-alkanes from methane to *n*-eicosane, with the number of carbons marked next to the data of each alkane; (c) Viscosity of *n*-alkylbenzenes, with the name of each alkylbenzene marked next to its data; (d) – (q) Viscosity of materials that also have crystallization data reported in this work; (r) – (ac) Viscosity of metals; (ad) – (am) Viscosity of all other materials described in this work.

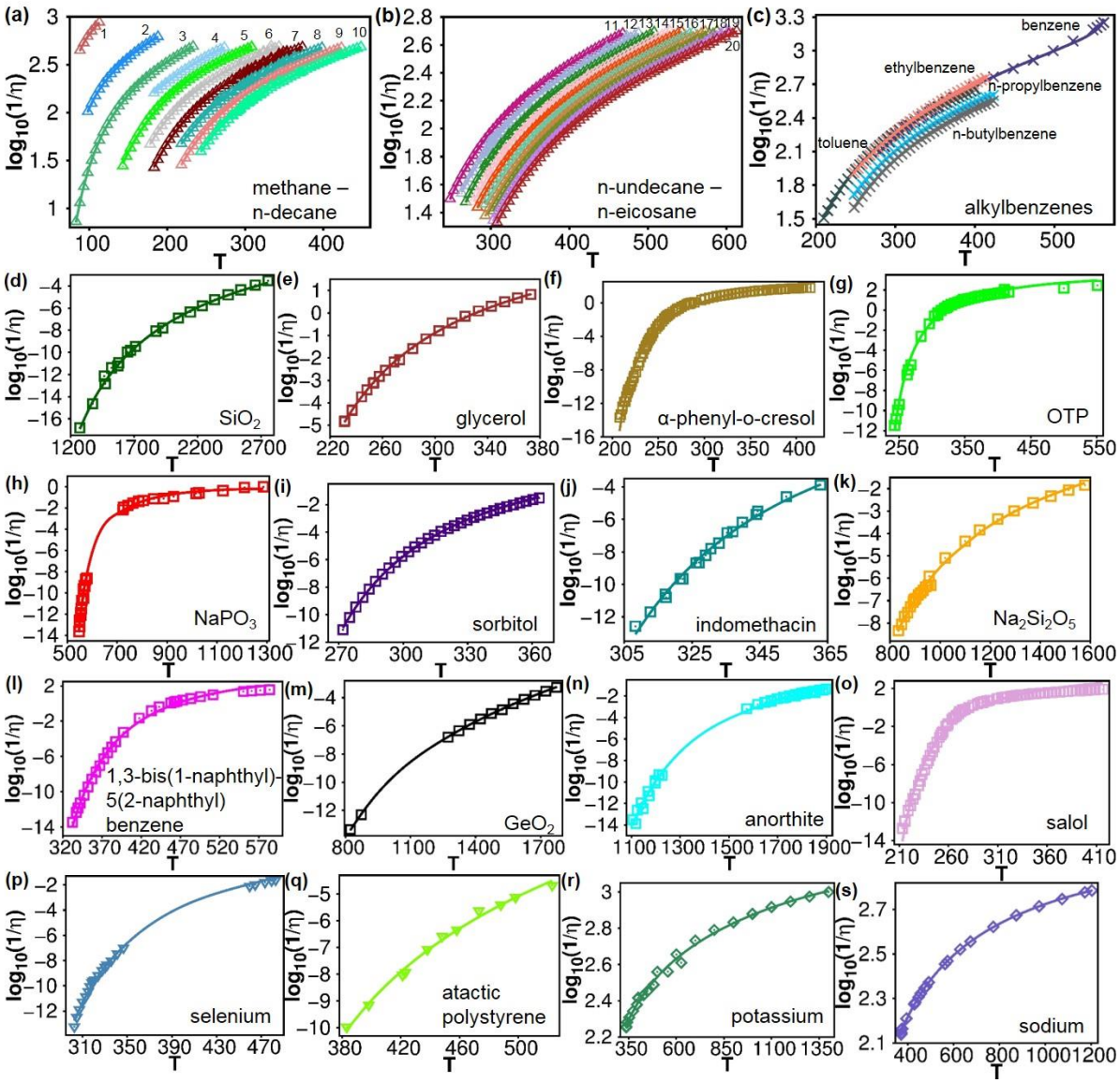
(a)
methane –
n-decane
(b)
n-undecane –
n-eicosane
(c)
benzene
ethylbenzene
n-propylbenzene
n-butylbenzene
toluene
alkylbenzenes
(d)
SiO2
(e)
glycerol
(f)
α-phenyl-o-cresol
(g)
OTP
(h)
NaPO3
(i)
sorbitol
(j)
indomethacin
(k)
Na2Si2O5
(l)
1,3-bis(1-naphthyl)-
5(2-naphthyl)
benzene
(m)
GeO2
(n)
anorthite
(o)
salol
(p)
selenium
(q)
atactic
polystyrene
(r)
potassium
(s)
sodium
log10(1/η)
T

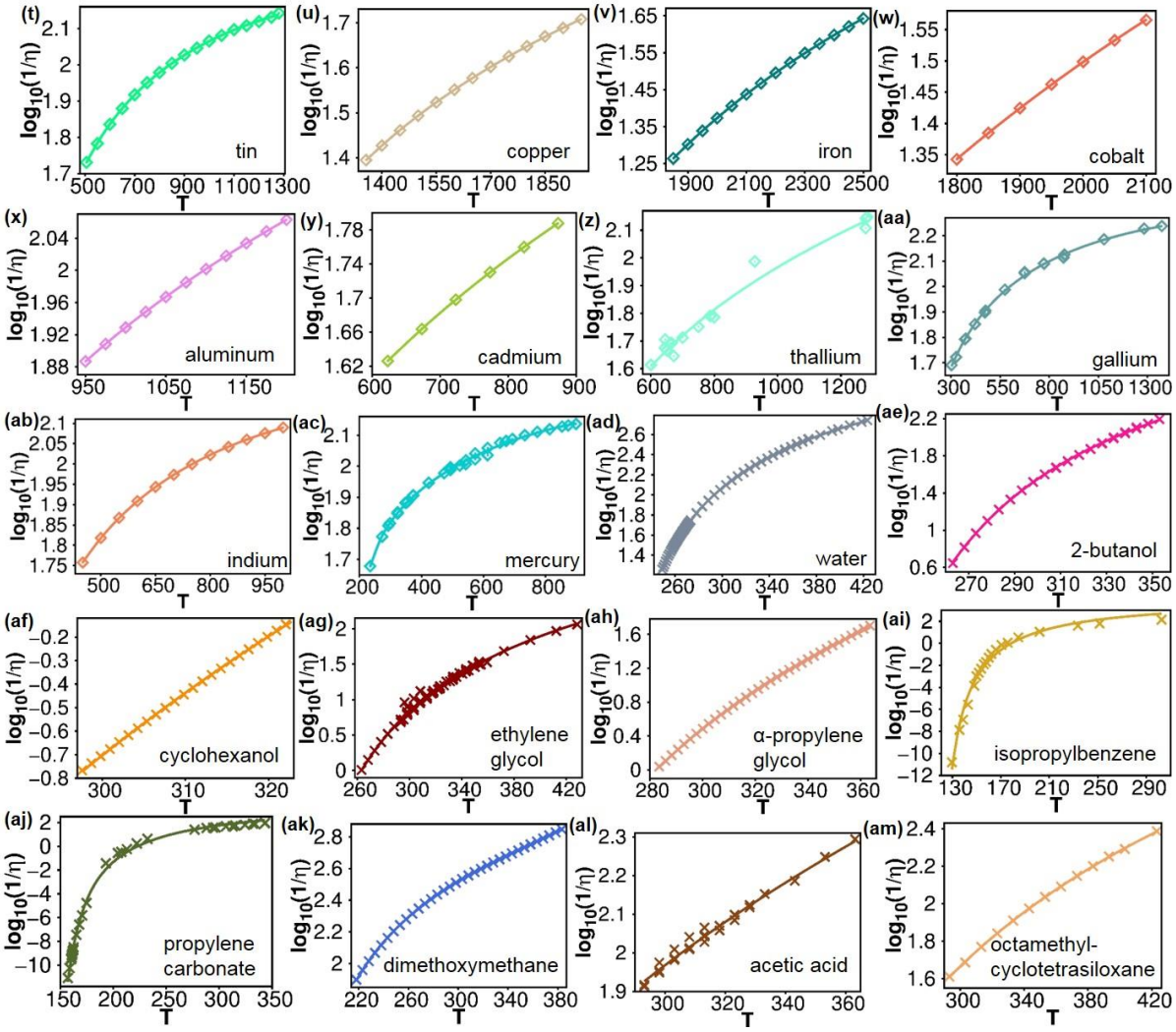
(t)
tin
(u)
copper
(v)
iron
(w)
cobalt
(x)
aluminum
(y)
cadmium
(z)
thallium
(aa)
gallium
(ab)
indium
(ac)
mercury
(ad)
water
(ae)
2-butanol
(af)
cyclohexanol
(ag)
ethylene glycol
(ah)
α-propylene glycol
(ai)
isopropylbenzene
(aj)
propylene carbonate
(ak)
dimethoxymethane
(al)
acetic acid
(am)
octamethyl-cyclotetrasiloxane
log10(1/η)
T

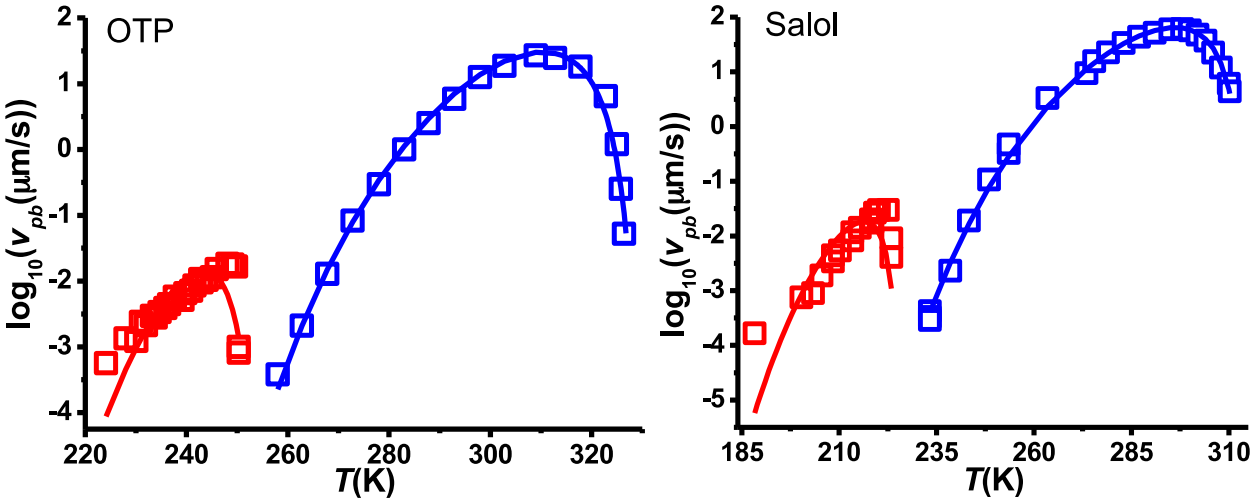

Figure B.2. Rate of crystal growth, and glass to crystal formation for OTP and Salol. Data (symbols) are taken from references 121 and 146, and 122, respectively. Crystallization data are fit using Equation (5.1), and literature reported T_m and T_K data (blue line). APC fits (red line) utilize ΔH_c*, ΔS_c* and z_c parameters from the bulk crystallization, as well as $T_g = T_{m\,APC}$ values as the highest temperature for which the glass to crystal formation is observed, with T_K' as the only additional fitting parameter.